Design and Implementation of A Three-Level Boost converter for Battery Impedance Spectroscopy

Prepared by:

FALOYE OMOLOLA MOSUNMOLA

FLYOMO002

Department of Electrical Engineering

University of Cape Town

Prepared for:

PROFESSOR PAUL BARENDSE

Department of Electrical Engineering

University of Cape Town

Submitted to the Department of Electrical Engineering at the University of Cape Town in partial fulfilment of the academic requirements for a Master of Science degree in **ELECTRICAL ENGINEERING**

Key Words: Three-level Boost converter, Impedance Spectroscopy, galvanostatic mode, Frequency Response Analyser Parameterization

Declaration

1. I know that plagiarism is wrong. Plagiarism is to use another's work and pretend that it is one's own.
2. I have used the IEEE convention for citation and referencing. Each contribution to, and quotation in, this final year project report from the work(s) of other people, has been attributed and has been cited and referenced.
3. This final year project report is my own work.
4. I have not allowed, and will not allow, anyone to copy my work with the intention of passing it off as their own work or part thereof

Name: **FALOYE OMOLOLA MOSUNMOLA**

Signature: Signed by candidate

Date: 14 September 2020

Acknowledgements

My gratitude goes to Almighty God for his grace he has bestowed upon me to complete this study. I thank the management of University of Cape Town for creating a safe and conductive learning environment.

To my wonderful Supervisor Professor Paul Barendse, am so honoured to work with you, your guidance, meticulous reviews and your endless encouragement is not taken for granted at all.

I am thankful to the Advanced Machines and Energy Systems (AMES) group and the University of Cape Town Postgraduate Office for the financial assistance rendered during the cause of my study.

I am grateful to my parent Nelson Faloye and Oluwabunmi Olaleye for the love and moral support given to me, even though I lost Nelson in cold blood during my study. To my younger brother Olawale Faloye you have made this a dream come true. To my uncles (Tunde and kayode Olaleye) I appreciate your care and support. To my sisters Ifedayo and Iyabode Akinsolu I appreciate your constant love and support.

I am indebted to my adopted parent Dr and Mrs Mathew Shobiye for his financial support, his guidance and his encouragement, God bless you mightily.

To my wonderful family here in Cape Town Mr and Mrs Lateef Adesola Akinyemi, I appreciate everything you have done during my stay in Cape Town God will always enrich your pocket. Mr Dayo Oladejo knowing you is a blessing, I appreciate your advice and support during the research. To my colleague turned uncle Mr and Mrs Oluwafemi Olayiwola, God bless you for not giving up on me during my study and thanks for your advice and support.

To my special friend Arc. Mandandola Ibukunoluwa Micheal, thanks for your understanding, support care and word of advice, God bless and increase you in all your endeavours.

My appreciation goes to the AMES technicians Masan, Phillip Titus and other AMES technicians for their technical assistance and for providing electrical electronic component for my experimental set-up.

Finally, I would like to express my gratitude for the support and friendship with a special thanks to Linda Shelembe for the countless hours you put in assisting me in this research.
Also, my appreciation goes to Akinola Ajayi-Obe, John Mushenya, Kunle Alao, Sunday Oladejo and Shireen Sabodien for their contribution to this project.

Abstract

Lithium-ion batteries are the most are widely used as electrical storage device in various applications such as portable electronics, electric vehicles, Photovoltaic application, telecommunication etc due to the characteristics of the batterie such as high-power density, long cycling and high-power efficiency. Extensive condition monitoring of the battery should be implemented due to the usage of the battery so that there will be an increase in all the overall performance and expectancy. This research is focused on implementing an online condition monitoring on the Li-ion battery using a signal injection through a power converter.

The implemented technique in this research is known as the Electrochemical Impedance Spectroscopy (EIS). The EIS is a widely known technique used in determining the internal impedance of a battery cell. The estimated impedance can be used to determine the state of charge (Soc) and State of health (SoH) of a battery. The EIS is used to characterize the electrochemical behaviour thereby monitoring the change in the impedance of the cell of the battery. The EIS technique is accomplished by sinusoidally injecting current at different frequencies and measuring the voltage response. A standard Frequency Response Analyser (FRA) is used as an offline test while the battery is disconnected from the Load. The limitation of this standard FRA analyser is that it is bulky and Expensive.

Attempts have been made to migrate the techniques to online operations, each having their own challenges. For an online Implementation, the interfacing power converter is used for Signal injection to measure the impedance of the battery. This work explores the low current ripple advantage of a three-level boost converter to implement EIS on lithium ion battery.

Table of Contents

List of Figures

List of Tables

1. Introduction

1.1 BACKGROUND TO THE STUDY

Batteries are considered as one of the most important devices for storing energy because of the increase and demand of electric energy in modern society. Batteries are often used for energy storage and backup power supply in hospitals, portable electronics applications, telecommunication, photovoltaic (PV) applications, hybrid electric vehicle (HEV) [1] [2]. For these applications, low cost and safe protecting system are required to ensure reliable operation.

At present, lithium ion (Li-ion) batteries are taking the lead in today's market because of the high efficiency, long cycle and high-power density. Usually the battery lifetime depends on these five factors: proper storage, internal temperature rise, battery chemistry, cycling and maintenance. Because of the enormous demand of energy from batteries, aging of the batteries, possible battery fires, and other undesirable situations that may occur, there is a need for continuous state of charge (SOC) and state of health (SOH) estimation. The estimation can be carried out using Electrochemical Impedance Spectroscopy EIS. EIS quantifies the internal state/condition of the battery [3] [4]. The impedance of the battery has been observed to be an adequate measure of monitoring the state of the health and state of charge of the battery [5] [6].

There has been continuous effort in improving the electrochemistry of the cells to achieve greater and overall performance. There is also the opportunity to improve the power electronics and control systems to ensure accurate monitoring of the battery state as implemented in a battery management system (BMS). The BMS is designed to continuously monitor the battery system. Traditionally, the BMS determines the state of charge and the state of health of the battery by the continuous monitoring of the current, temperature, and terminal voltage of the battery. This provides the information required for the monitoring. However, more information regarding the internal state of the battery can be derived using EIS. The EIS techniques is a well-known scheme that injects small signal perturbations for determining the battery impedance. An EIS is an AC injection technique used in computing the battery internal impedance. Conventionally, an expensive and bulky Frequency Response Analyser (FRA) is used to perform EIS by measuring the AC response of the battery. The use of expensive FRA can be avoided using the power converter associated with the battery system for implementing EIS in BMS.

Recently, several power converters have been used to estimate the state of charge and state of health of the battery in literature using EIS [4] [7]. The approach mostly adopted in literature is that of single-sinusoidal EIS approach, which injects and measures each perturbation sinusoid separately. There has

been research aimed at implementing online EIS on the battery using the control systems that are already connected to the battery to reduce downtime, cost of the equipment and human intervention.

In this research, the focus is on a three-level boost power converter which is used to investigate the high-resolution capabilities in implementing impedance spectroscopy on the Lithium-ion batteries. The non-isolated three-level DC-DC converter topology was chosen based on its reduction in cost as compared to the interleaved boost converter while minimizing ripple current and increasing voltage resolution as compared to the conventional boost converter. The three-level boost converter can also be used for a high voltage applications since the voltage is shared across the switches. In this research the small signal analysis, simulation and experimental results are presented.

1.2 OBJECTIVES OF THIS STUDY

- Conduct a literature review on the electrochemical cell or batteries to determine the cells or batteries that are currently being used for high power and high energy applications.
- Conduct a literature review on current condition monitoring techniques for batteries with an emphasis on EIS techniques.
- Investigation of different battery modelling techniques that can be used with EIS techniques.
- Investigation of different power converter topologies that can be used for implementing online EIS techniques.
- Perform EIS with a Frequency Response Analyser (FRA) (NOVA AUTOLAB PGSTAT302N) to serve as the benchmark when evaluating the proposed scheme.
- Design and simulation of the power converter used for impedance spectroscopy.
- Design of the voltage and current control system for implementing the EIS using the converter and to evaluate its performance.
- Design a low pass filter to filter out the high frequency for EIS implementation with the converter.

1.3 RESEARCH METHODOLOGY

In this study, the research methodology that would be adopted is simply the use of analysis and simulation and experimental verification. This is divided into four core sections namely design, analysis, simulation and experimental verification. The analytical section of this research analyses the theory and modelling of the electrochemistry of the Lithium-ion battery which is then modelled with the three-Level Boost converter. A simulation of the EIS implementation with the converter was implemented in the MATLAB Simulink environment, before the experimental verification. The closed loop of the system was also designed in MATLAB Simulink. An FRA (NOVA AUTOLAB PGSTAT302N) device was used to

verify the battery electrochemical characteristics to validate the simulated and the experimental results of the implantation of the EIS with converter.

1.4 SCOPE AND LIMITATIONS OF THE RESEARCH

This research is based on achieving a high resolution of the system when performing Electrochemical Impedance Spectroscopy on the Lithium-ion battery. The advantage of attaining low-inductor current ripple when using a three-level boost converter was the key focus of the project. This is critical when injecting small signals to measure the impedance of the Lithium-ion battery in determining the SoC and SoH of the battery. This research also demonstrates the closed loop of the three-level boost converter. For other Lithium-ion batteries with different battery chemistries, the battery non-linear impedance model was outside the scope of this study. This study does not cover to other areas such as BIS

1.5 PLAN OF DEVELOPMENT

Chapter 2 present the literature review of existing battery technologies with emphasis on Li-Ion batteries. This is followed by a review of the modelling of the Li-ion battery. Finally, the battery model was discussed.

Chapter 3 investigates the various testing techniques, whereby Electrochemical Impedance Spectroscopy (EIS) is introduced. It then investigates the appropriate DC operating point to perform EIS as well as the optimal perturbation amplitude to be used in the experiments. Converter EIS implementation was also discussed.

Chapter 4 presents an overview of a three-level Boost converter. It then describe the operation of the converter, the current ripple and the active stress on the switches. Efficiency of the converter was also analytically described. State space averaging techniques are performed to attain a transfer function of the converter. This transfer function is used to determine the closed loop control for the power converter.

Chapter 5 explains the implementation of the Three-level Boost Converter for EIS. The converter and EIS specification were analysed. The passive components were designed, and the controller was designed based on transfer function from the previous chapter. Finally, the design of the voltage balancing control for the capacitor is presented.

Chapter 6 presents the simulation and the experimental results of the three-Level Boost Converter and the results are discussed afterwards.

Chapter 7 presents and discusses the results obtained from the FRA experiment. Also, the EIS results for the simulation and experimentation are presented and compared. Parameters for the equivalent circuit model of the battery is then extracted from the experimental results, to demonstrate its ability to monitor SoC. The online experimental results for the implementation of the three-level boost converter for EIS were also presented and discussed.

Chapter 8 contains the conclusions of this dissertation and gives recommendations in the form of future work or studies in this area of research.

2. Battery literature review

In this chapter, literature review regarding the battery and cells will be comprehensively reviewed and discussed extensively.

2.1 Batteries and Cells

The word batteries and cells are mostly mistakenly referred to each other. A battery is an energy device which uses an electrochemical oxidation-reduction (redox) reaction to convert the stored chemical energy into electrical energy in its active membrane while the cell is mainly the electrochemical storage. The desired output voltage and capacity of a battery are dependent on the arrangement of cells which can either be arranged in series or in parallel [8].

A cell comprises of three important components. Firstly, the anode (negative electrode) is a reducing electrode which gives up electrons to the external circuit and is oxidized during the electrochemical reaction. The Cathode (positive electrode) is an oxidizing electrode which accepts electrons from the external circuit and is reduced during the electrochemical reaction. The electrolyte is the transportation mechanism. It is the passage which provides the transportation of ions between the cathode and anode of a cell. Electrolytes which are often (liquids such as acids, water, alkalis and solvent with dissolved salt) are required for ionic conduction. The suspension of the electrode in the electrolyte is where the chemical reaction takes place by converting the electrical energy to chemical energy vice-versa [9]. Figure 2.1 shows the schematic diagram of the anode and cathode of a cell.

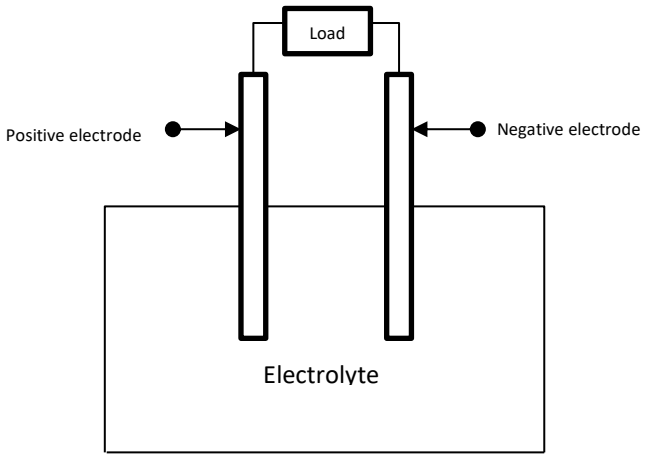

Figure 2.1: The anode and cathode of a cell.

The roles of the two-metal electrodes (anode and cathode) is dependent of the charging or discharging of the cell.

During the charging of the cell, the two electrodes are designed as positive electrode(anode) and negative electrode(cathode), respectively. The chemical reaction at the anode is called oxidation. There is a release of electrons that flow freely to the cathode. At the cathode, the reduction process occurs. There is a free movement of electrons in the anode, the cathode accepts the flow of electrons from the anode through the chemical reaction which occurs at the electrolyte and the electrode interface. The discharging process is the reverse of the charged process. The positive electrode(anode) and the negative electrode (cathode) interchange roles. The electrons extracted from the oxidation at the cathode flow to the anode where reduction happens. Figure 2.2 shows the charging and discharging electrochemical cell.

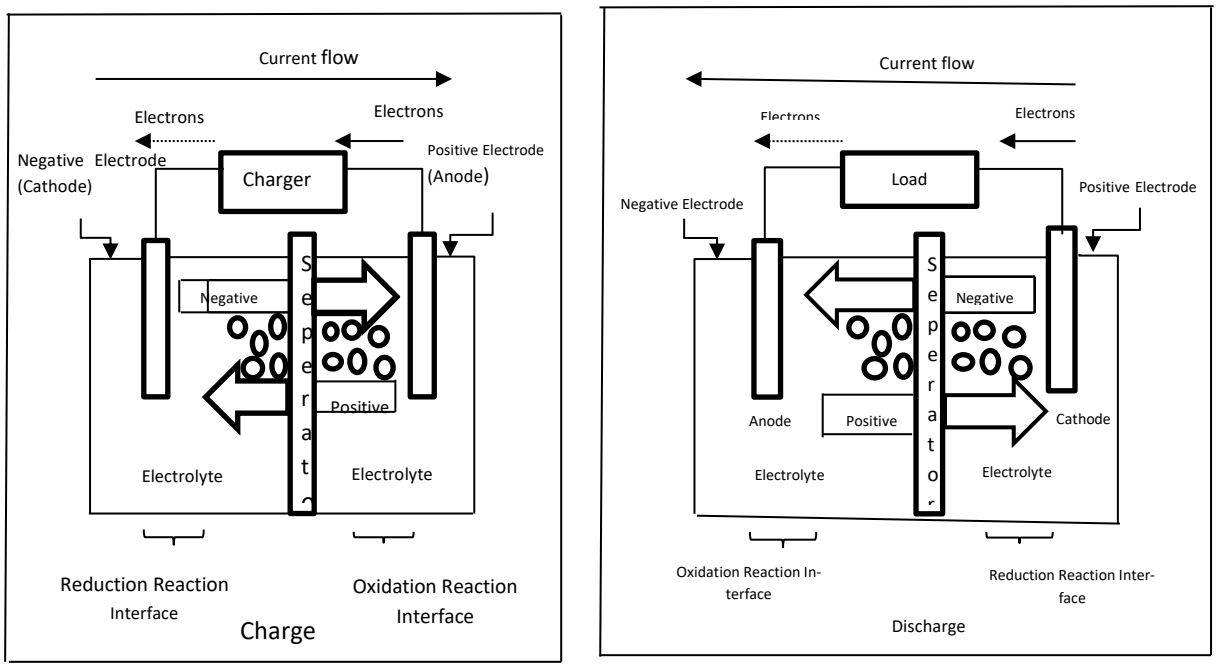

Figure 2.2: The Electrochemical Operation of the Cell

2.1.1 Types of Batteries or Cells

i. Non-Rechargeable (Primary) Cells or Batteries

The primary batteries or cells are not easily or effectively recharged electrically and, hence, are discharged once and discarded. Many primary cells in which the electrolyte is contained by an absorbent or separator material (there is no free or liquid electrolyte) are termed ‘‘dry cells.’’

The primary battery is convenient and inexpensive, lightweight source of packaged power for portable electronic and electric devices, lighting, photographic equipment, toys, memory backup, and a host of other applications, giving freedom from utility power. The general advantages of primary batteries are good shelf life, high energy density at low to moderate discharge rates, little of any maintenance, and ease of use. Although large high capacity primary batteries are used in military applications, signalling,

standby power, and so on. Most primary batteries are the familiar single cell cylindrical and flat button batteries or multicell batteries using these component cells [9].

ii Rechargeable (Secondary) Cells or Batteries

These batteries can be recharged electrically, after discharging, to their original condition by passing current through them in the opposite direction to that of the discharged current. They are storage devices for electric energy and are known also as ‘‘storage batteries’’ or ‘‘accumulators.’’ The applications of secondary cells or batteries can be categorised in two main sectors:

- The secondary batteries or cells which are used as an energy-storage device, generally being electrically connected to and charged by a prime energy source and delivering its energy to the load on demand. Examples of such batteries and cells are automotive and aircraft systems, emergency no-fail and standby (UPS) power sources, hybrid electric vehicles and stationary energy storage (SES) systems for electric utility load levelling [9].
- The secondary batteries or cells which are used or discharged essentially as a primary battery but recharged after use rather than being discarded. Secondary batteries are used in this manner as, for example, in portable consumer electronics, power tools, electric vehicles, etc., for cost savings (as they can be recharged rather than replaced), and in applications requiring power drains beyond the capability of primary batteries. Secondary batteries are characterized (in addition to their ability to be recharged) by high power density, high discharge rate, flat discharge curves, and good low-temperature performance.

Their energy densities are generally lower than those of primary batteries. Their charge retention also is poorer than that of most primary batteries. Although the capacity of the secondary battery that is lost on standing can be restored by recharging. Some batteries known as ‘‘mechanically rechargeable types,’’ are ‘‘recharged’’ by replacement of the discharged or depleted electrode, usually the metal anode, with a fresh one [9].

iii. Reserve Cells or Batteries

The reserve cells or batteries are different from the primary or secondary cells or batteries. In these types of batteries, a key component is separated from the rest of the battery prior to activation. In this condition, chemical deterioration or self-discharge is essentially eliminated, and the battery is capable of long-term storage. Usually the electrolyte is the component that is isolated. In other systems, such as the thermal battery, the battery is inactive until it is heated, melting a solid electrolyte, which then becomes conductive. The reserve battery design is used to meet extremely long or environmentally severe storage requirements that cannot be met with an ‘‘active’’ battery designed for the same performance

characteristics. These batteries are used, for example, to deliver high power for relatively short periods of time, in missiles, torpedoes, and other weapon Systems [9].

iv Fuel Cells or batteries

The fuel cell represents the fourth category of batteries. Fuel cells are like batteries except for the fact that all active materials are not an integral part of the device (as in a battery). In fuel cells, active materials are fed into batteries from an outside source. The fuel cell differs from a battery in that it possesses the capability to produce electrical energy if active materials are fed to the electrodes but stop operating in the absence of such materials. A well-known application of fuel cells has been in cryogenic fuels used in space vehicles. Use of fuel cell technology for terrestrial applications has been slow to develop. Although recent advances have generated a revitalized interest in a variety of systems with applications such as utility power, load-levelling, on-site generators and electric vehicles [9]. In this research, a secondary type of cells or battery is being used. The next section explains different battery chemistries.

2.2 Batteries or Cell Chemistries

There are several battery chemistry cells available, although, the focus of this research is Lithium ion battery cell. But a summary discussion on various other battery chemistries with their advantages and disadvantages are discussed in the next sections.

2.2.1 Lead Acid Chemistries:

This is the oldest form of a rechargeable batteries. These are mostly used for starter motors in combustion vehicles. The lead-acid was developed into two main designations. The first being the sealed lead-acid (SLA) and the second is the large valve regulated lead -acid (VRLA). Both battery types should not be operated at high depths of discharge to preserve cycle life. Lead acid batteries have three elements which are Lead acid, Lead oxide and dilute sulphur. Some of the advantages of the Lead acid are low cost and mature technology. While self-discharge, heaviness in weight, low specific power and energy are the main disadvantages of this chemistry [10].

2.2.2 Nickel Based Chemistries:

The Nickel based battery has two main popular types of battery namely Nickel metal hydride (NiMH) and Nickel cadmium (Nicad) which are the based battery technologies. The Nickel metal hydride (NiMH) are commonly used in electric vehicles and it has an advantage of an advanced performance in safety and power density. It offers 30-40 percent higher density compared to Nicad. The flaunting price of the Nickel and its low power is the main disadvantage of this battery technology [11]. Nickel cadmium has the most suitable stable performance because its performance is not affected by over charged or over

discharge [12]. The disadvantage of the battery chemistry is that cadmium is poisonous, so it is being banned for industrial application [10].

2.2.3 2.2.3 Lithium-ion Based Chemistries:

Lithium-based batteries offer higher specific power and good energy density than Lead-Acid and Nickel based batteries [11]. The Lithium-based batteries are categorized into two main categories the Lithium polymer (Li-poly) and the Lithium -ion (Li-ion). The Lithium-Ion (Li-Ion) battery is probably the most well-known in the market today. Lithium is the lightest of all metals, has the greatest electrochemical potential and provides the largest energy content of the metals. The common materials used for the positive electrode (anode) of the Lithium-Ion (Li-Ion) batteries are Cobalt Oxide, Manganese Oxide, Iron Phosphate, Nickel Manganese Cobalt Oxide and Nickel Cobalt Aluminium Oxide, while Lithium salt in organic solvent and carbon are used for the negative electrode (cathode)and electrolyte, respectively. Because of the high specific energy (over 100 Wh/kg), recyclability and long cycle life (several thousand cycles). Li-ion is widely used [13]. Li-Ion batteries units are produced in billions every year in the market of popular devices such as laptops, cell phones and cameras. Below is the battery Comparison chart illustrating the volumetric and specific energy densities showing smaller sizes and weight.

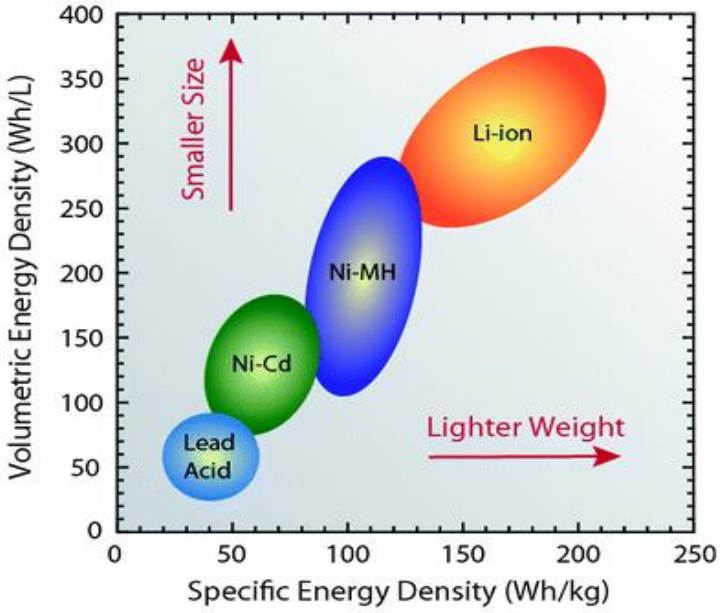

Figure 2.3: Specific Power Versus Specific energy density for different battery [14]

From Figure 2.3 the battery comparison chart shows the advantage of the Lithium Ion over the other battery. Therefore, in this research, Lithium-ion is used and it is discussed in detail in the next section.

2.3 History of Lithium-ion Cell

Lithium is the lightest of all metals, and it has the greatest potential and provides the largest energy content in all metals. The Li-ion tapping actual began in the year 1912 by G.N. Lewis who was the Dean of chemistry at the University of California Berkley [15]. In the early year of 1970's, M. S. Whittingham

at Exxon proposed the first Lithium-ion non- rechargeable (primary)batteries and were made commercially available [9].

In the year 1980's, attempts to develop lithium-ion rechargeable batteries were made, and it was found that a high voltage and excellent capacity can be achieved by using a rechargeable (Secondary) batteries which use Lithium metal anode. The characteristics of the Lithium metal anode lead to a high energy density but could not be sustained because of the violent chemical reactions that occur during the rise in temperature change of the battery. Therefore, research was made using a Lithium-ion battery which is a non-metallic battery, which was comparatively safer than Lithium metal [16].

The significant advancement in the lithium batteries development was made in 1986, by discovery of intercalation materials where the Lithium was used as an insertion material for rechargeable batteries. Intercalation is a process where metal ions are reversibly removed or inserted into a host without a significant structural change to the host. The electrochemical properties of lithium intercalation in graphite were shown in Figure 2.4.

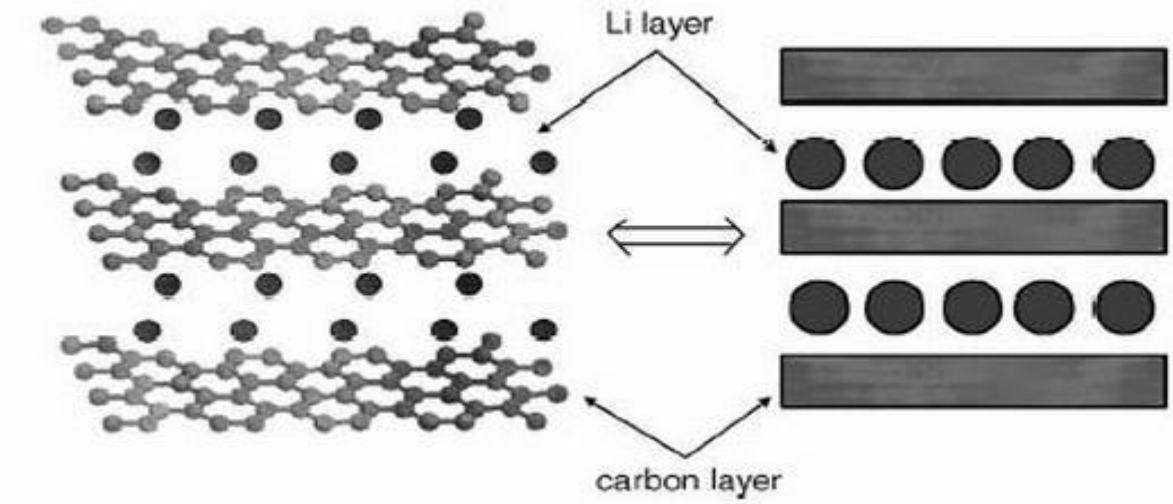

Figure 2.4: Structure of the graphite intercalated with Lithium [16] .

A few years later, Dr J. Goodenough proposed that the material under the family of $LixMO_2$ (where M= Co, Mn or Ni) as a cathode material [17], and research was being done to find a replacement for Li metal anodes. Eventually, based on research by John Goodenough's team the first commercial lithium was released by Sony in 1991 [18] [19].

2.3.1 Working Principle of Li-ion Battery

A Li-ion battery is usually referred to a secondary battery in which energy is stored chemically through the Red-ox process which employs lithium intercalation between the positive(cathode) and the negative cathode(anode) electrodes. During the charging and discharging of the battery the lithium -ions move between the cathode and the anode because of this they are also referred as "Rocking-chair" batteries. Basically, there are four primary components of a lithium-ion battery: the anode, cathode, separator and

electrolyte for which a variety of materials may be used. The cathode acts as a positive electrode which accepts the electrons while acting as reducing agent and the anode acts as a negative electrode which donates the electrons and oxidizes during the discharge cycles. The electrodes do not touch each other but are electrically connected by the electrolyte while the separator prevents the mixing between them but allows ions to flow. Figure 2.5 illustrate the charging and discharging principle Li-Ion of battery.

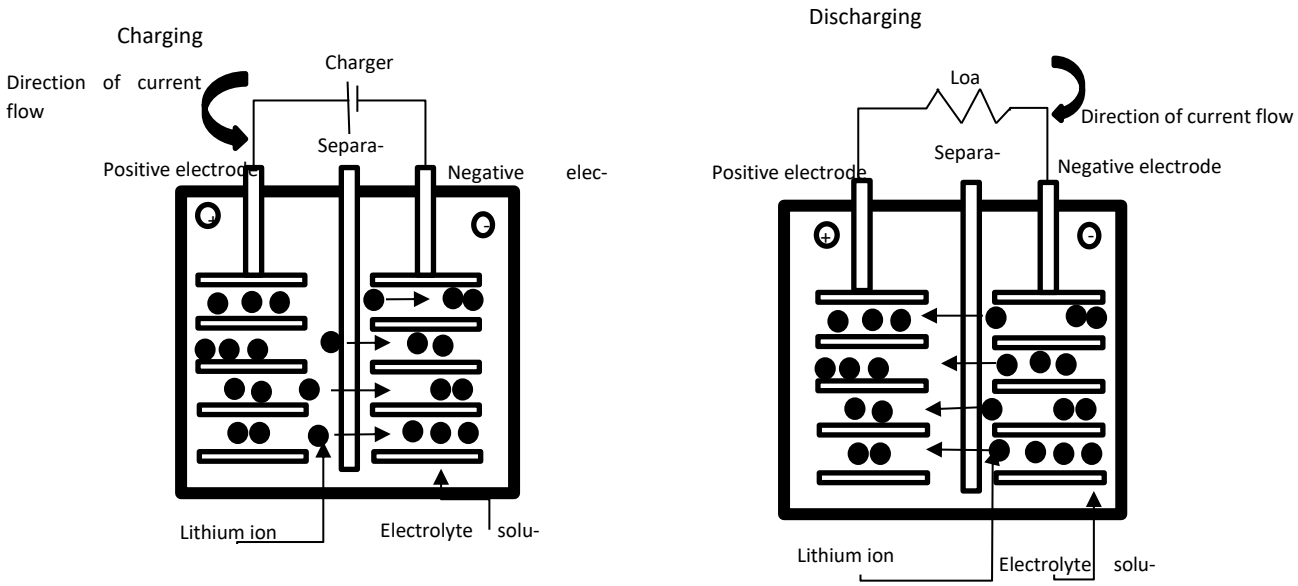

Figure 2.5: Diagram of Charging and Discharging of Li-ion cell.

2.3.2 Charging and Discharging of a Li-ion Battery

There are many methods of charging a battery such as float charging, trickle- charging, pulse charging, constant current charging and constant voltage charging. Since the focus of this research is on lithium-ion batteries, constant current and constant voltage charging will be considered since they are the preferred methods for charging a Lithium based cell. [20]

A Lithium-ion battery is a fixed voltage source that is current limited. The battery is charged at a constant current (CC) until the battery voltage reaches a threshold, which is the set-point voltage.
During the Constant Current phase, when the set-point voltage has been reached the current will begin to decrease to maintain the set-point voltage on the battery. This is known as the constant voltage (CV) phase of charging. Most major Li-ion cell manufacturers recommend 4.2V as the ideal set point voltage. The constant-voltage cut-off time is typically given by the manufacturer with a desired degree of accuracy to ensure the specified cell cycle-life and capacity can be met. It is important to note that this value is specified for the voltage available at the cell's terminals when the current is actively charged or discharged from the cell [20]. Figure 2.6 Shows the constant current and constant voltage of a lithium-ion battery.

During the discharging stage of lithium-ion battery, the energy is depleted, the cell voltage drops rapidly. The nominal discharge voltage for Li-ion cell is typically 2.5V.

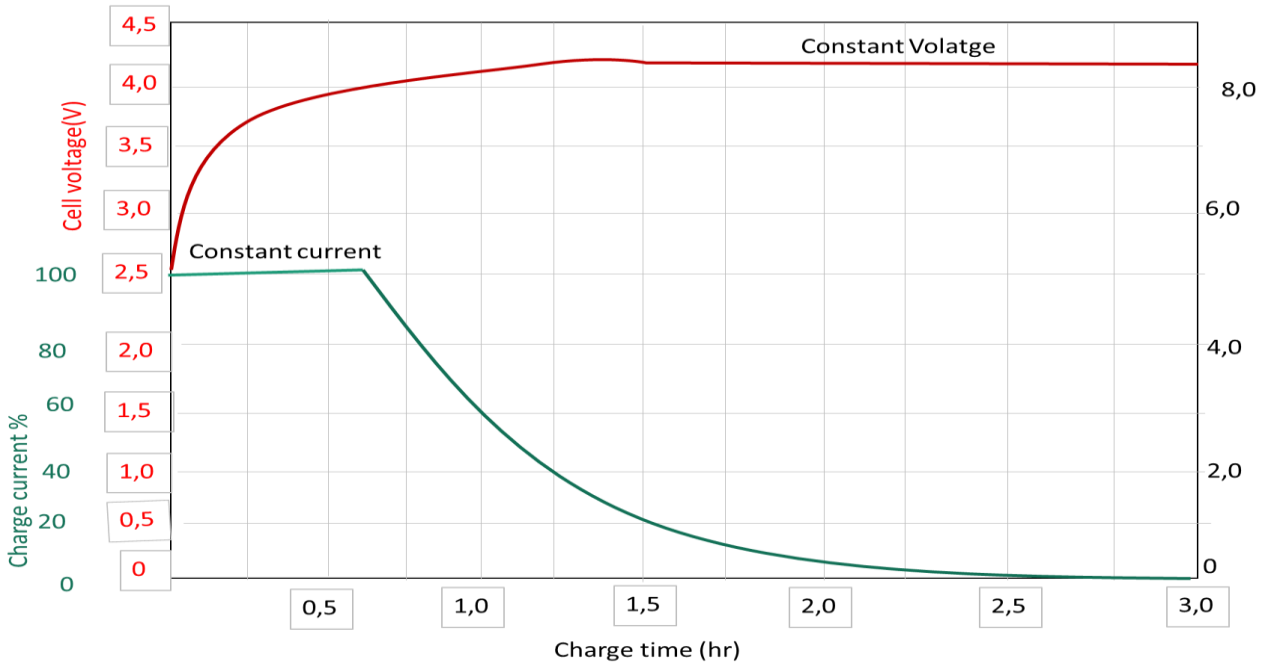

Figure 2.6: Constant Current/Constant Voltage charging method for Li-ion cell

2.3.3 TYPES OF LITHIUM ION BATTERY

There are different types of lithium-ion batteries, the most commonly used are discussed below:

i. Lithium Cobalt oxide

Lithium Cobalt Oxide (Li-Co Oxide) batteries provide advanced electrical performance and more specifically, very high specific energy. However, they suffer from poor thermal stability. This chemistry is used in small portable electronics such as cameras, cell phones, tablets, and some laptops. This chemistry is not suitable for industrial applications and electric vehicles due to its high usage of cobalt and is relatively expensive [21]. The positive electrode is derived from cobalt oxide and the negative electrode is graphite carbon. Typical charge and discharge current maximums are relatively low. Anything higher causes overall cell life to decrease. Hence, the cells' ability to store energy per unit of weight, of this chemistry is high, the specific power is low. The specific power is a measure of how much instantaneous power the cell can provide in a short period of time [10].

ii. Lithium Manganese oxide

The chemistry of Lithium Manganese Oxide (Li-Mn Oxide) was first introduced in 1996 and had a positive electrode made of lithium manganese oxide. Because of the architecture, a three-dimensional spinel structure, ions can flow more freely, decreasing internal resistance. This allows for high currents which

make this chemistry suitable for applications such as power tools, medical equipment, and electric vehicles [11] as compared to lithium cobalt, lithium manganese offers higher safety factors and lower cost. However, it has a low cell durability roughly one-third the size of lithium cobalt's storage capacity.

iii. ***Lithium Iron Phosphate***

In 1996, researchers at the University of Texas implemented phosphate as a positive electrode for a lithium-based cell. This material which can be designed with Nano-scale phosphate which offers low resistance, high current rating, and long cycle life. Along with the benefits and a relatively higher abuse tolerance, this technology finds applications also in power tools, electric vehicles, and back-up power applications. In comparison to the $LiMnO_2$ chemistry, due to $LiFePO_4$'s lower $3.2V - 3.3V$ nominal voltage, it has a slightly lower specific energy. Lithium Ferro Phosphate (Li-Fe Phosphate) provides a good balance in safety, life cycle and cost. However, its energy density is lower than other lithium chemistries [21].

iv. ***Lithium Nickel Manganese Cobalt Oxide***

This chemistry has been around since the 1980s. In this cell chemistry Lithium titanite, as opposed to carbon, is used for the negative electrode. This also forms a spinel structure as with the $LiMnO_2$ cell chemistry, enabling lower internal resistance. This allows this chemistry to safely charge and discharge quickly at high currents and has low temperature discharge characteristics (down to -30°C). Since a single cell provides 2.4V nominally, its specific energy is relatively low [10]. Lithium Nickel Manganese Cobalt Oxide (Li-Ni-Mn-Co Oxide) was developed as an alternative to Li-Co Oxide to balance the cost and performance of the battery. Li Ni-Mn-Co Oxide battery is a suitable choice for electric vehicle, as it offers an excellent trade-off between safety, capacity and performance.

v. ***Lithium Nickel Cobalt Aluminium Oxide***

The Lithium Nickel Cobalt Aluminium Oxide cells have a reasonable long span and power density and there are majorly used for electric vehicles. The Lithium Nickel cobalt aluminium oxide has similar advantages to that of Nickel Manganese Cobalt. The major drawback of this type of cell is that it is costlier and less safety when compared to the Nickel manganese cobalt [22].

vi. ***Lithium Titanite***

The Lithium Titanite is a chemistry which opposes the carbon. They have the Lithium Titanite cathode and a graphite anode. The Lithium Titanite chemistry had been in existence since 1980s and this cell has a low nominal voltage of about $2.4V$ and has a very low specific energy. The Lithium Titanite chemistry can be charged very fast and offer a high discharge rate. The Lithium Titanite is safer than the NMC chemistry type which makes the Lithium Titanite costly [20]. Table 2-1 Shows the characteristics of various Li-Ion chemistry cell.

Table 2-1: Li-Ion Battery Characteristics [20].

Cathode	Anode	Energy Density	Power Density	Cycle Life	Safety	Cost
Lithium cobalt oxide	Graphite	High	Fair	Fair	Fair	High
Nickel cobalt aluminum oxide	Graphite	High	High	Fair	Fair	High
Lithium iron phosphate	Graphite	Low	High	High	Very Good	Fair
Lithium manganese oxide	Graphite	High	High	Fair	Very Good	Fair
Lithium manganese oxide spinel	Graphite	High	High	Fair	Good	Low
Lithium manganese oxide spinel polymer	Graphite	High	High	Fair	Good	Low
Manganese nickel cobalt oxide	Graphite	High	Fair	Low	Fair	High
Lithium manganese oxide spinel	Lithium titanate oxide	Low	Low	High	Good	High
Lithium nickel oxide	Graphite	High	Fair	Fair	Fair	Fair
Lithium manganese nickel oxide spinel	Graphite	High	High	Fair	Fair	Low
Lithium manganese nickel oxide spinel	Lithium titanate oxide	Fair	High	High	Good	Low

2.3.3 Lithium-ion Configuration

There are four different configurations of lithium ion that can be found in the market as of this day namely the cylinder, thin and flat polymer, coin and prismatic battery. Each depends on the application that it is used for. Prismatic configuration is commonly used for low power applications such as laptop, mobile phones etc. The coin configurations are batteries used in wristwatches, hearing aids and medical devices. The thin-flat batteries are commonly used in the automobile and military applications [20].

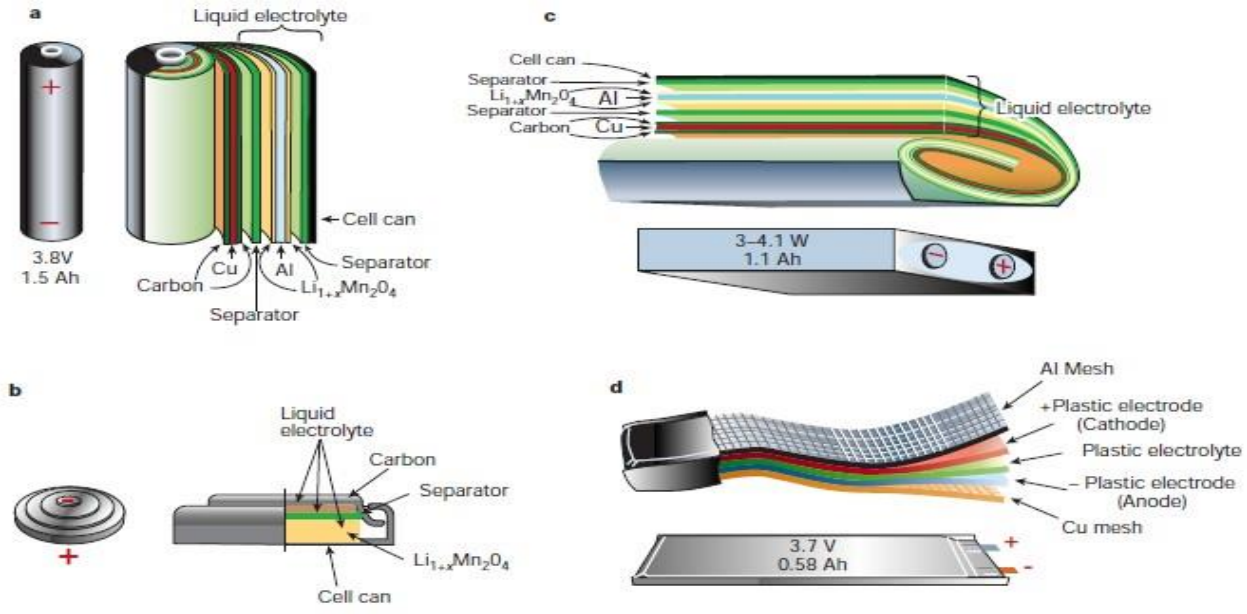

Figure 2.7: Battery Configuration, A. Cylinder, B. coin, C. Prismatic and D. Thin and Flat Polymer

2.4 Degradation of Battery Performance

The degradation of the observed performance characteristics over a cell's lifetime is a significant challenge for the battery system designer. The charging and discharging cycle of the battery over a period leads it to various forms of degradations which is influenced by various operating conditions such as temperature, number of cycles and load applied etc. A primary concern about the battery is the reduction in cell capacity, an increase in impedance which is difficult when incorporating an online estimation on the battery. The difficulty in isolating the causes and form of degradation are usually complex and interrelated processes such as the chemical and the structural change in the electrode, electrolyte compositions, the formation of passive layers, the coverage of previous active reaction surface, loss of cyclable lithium and many more [23].

The degradation of Lithium -ion cell can be caused by many mechanisms. Certain factors are known to be internal mechanism which contributes to the capacity fade, by increasing the mechanical stress effects which can lead to the volume changes of the battery. The electrodes are one out of the major mechanisms which degrade the Lithium -ion battery [24]. The negative electrode of the Lithium -ion battery is generally made of graphite (or carbon), silicon or Titanate. The main aging effect that occurs on the graphite electrode is the development of the solid electrolyte interphase layer [25]. As the layer develops over time, there is a loss of Lithium -ions that can migrate across as well as a decomposition of electrolyte. This layer consists of Lithium oxide and Lithium carbonate. The more the cell is used the larger the interface grows, and it can create a barrier that can completely obstruct interaction with the graphite. The cathode also develops a layer that behaves similarly to the solid electrolyte interphase layer, known as electrolyte oxidation. This is mainly caused by high charging voltages. These layers result in a higher resistance experienced by the cell [26]. Figure 2.8 shows the interphase layer of the Electrolyte oxidation of the Li-Ion.

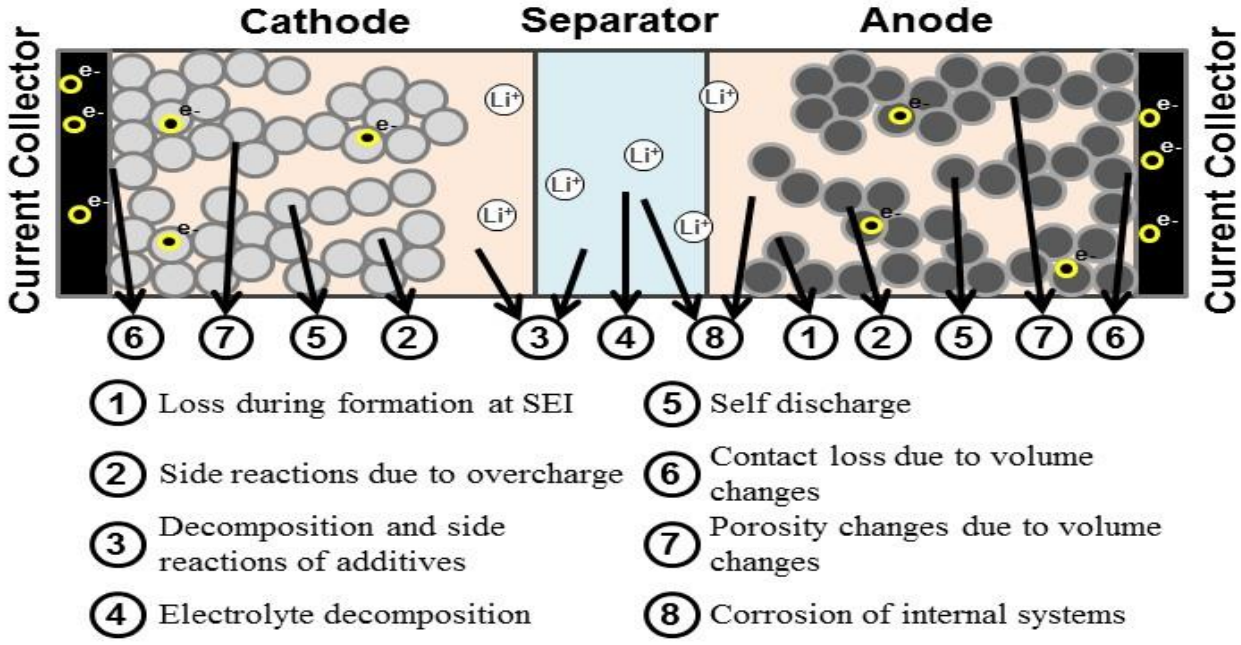

Figure 2.8: The Interphase layer of the Electrolyte oxidation of the Li-Ion

2.5 Overview of Battery Terminologies and Definitions.

Battery technologies used to describe the parameters, characteristics and properties of a battery cells are as follows:

2.5.1 Cell, Modules and Packs

Electric Vehicles (EVs) contain a high voltage battery pack that consists of two or more modules; each module consists of two or more cells. A cell is the smallest unit connected in parallel or in series to form one module. A module is then connected in a parallel or series configuration to form one pack.

2.5.2 Charge Rate (C-Rate)

Battery charge rate or as denoted by C-rate describes the rate at which the battery is charged or discharged relatively to its maximum capacity. A 1C rate means that the applied discharge current will discharge a fully charged battery in $1hr$. For a battery with a capacity of $20Amp-hours$, this equals to a 20Amps discharge current. A $5C$ rate for this battery would be $20x\ 5 = 100\ Amps$, and a C/2 rate would be $20/2 = 10\ Amps$.

2.5.3 Terminal Voltage (Vt)

The voltage measured between the battery terminals when a load is applied.

2.5.4 Open-Circuit Voltage (VOC)

The voltage measured between the battery terminals when no load is applied. The open circuit voltage alone can provide essential information about the battery when is tested. For a Lithium-ion battery the open circuit voltage is the key quantity to determine the State of Charge (SOC) of the cell, given in its steady state. The accuracy hereby depends on the characteristics of the voltage over OCV.

2.5.5 Capacity or Nominal Capacity

The coulometric capacity is the total Amp-hours that can be drawn from a battery when being fully discharged from 100% state-of-charge to its rated minimum cut-off voltage at a certain discharge current (specified as a C-rate). Capacity is calculated by multiplying the discharge current (in Amps) by the discharge time (in hours)

2.5.6 State of Charge (SOC)

In electric vehicles, a key parameter is the State of Charge (SOC) as it shows the current battery capacity as a percentage of maximum capacity. As such, it provides a measure of the amount of electric energy stored in a battery. It is analogous to a fuel gauge on conventional internal combustion engine vehicle. State of Charge (SOC) is a dimensionless number between 0 and 1 representing a percentage. It is worth noting that a zero SOC does not mean that the battery is fully empty, only that the battery cannot be discharged anymore without causing some permanent damage (irreversible chemical reaction) to it.

2.5.7 Depth of Discharge (DOD)

The Depth of Discharge (DOD) is the alternative method of indicating the battery State of Charge (SOC), the DOD is the percentage of the battery capacity that has already discharged.

2.5.8 Cut-off Voltage

The minimum allowable voltage at which the battery is known to be empty.

2.5.9 Cycle Life

This is the number of cycles that can be performed before the battery reaches end of Life.

2.5.10 State of Health (SOH)

The state of Health (SOH) indicates a condition in the battery life between the beginning of life (BoL) and end of life in percentage. The BoL of a battery is defined as the point in time when battery life begins. The EoL of battery is reached when the battery cannot perform according to its predefined minimum requirements. For EV applications, the battery manufacturer defines EoL when one of the following conditions has been reached:

i. 80% drop in the battery capacity compared to its rated capacity under reference conditions. This is known as capacity fading.

ii. 80% drop in the battery's maximum power compared to the rated power. This is known as power fading.

2.6 Lithium ion Battery Modelling

For a very long time, there has been extensive research in predicting the battery performance. The major challenges faced when monitoring a battery is the electrochemical devices which exhibit a non-linear behaviour. This non-linear behaviour can be inherent characteristics such as when the battery is charged and discharged and the increase in temperature. There are many kinds of models that are used in achieving the prediction of the battery performance and operation. It is important to know how the parameters of the battery change because regardless of the information provided by the manufacturer of the battery, the battery still changes over time due to degradation and operating conditions. The Battery Management System (BMS) ensures that the operational condition of the battery should be monitored at regular intervals to ensure a longer life span and safety of the battery [27] . The interaction and flow of information of the estimated state of the battery is shown in Figure 2.9.

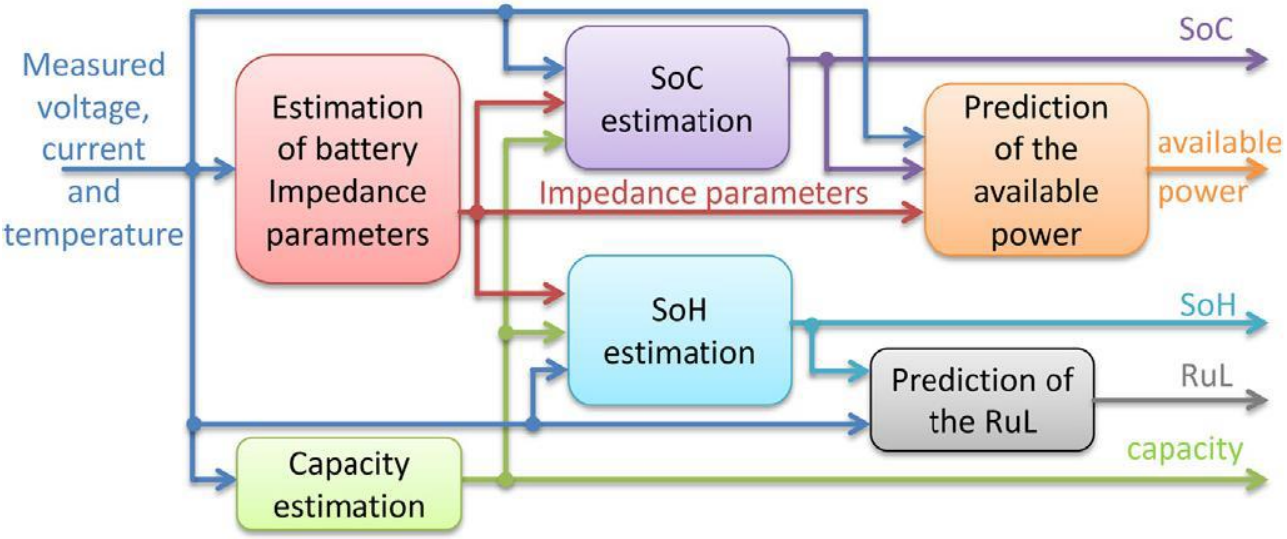

Figure 2.9: The Interaction and flow of Information of estimated state in a BMS [27]

The most important states to monitor the continual operation of the battery is listed and discussed below:

2.6.1 State of Charge (SoC) Estimation

The SoC is a very important parameter of a BMS where individual cells of a battery stack must be estimated accurately. The estimation is usually done in percentage terms. When a battery is at 0% the battery is said to be empty and 100% of the battery indicates a fully charged battery. The state of charge of a battery is therefore defined as the ratio of its capacity in its present state to its fully charged state, and it can be expressed as

$$SoC = \frac{C_{prsent}}{C_{fully\ charged}} \times 100\% \qquad (2.1)$$

The accuracy of SoC estimation of the battery prevent the unexpected interruption of the system when conducting test. The SoC of the battery can also prevent the battery from over discharging or over charging which could lead to internal damage of the battery.

2.6.2 Available Power Estimation

Another important task of a BMS is to estimate the maximum available discharge and charge power and make it reliable over the whole range of SoC estimations. The available power estimation represents the battery capability to perform a task, i.e. to deliver a certain amount of energy over a certain time frame. Prediction of available power at a given time would fall into this state. This state is very dependent on the internal impedance of the battery.

2.6.3 State of Health Estimation

The State of Health of a battery is one of the major parameters which must be monitored constantly. The BMS system runs a continuous diagnosis on the cells within the battery pack to observe a set of scenarios. It compares whether the voltage, current and temperature levels of the cells in the pack are intermediated levels or fluctuating from one another with a certain non-permissible margin. SoH of the battery is of paramount significance for averting unexpected failure from gradual capacity fading. As the battery lifespan decreases, its ability to deliver power also decreases. The relationship between SoH is given by the ratio of the current capacity to the capacity of the battery when it was new. This is expressed in the equation.

$$SoH = \frac{C_{battery}}{C_{new}} \times 100\% \tag{2.2}$$

2.6.4 Remaining Useful Life (RUL)

Remaining useful life is a derivative of the SoH prediction, and this denotes the estimated remaining lifetime of the battery under the current operating conditions before the available capacity has fallen below a certain End-of-Life threshold.

2.7 Literature Review of Battery Models

In this section a brief overview of some basic battery models is discussed. It is important that a proper model is defined for the electrochemical system. The battery modelling can be broadly categorized into 3 categories, namely Electrochemical models, Mathematical models and Electrical models (Equivalent Circuit). The choice of model for a battery is dependent on what parameters are being tested. A trial-and-error determination of battery design parameters and operating conditions is inefficient, which has motivated the use of battery model to numerically optimized battery designs. A high simulation times has limited the application of battery optimization based on physics-based models. Mathematical

models of Lithium-ion batteries vary widely in terms of complexity, computational requirements, and reliability of their predictions [28].

2.7.1 Electrochemical Models and Mathematical Models

Electrochemical models link the physical parameters to the internal electrochemical dynamics of the cell which allows trade off analysis and high accuracy. The electrochemical model is also known as the mathematical model because of the involvement of partial differential equations that relate the different relationships between the open circuit potential and the Lithium-ion concentration with the cell, the conservation charge as well as the Butler-Volmer kinetics. The advantage of electrochemical (Mathematical) modelling of a battery is that it can relate the design parameters to macroscopic information as well as the physical design aspect. It is also highly accurate when compared to the other type of models. The disadvantage of the electrochemical model computationally intensive due to the complex numerical algorithms while also requiring specific battery information, that is difficult to obtain due the propriety nature of the battery.

2.7.2 Electrical (Equivalent Circuit) Models

Electrical models are a visual variant model which makes the model a popular choice of use without having to know the electrochemical process of the battery. The aim to use this model is to reproduce the voltage behaviour under load by replacing the mathematical laws of electrochemistry by electric circuit equivalents. The advantage of this model is that it can be simulated as part of the embedding circuit. Electrical model unlike the mathematical (electrochemical) makes use of linear passive elements [29] which uses a combination of voltage sources, resistors and capacitors for design with other electrical circuits and systems. The equivalent circuit model generally fails to describe the intrinsic battery performance states. In an attempt to account for these, various equivalent circuit models have been proposed consisting of the combinations of the linear passive element and the ideal voltage source which is parameterised by interpolating ore-stored data of the electrode potential making this model strongly dependent on the qualities of its prior parameterisation. There are three examples of circuits with pre-populated voltage sources. These are the RINT model, the Thevenin model and the RC model [30].

i. The RINT model

The RINT model uses a complex circuit network to simulate a battery. It consists of an ideal voltage source V_{oc} populated by the open -circuit voltage data and an internal resistance, both functions of temperature. A potential difference between the cell terminal reflects the terminal voltages $V_{battery}$ under the application of a current $I_{battery}$. The disadvantages of the RINT model are its strong dependency on pre-populated and limited applicability in real world dynamic operating conditions. The RINT circuit model diagram is shown in Figure 2.10

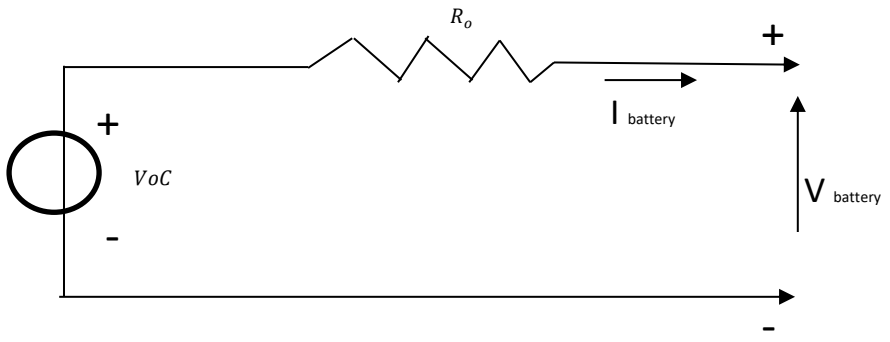

Figure 2.10: The RINT Circuit Model

$$V_{battery} = V_{oc} - I_{Battery}R_o \tag{2.3}$$

ii. ***The Thevenin circuit model***

The Thevenin model uses the simplest combination of a parallel-series arrangement of a constant resistor and capacitor elements. An ideal battery represents the open circuit voltage source V_{oc} which is arranged in series with the internal resistance and a parallel couple C_{th} and R_{th}, contributing to the transient capacitive response and polarisation overpotential resistance respectively. It is assumed that the open circuit voltage is constant. The Thevenin based equivalent circuit is shown in Figure 2.11.

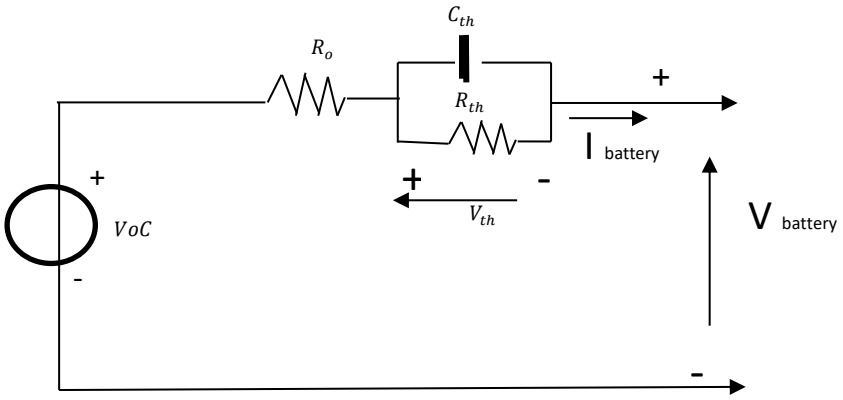

Figure 2.11: The Thevenin Based Equivalent Circuit

The Thevenin equivalent circuit can be expressed as:

$$V_{battery} = V_{oc} - V_{th} - I_{Battery}R_o \tag{2.4}$$

Where

$$V_{battery} = -\frac{V_{th}}{R_{th}C_{th}} + \frac{I_{Battery}}{C_{th}} \tag{2.5}$$

iii. ***The RC circuit model***

The RC circuit model combines capacitive and resistive elements to achieve battery characteristics behaviour under load. Two capacitors and three resistors are arranged as shown below. This model was created in the attempt of associating a physical meaning to each electric element. Electrochemical reaction capacitance (more specifically double-layer capacitance) is represented by a small capacitor C_c. The remaining battery capacity is represented by the C_b. The RC circuit model diagram is shown Figure 2.12.

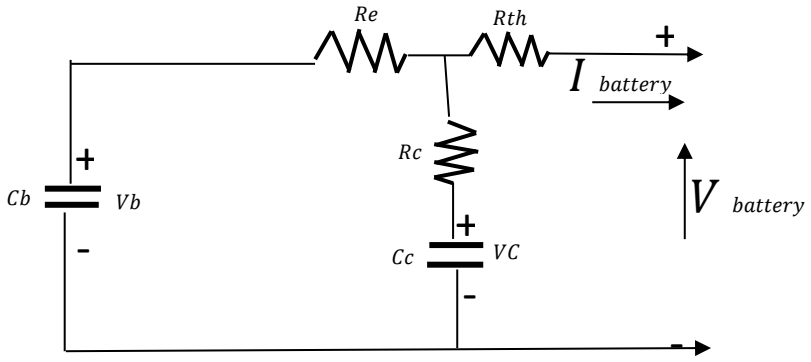

Figure 2.12: The RC Circuit Model

The equivalent RC model is expressed below

$$\left[V_{battery}\right] = \left[\frac{R_c}{R_c+R_e} \quad \frac{R_e}{R_c+R_e}\right] \begin{bmatrix} V_b \\ V_c \end{bmatrix} + \left[R_{th} - \frac{R_c}{R_e+R_c}\right] \left[I_{battery}\right] \tag{2.6}$$

3. Battery testing techniques

There are various ways of testing a battery in determining the state of the battery. These various techniques will be discussed briefly in this section.

3.1 Static capacity test

This is an offline test which is carried out during the charging and discharging of the battery. This illustrates the non-linear relationship between the capacity/SOC and the voltage of the cell [6].

3.2 Open circuit voltage SOC estimation

This is a common test that involves the SoC of the battery to determine how much the energy the battery system can still deliver before a recharge is required. This is a very simple method that has a high accuracy. However, it has a major drawback of allowing the battery to be at a state of rest for a very long time before the OCV can be measured accurately [31].

3.3 Coulomb Counting

This is another battery testing technique used in estimating the SOC. It has a major benefit of being computationally simple for a microcontroller. It works by integrating the current of a battery over a particular time frame during a charge or discharge of the battery. The major drawback of the coulomb test is that the inaccuracies in measurement result in an accumulative inaccuracy over time [31].

3.4 Impedance testing methods

The battery characterization is an important parameter as it is directly related to the power capability of the cell, and therefore the SoF. Impedance is often used to obtain a model of the electrochemical systems. Impedance is not directly measurable quantity of the battery and must be estimated by other means (i.e. from voltage and current measurement). The impedance testing model of the battery, however, demonstrates a non-linear behaviour as it is dependent on the SoH, temperature and the discharge rate of the cell [32]. There are a variety of tests that are used to classify the impedance at various operating points. The impedance of a cell can be used to obtain other information related to its state. The impedance spectroscopy technique parameterizes battery impedances, because the battery impedance varies for different conditions such as: SoC, SoH and temperature. The impedance testing makes it possible to measure very slow battery dynamics. Its extracted parameters derived from the electrical

model are closely associated with the physicochemical processes [33]. The impedance testing method was used to carry out testing on a Lithium-ion battery and is discussed extensively in the section below.

3.5 Electrochemical Impedance Spectroscopy

Electrochemical Impedance Spectroscopy [EIS] is a method of characterizing the battery's impedance at a various frequency. The EIS is an electro-analytic technique applied to batteries for the investigation of not only electrochemical kinetics but also characterization under different conditions. EIS is a method which applies sinusoidal current or voltage to a cell and records its response which is a sinusoidal amplitude as well as phase shift.

3.5.1 Introduction

EIS techniques has major two types of modes which is used to determine the impedance of the battery, the Galvano-static and the potentio-static mode of operations. In galvanostatic mode of operation, a current signal is injected, and the voltage response is measured. In potentio-static mode, a voltage perturbation signal is used, and the current response is measured. Galvanostatic mode is usually preferred when measuring the impedance of a battery, majorly because it is a constant voltage device and it is easier to draw varying load currents at the same SoC. EIS in galvanostatic mode involves injection of small current perturbation and measurement of the corresponding voltage response [34] [35]. The injected current and voltage response can be represented mathematically as given in (3.1) and (3.2), while the corresponding impedance is determined at each frequency using the ohmic relationship as given in (3.3) [36].

$$\Delta I = I_{max}(sin\ 2\pi f_t) \tag{3.1}$$

$$\Delta V = V_{max}(sin2\pi f_t + \emptyset) \tag{3.2}$$

$$Z = \frac{V_{max}(sin2\pi f_t + \emptyset)}{I_{max}(sin\ 2\pi f_t)} \tag{3.3}$$

The terminal voltage and current of the battery exhibits a non-linear internal characteristic. Impedance variation can only be defined for a non-linear system if the requirement of system linearity is met. Therefore, it is very important for the system to operate in a linear region for an impedance estimate to be used. The linearity condition of the battery can be achieved, if the EIS is conducted at a fixed operation with a small excitation for the conditions of casualty, linearity and stability to be met. When operating the battery in linear region the state of charge and the temperature of the battery should not vary

significantly during the measurement of impedance. The impedance is measured over a certain frequency range. The obtained impedance variation is then used to produce a Nyquist representation as shown in Figure 3.1

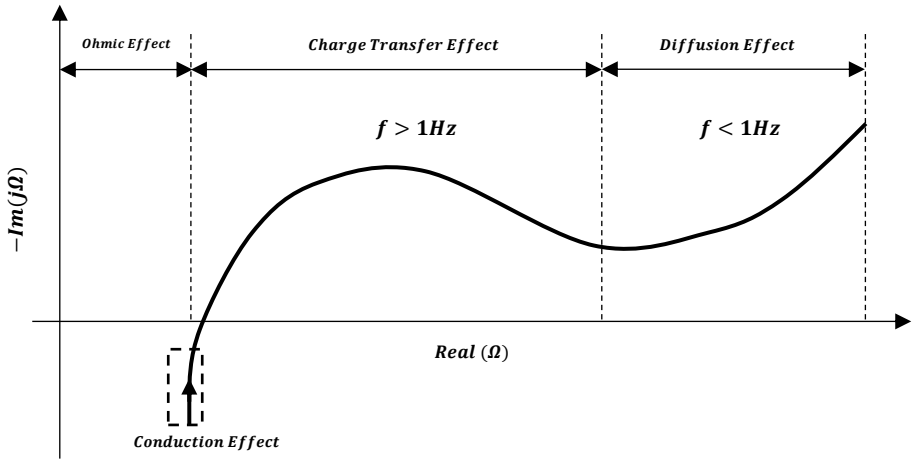

Figure 3.1: Typical Nyquist Spectrum

From Fig. 3.1, it can be observed that the impedance measurement obtained over a lower frequency range ($f < 1Hz$), is used to describe the diffusion effect within the cell which is represented by a slope of 45^o. While the semi-circular is the region representing the charge transfer effect. The ohmic effect is due to the cell electrode and can be observed at the point where the impedance spectra intersect the real axis. The conduction effect observed at high frequencies describes the high frequency inductive effects of the cell electrodes and not the internal process of the battery [7].The measured battery impedance data are fitted to a linear model of the cell impedance. This is then used to extract the parameters of the battery, using an appropriate AC equivalent electric circuit (AC-EEC), that best describes the Nyquist plot and the internal process of the battery. The generalized Warburg impedance model for a Lithium-ion battery is used in this work as shown in Figure 3.2. Variation of the internal process of the battery can thus be observed, using the variation of the AC-EEC parameters. Where, R_s, C_{dll}, R_p and Z_w represent series resistance, double layer charge transfer, internal shunt resistance and Warburg impedance, respectively [7].

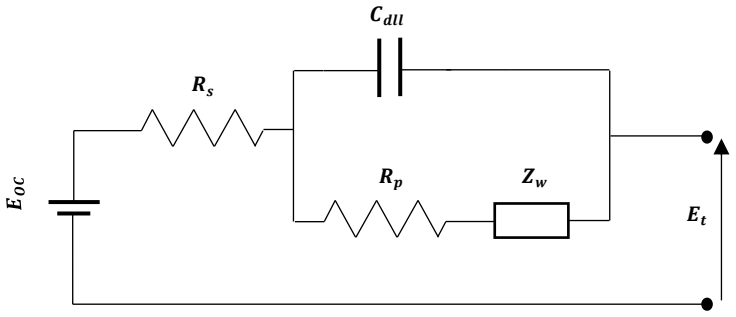

Figure 3.2: Lithium-ion Battery first order equivalent circuit

The AC-EEC representation is quite useful considering the battery impedance measurements because internal impedance varying response to different frequencies which is later discussed in this research.

3.5.2 Excitation Signals

Measurement of the input and output in (3.3) during charging and discharging of the battery does not give information about the internal impedance of the battery. Information of the battery can be achieved by perturbating the battery with an excitation signal and measuring the changes in current and voltage. Different excitations signal have a different impact on the result collected from the impedance measurement. To extract the desired content of the system, excitation signal needs to be carefully designed. A principal block diagram of an excited system is shown Figure 3.3.

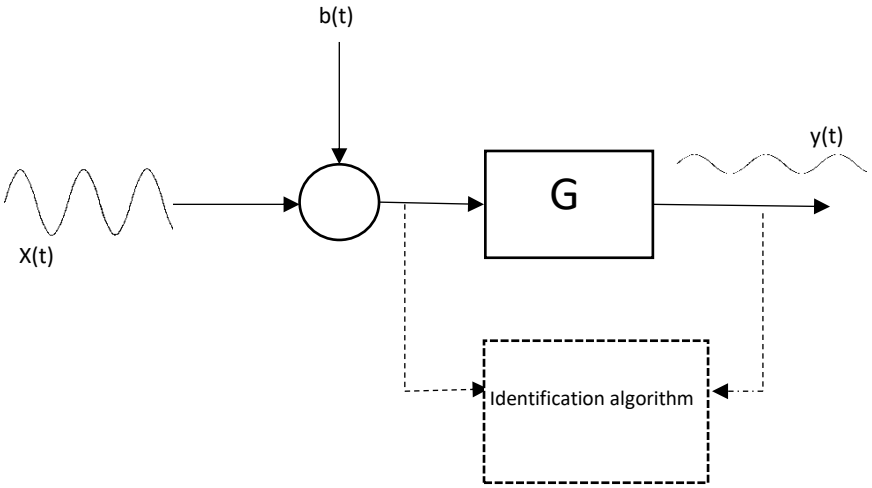

Figure 3.3: System Frequency response measurement with the use of external signal

Where $x(t)$ is the input, $y(t)$ output of the system and $b(t)$ is the excitation injection which is depended highly on the application. Because battery is realized as a voltage source, battery current is the quantity that should be perturbed and thus perturbation is located as the input side in the figure above. Excitation of signal can be done either by injecting a single frequency at a time (EIS) or by injecting multiple frequencies at a time (BIS). In this thesis, injection of a single frequency at a time was implemented to perform EIS and it is explained in the next section.

3.5.3 Sine Sweep

In the Sine sweep method, the perturbation is a sine wave with only the fundamental frequency as frequency content. The mathematical expression for this is expressed as

$$x(t) = Asin(2\pi ft) \tag{3.4}$$

The sine sweep has a quite high Signal to Noise Ratio (SNR) since only one frequency is swept at a time. SNR can also be increased up to a certain point by increasing the amplitude A of the excitation. It is also suitable for analysis of non-linear systems since its harmonic content is directly visible [37]. Significant drawback is that each frequency must be injected separately which increases the measurement time. Sine wave is also difficult and heavy to implement digitally since it has characteristics of continuous signal whereby numerous bits are required to estimate discretely. Sine function is widely used in EIS measurement. However, in this thesis injection of signal was done in both offline measurement and online measurement.

3.5.4 Impedance measurement

Battery measurements in this research are implemented using a sine sweep excitation signal. The measurement is done in offline and online implementation. For the offline implementation it requires an expensive and a bulky Frequency Impedance Analyser (FRA). The use of the bulky and expensive equipment can be done away with by implementing the measurement online by substituting the FRA with a power converter.

3.5.4.1 Offline Measurement

The offline measurement is usually carried out by using a bulky frequency impedance analyser.

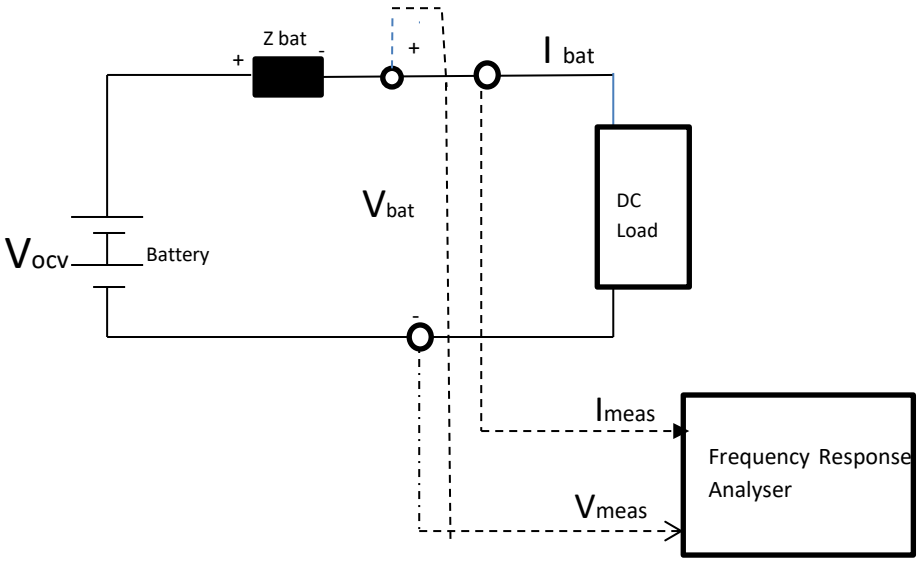

Figure 3.4: Schematic representation of Impedance measurement setup of the battery using FRA.

The V_{OCV} is the open-circuit voltage of the battery, Z_{batt} is the internal impedance of the battery and the V_{bat} is the voltage between the battery terminals which is different from V_{OCV} when the battery draws any currents. Excitation signals are perturbed into the circuit as current reference I_{ref} to the DC-load device that draws a current which is the same as the battery current. Current and terminal voltage of the battery are measured with a high-resolution current and voltage probe and using the FRA. Measurements on FRA are only carried out by means of discharging the battery.

3.5.4.2 Online Impedance Measurement

Online impedance measurement can be implemented using linear amplifiers for injecting the AC perturbations or using the associated power converter that interfaces the battery and the load to inject signals through duty cycle perturbations. The major disadvantage of using a linear amplifier for injecting signals is that the linear amplifier is dependent on the battery bank and a large power is required to produce the current stimuli. The power losses are also high due to the heat in the linear amplifier [38].

The aim of this dissertation is to perform impedance spectroscopy measurements without disconnecting the battery from the system or interrupting the system operation. The results obtained from the online impedance measurements can be used by the Battery Management System (BMS) to determine the state of the battery. EIS can be performed on a switching converter by superimposing a sinusoidal perturbation onto the duty cycle [38]. In [39] a conventional DC-DC boost/buck converter was used in implementing EIS. The perturbation signal was superimposed during charging and discharging of the Li-ion battery while varying the duty cycle of the converter, instead of using external linear signal generator [39].

3.5.5 Converter Topology for the DC-DC Converter

DC-DC converter serves as an interphase between the battery energy storage system and the inverter DC-link. It must regulate the battery voltage level suitable for the DC-link and carry out the control strategies for charging and discharging the battery. Converters need to have minimal current ripples in order to avoid unwanted noise.

Appropriate comparative study among some bidirectional DC-DC converters is introduced. Topologies that will be compared are the conventional Boost Converter and two leg Interleaved converter. The topologies are discussed in the section below.

i. Boost Converter Topology

The word BOOST means to 'step up'. From the literal meaning, we can say a Boost converter, is a step-up converter which steps up a low input voltage to a high output voltage by periodically opening and closing an electronic switch. The converter consists of a diode, a MOSFET as a switch and an energy storage element. A capacitor is usually added to the output of the circuit to perform the function of removing the output voltage ripple and sometimes inductors are also combined with it [35]. The schematic diagram, of a conventional boost converter is shown in Figure 3.5.

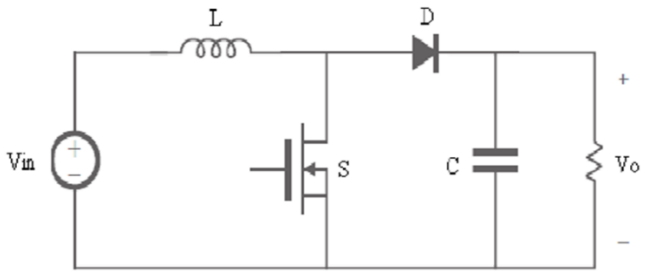

Figure 3.5: Schematic diagram of a conventional boost converter

A conventional boost converter is used for EIS because of the continuous input current across the inductor which is enough for EIS in battery applications. In [7], the boost aspect of a conventional buck-boost converter was used to implement EIS on a Lithium ion battery. It was then demonstrated that EIS can be performed on a switching converter by varying the duty cycle. Small signal analysis can be used to create a feedforward control to create accurate perturbations in the inductor current on the switching converter. These inductor current perturbations were effective at creating a battery voltage response, so that impedance could be measured. The results of the EIS performed by the DC-DC boost converter system was shown to be slightly less accurate compared to the FRA result in [7]. The disadvantage of using a boost converter for the EIS implementation on the battery, is the high current ripple which affects the perturbation signal that is being injected in the duty cycle. The conventional boost cannot be used for high voltage applications due to the voltage stress across the switch.

ii. Interleaved Boost Converter

Because of the drawback of the conventional DC-DC boost converter, an interleaved boost converter was proposed. Interleaved boost converters have been studied in recent years with the goal of improving power converter performance in terms of conducted electromagnetic emission and transient response. Higher efficiency is realized by splitting the output current into 'n' paths, substantially reducing losses, particularly inductor losses. In addition, interleaving is also employed to reduce the input current ripple, and therefore to minimize the size of the input filter that would be relatively large if a single boost converter was used. [40]. The diagram of a two-phase interleaved boost converter is shown in Figure 3.6. It contains inductor L1 in parallel with inductor L2, switch Q1 in parallel with another switch Q2, diode

D1 in parallel with diode D2, thereby forming two parallel channels between input and output circuits. All identical components are used for the circuit to obtain interleaving operation. Two switches are provided and the gate signal which is out of phase by 180°. The benefits of interleaving include high power capability, modularity, and improved reliability. Interleaving add benefits such as reduced ripple current in both input and output circuits. The current ripple of the interleaved boost converter is reduced by the gate shift and this helps in performing EIS implementation.

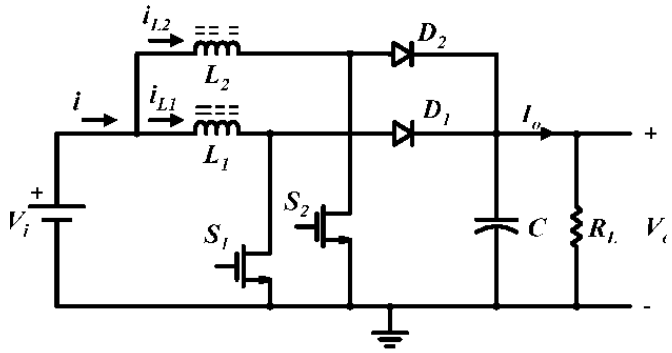

Figure 3.6: schematic circuit diagram of a two-leg interleaved converter

The two-legged interleaved DC-DC Converter topology was proposed to keep the current ripple to a minimum, such that the battery health is not affected. The controller for controlling the charge or discharge of the battery was used to produce a small perturbation required for the impedance measurement. The two-legged interleaved DC-DC converter analysed the ability of the DC-bus voltage on the ability to generate small amplitude perturbation. The drawback of this topology when implementing EIS is that it has more delay and phase error because of all its components, therefore the impedance measurement will no longer be accurate.

3.6 Chapter summary

Batteries are expensive devices that need to be maintained in order to improve their lifespan. This chapter has reviewed the most widely used methods to monitor a battery's health. The static capacity test is an offline test that shows the battery's relationship between its capacity and state of charge, but its major drawback is the change of temperature and discharge rate over a period of time. The open circuit voltage estimation shows the relationship between a battery's state of charge and its energy. Although it provides more accurate results than the static capacity test, it is an expensive and time-consuming test. The Coulomb counting state of charge monitoring method solves the time constraint of the open circuit voltage estimations technique by making use of digital implementation but has the problem of having inaccuracies due to the conversion between analogue and digital signals. Impedance

spectroscopy (IS) solves the problem of accuracy and time rate. The IS can be used to obtain state of information of the battery. Offline IS method using FRA's however, is an expensive option but the use of power converters to replace the FRA is a much cheaper option but it is not as accurate as the FRA. Not all power converters give the best results for IS: the boost converter gave good results but suffered from high frequency ripples in the input current. Interleaved converters were used to solve the ripple issue, however, they are limited in applications because of the cost associated with these converters.

4. The three-level boost converter

The topology overview and analysis of the three-level boost converter is presented.

4.1 Topology overview

The three-level boost converter, as shown in Figure 4.1, is a converter that has the same voltage transfer characteristics as a conventional boost converter. Unlike a conventional boost converter which has two voltage levels, the three-level boost converter has three different voltage levels. It has 1 input inductor, 2 switches, 2 output filter capacitors and 2 diodes.

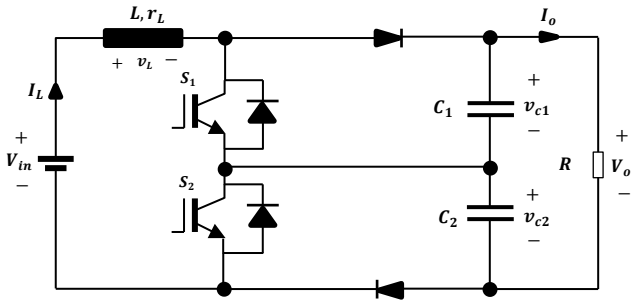

Figure 4.1: The three-level boost converter

Like interleaved boost converters, the three-level boost converter reduces the input current ripple by switching the two switches, S_1 and S_2 180^o out of phase. Unlike interleaved converters however, the three-level only uses 1 inductor to achieve the ripple reduction. Because of the inverse relationship between the average current of an inductor and its inductance, the interleaved converter has higher inductance values than the three-level converter, this means that the cost of the three-level converter is lower than that of an interleaved. The converter also reduces the ripple at the output voltage without using large capacitors but rather shifting the phase of the capacitors' ripple by 180^o, thereby reducing the overall output voltage ripple. The average value of the two capacitors C_1 and C_2 sum up to the output voltage, as a result the voltage stress on the switches is reduced by half – hence, the converter can be used for high voltage applications.

4.2 Operational analysis

The converter has 4 modes of operation, as shown in Table 4-1. Modes 1 and 4 are the same as a conventional two-level converter.

Table 4-1: Three-level boost converter modes of operation

Mode	S_1	S_2
1	OFF	OFF
2	OFF	ON
3	ON	OFF
4	ON	ON

During mode 1, switches S_1 and S_2 are both in their ON state as shown in Figure 4.2 (a). The inductor L charges through the switches. Both the diodes are reverse biased. The capacitors discharge through the load as illustrated by equation (4.1):

$$\left.\begin{aligned} \frac{d}{dt}I_L &= \frac{V_{in}}{L} \\ \frac{d}{dt}v_{c1} &= -\frac{v_{c1}}{R_L C_1} \\ \frac{d}{dt}v_{c2} &= -\frac{v_{c2}}{R_L C_2} \end{aligned}\right\} \tag{4.1}$$

Where, I_L is the inductor average current; V_{in} is the input voltage; v_{c1} is the voltage across capacitor C_1; and v_{c2} is the voltage across capacitor C_2.

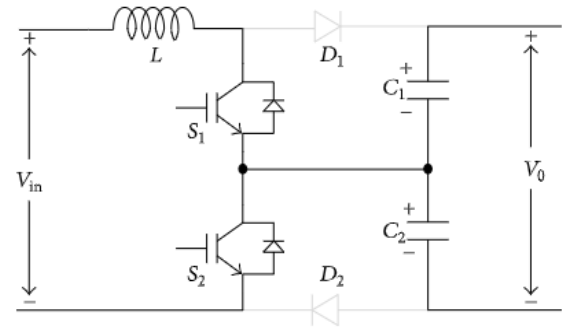

(a)

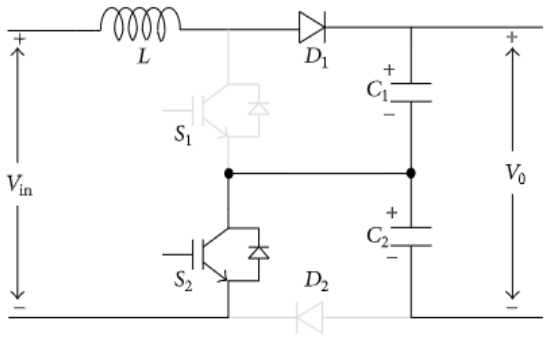

(b)

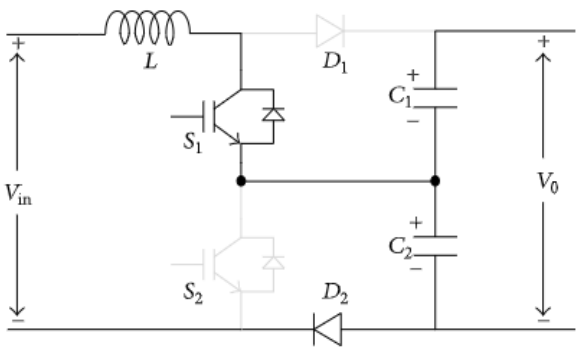

(c)

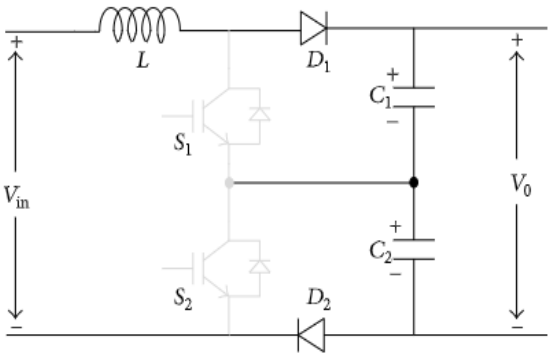

(d)

Figure 4.2: Three-level boost converter modes of operation equivalent circuits (a) Mode 1 (b) Mode 2 (c) Mode 3 (d) Mode 4 [41]

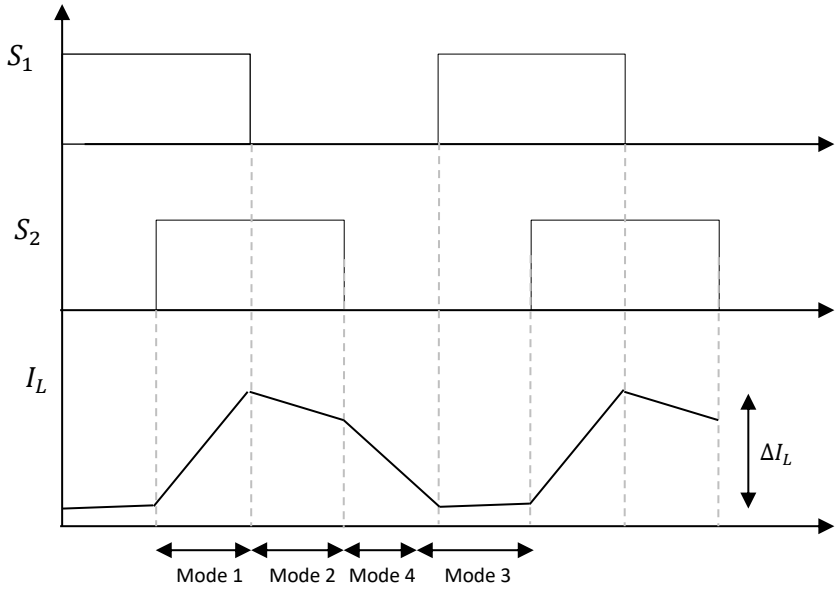

Figure 4.3: Inductor current ripple in continuous inductor current mode (CICM) and 50% duty cycle

In Mode 2, switch S_1 is in its OFF state while switch S_2 is in its ON state as shown in Figure 4.2 (b). Since the voltage across the inductor is $v_L = V_{in} - v_{c1}$. The inductor can therefore be either charging or discharging depending the voltage across the capacitor C_1 – which is charging. The capacitor C_2 is discharging through the load as illustrated by the system of equations

$$\left.\begin{aligned} \frac{d}{dt}I_L &= \frac{V_{in} - v_{c2}}{L} \\ \frac{d}{dt}v_{c1} &= \frac{I_{L.}R_L v_{c1}}{R_L C_1} \\ \frac{d}{dt}v_{c2} &= -\frac{v_{c2}}{R_L C_2} \end{aligned}\right\} \tag{4.2}$$

Figure 4.2 (c) shows Mode 3 in which switch S_1 in its ON state while S_2 is OFF. The voltage appearing across the inductor is $v_L = V_{in} - v_{c2}$ and the inductor can charge or discharge depending on the voltage across capacitor C_2 described by the system of equations given by

$$\left.\begin{aligned} \frac{d}{dt}I_L &= \frac{V_{in} - v_{c1}}{L} \\ \frac{d}{dt}v_{c1} &= -\frac{v_{c1}}{R_L C_1} \\ \frac{d}{dt}v_{c2} &= \frac{I_L R_L - v_{c2}}{R_L C_2} \end{aligned}\right\} \tag{4.3}$$

Figure 4.2 (d) shows Mode 4 where the inductor is discharging because the voltage appearing across both capacitors is larger than the input voltage; while the capacitors are charging [41]. The system of the equations is given:

$$\left.\begin{aligned} \frac{d}{dt}I_L &= \frac{V_{in} - v_{c1} - v_{c2}}{L} \\ \frac{d}{dt}v_{c1} &= \frac{I_L R_L - v_{c1}}{R_L C_1} \\ \frac{d}{dt}v_{c2} &= \frac{I_L R_L - v_{c2}}{R_L C_2} \end{aligned}\right\} \tag{4.4}$$

The converter has two regions of operation which are governed by the duty cycle i.e.

$$\left.\begin{aligned} Region\ 1: &\quad 0 \le d \le 0.5\ or\ V_o \ge 2V_{in} \\ Region\ 2: &\quad 0.5 < d \le 1\ or\ V_o < 2V_{in} \end{aligned}\right\} \tag{4.5}$$

In each region, the voltage has 3 different voltage levels. In Region 1, the inductor is charging since the input voltage is always greater than half the output voltage. In Region 2, the inductor is discharging since the input voltage is always less than half the output voltage.

4.3 Ideal power transfer

In this work, the converter was operated in Conduction Inductor Current Mode (CICM), hence the power transfer will be during this mode of operation. In this mode, the inductor current is not allowed to reach zero and maximum power is transferred to the load, with minimal losses. The inductor is assumed to have no dc resistance and the output current is assumed to have an average of zero. The converter transfers its power through the inductor, as such, the average voltage across the inductor is given by:

$$\int_0^{T_s} V_L\, dt = 0 \tag{4.6}$$

$$\int_0^{dT_s} V_{in}\, dt + \int_{dT_s}^{T_s} (V_{in} - v_{c1} - v_{c2})\, dt = 0 \tag{4.7}$$

Assuming that the capacitors have balanced voltages, $v_{c1} + v_{c2} = V_0$.

$$dV_{in}T_s + (V_{in} - V_0)(1 - d)T_s = 0 \tag{4.8}$$

Where, d is the averaged duty cycle; and T_s is the switching period. Evaluating (4.8) for the voltage transfer ratio gives:

$$\frac{V_0}{V_{in}} = \frac{1}{1-d} \tag{4.9}$$

If the input power of the converter is assumed to equal the output power, then:

$$\frac{I_o}{I_{in}} = 1 - d \tag{4.10}$$

Which is the current transfer ratio for the converter.

4.4 Converter ripple analysis

In impedance spectroscopy, the current ripple is required to be as small as possible. This is to ensure that the small ac signal injected and its response can be measured without the use of expensive filters. The three-level boost converter's input current and output voltage ripple were analysed.

4.4.1 Input current ripple

The converter has two regions of operation as defined by (4.5). The converter's input current ripple was analysed in Region 1, then Region 2 and subsequently represented graphically. Using (4.2) and (4.3), in Region 2, the inductor current ripple is given by:

$$\Delta I_L = \frac{V_o(2D-1)}{Lf_{sw}} \tag{4.11}$$

Where, f_{sw} is the switching frequency of the converter. In this region the voltage appearing across the capacitor C_1, is half the that of the output voltage i.e.

$$D = 1 - \frac{V_{in}}{V_o} \tag{4.12}$$

Simplifying (4.12),

$$\Delta I_L = \frac{V_o\left(1-\frac{V_{in}}{V_o}\right)\frac{V_{in}}{V}_o}{Lf_{sw}} \tag{4.13}$$

Solving (4.9) for the output voltage and substituting the result into (4.13),

$$\Delta I_L = \frac{\frac{V_{in}}{1-D}\left(1-\frac{V_{in}}{1-\frac{V_{in}}{1-D}}\right)\frac{V_{in}}{1-\frac{V_{in}}{D}}}{Lf_{sw}} \tag{4.14}$$

Simplifying (4.14),

$$\Delta I_L = \frac{V_{in}}{1-\left(1-\frac{V_{in}}{V_o}\right)}\left(\frac{\left(1-\frac{V_{in}}{1-\frac{V_{in}}{1-\frac{V_{in}}{V_o}}}\right)\left(\frac{V_{in}}{1-\frac{V_{in}}{1-\frac{V_{in}}{V_o}}}\right)}{Lf_{sw}}\right) \tag{4.15}$$

Finally,

$$\Delta I_L = V_o\left(\frac{\left(1-\frac{V_{in}}{V_o}\right)\left(\frac{2V_{in}}{V_o}-1\right)}{Lf_{sw}}\right) \tag{4.16}$$

In Region 1, equations (4.1) and (4.4) were used. The ripple inductor obtained was,

$$\Delta I_L = \frac{V_{in}}{Lf_{sw}}(1-2D) \tag{4.17}$$

Using (4.16) and (4.17), the inductor current ripple was then normalized with respect to:

$$V_o = \frac{\left(\frac{V_{in}}{V_o}\right)\left(1-\frac{2V_{in}}{V_o}\right)}{Lf_{sw}} \tag{4.18}$$

The resulting input inductor current ripple was then:

$$\Delta I_L = \begin{cases} (1-D)(2D-1), & 0.5 \le d \le 1 \\ D(1-2D), & 0 < d \le 0.5 \end{cases} \tag{4.19}$$

The ripple was then represented graphically to illustrate the ripple comparison between the two level and three level boost converters.

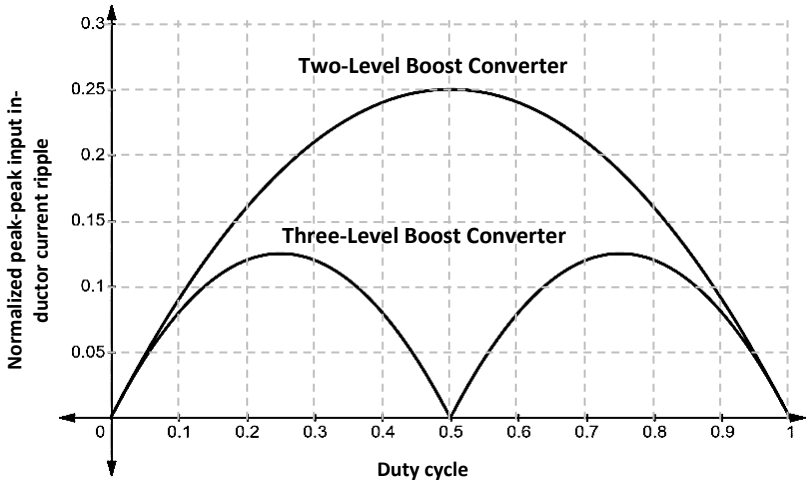

Figure 4.4: Peak to peak input current ripple comparison between the conventional two-level and three-level converters

Under the same operating condition of both the conventional boost and the three-level boost converter, Figure 4.4 shows that the three-level boost converter clearly offers better ripple current reduction when compared to the conventional boost converter. At 50% duty cycle the input current results in a near zero normalized peak-peak ripple. The three-level boost converter also shows a smaller peak ripple that is about half of the two-level boost converter. This implies that if this converter is applied for EIS implementation, the integrity of the measured signal ripple can be ensured.

4.4.2 Output voltage ripple

The three-level boost converter also reduces the output voltage ripple without the use of a large filter capacitor. This ripple was also analysed in both Regions 1 and 2. From (4.2) and (4.3), the ripple in Region 2 it was resolved to be:

$$\Delta V_o = \frac{V_{in}(2D-1)}{2(C_1+C_2)f_s R_L} \tag{4.20}$$

In Region 1, the output voltage ripple was resolved to be:

$$\Delta V_o = \frac{V_{in}(1-2D)}{2(C_1+C_2)f_s R_L} \tag{4.21}$$

The resulting output voltage ripple of the converter was obtained to be:

$$\Delta V_o = \frac{V_{in}}{2(C_1 + C_2) f_s R_L} \begin{cases} (1-D)(2D-1), & 0.5 \leq d \leq 1 \\ D(1-2D), & 0 < d \leq 0.5 \end{cases} \tag{4.22}$$

The ripple was then represented graphically as shown by

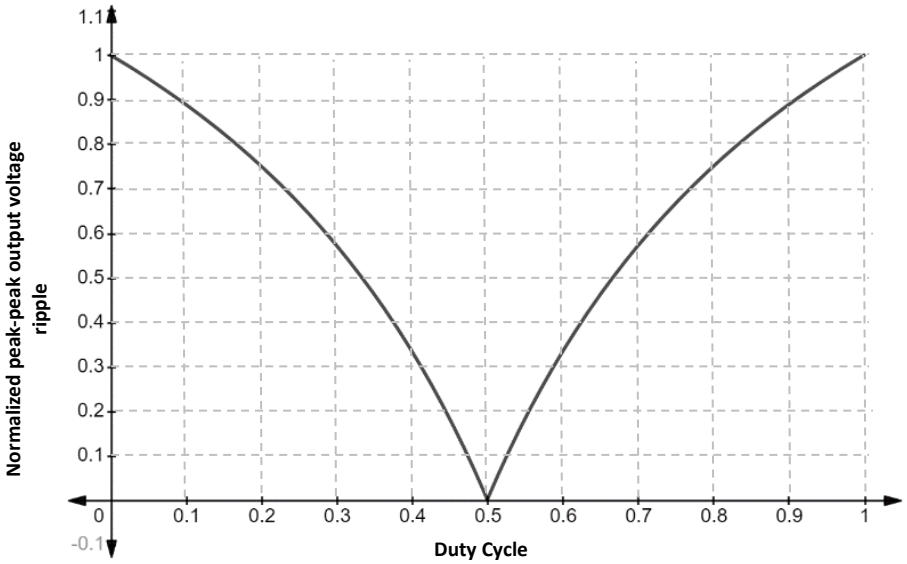

Figure 4.5: Three-level boost converter output voltage ripple at 50% duty cycle – with balanced output capacitor voltages.

Because of the voltage balancing of the output capacitors, the voltage ripple at the output is minimal at 50% duty cycle operation. The output capacitors' ripples are out of phase by 180^o and share the output voltage ripple equally and hence, reducing the output voltage ripple.

4.5 Active switch stress

One of the main drawbacks of a conventional two-level boost converter is that, it exhibits high voltage stress. This limits its capabilities at high voltage levels. The three-level boost converter's voltage stress was analysed and shown and compared in Region 1 and Region 2. The total stress of any power converter is given by:

$$\delta = \sum_{i=1}^{n} V_{m(i)} I_{m(i)} \tag{4.23}$$

Where, n is the number of switches in the converter; i is the switch number; V_m is the maximum voltage stress across each switch and I_m is the maximum or rms current applied to the switch.

4.5.1 *Voltage stress*

In Region 1, the voltage stress applied to the switch S_1 is:

$$V_{m(1)} = \frac{V_o(1-2D)}{2}(1+\Delta V_{o\%}) \tag{4.24}$$

Where, $\Delta V_{o\%}$ is the ripple voltage ratio given by:

$$\Delta V_{o\%} = \frac{\Delta V_o}{2V_o} \tag{4.25}$$

The voltage applied to switch S_2 is given by:

$$V_{m(2)} = \frac{V_o}{2}(1+\Delta V_{o\%}) \tag{4.26}$$

The voltage stress applied to switch S_2 is larger than that of S_1 as shown by Figure 4.2. Substituting equation (4.20) and (4.25) into (4.24), the voltage stress across switch S_1 becomes:

$$V_{m(1)} = \frac{V_o(1-2D)}{2}\left(1+\frac{\frac{V_{in}}{2(C_1+C_2)f_sR_L}(1-2D)}{2V_o}\right) \tag{4.27}$$

And substituting equation (4.21) and (4.25) into (4.26), the voltage stress across switch S_2:

$$V_{m(2)} = \frac{V_o(1-2D)}{2}\left(1+\frac{\frac{V_{in}}{2(C_1+C_2)f_sR_L}(1-2D)}{2V_o}\right) \tag{4.28}$$

In Region 2, the voltage stress across the switch S_1 is zero but the stress across the switch S_2 is given by:

$$V_{m(2)} = \frac{V_o(2D-1)}{2}(1+\Delta V_{o\%}) \tag{4.29}$$

Substituting equation (4.21) and (4.25) into (4.29):

$$V_{m(2)} = \frac{V_o}{2}\left(\frac{1+\frac{V_{in}}{2(C_1+C_2)f_sR_L}(2D-1)}{2V_o}\right) \tag{4.30}$$

Which is a stress that is less than the stress observed by the switch in Region 1.

4.5.2 *Current stress*

In Region 1, the peak current stress across the switch S_1 was:

$$I_{m(1)} = \frac{I_o}{2}(1 + \Delta I_{L\%}) \tag{4.31}$$

Where, $\Delta I_{L\%}$ is the inductor current ripple ratio given by:

$$\Delta I_{L\%} = \frac{\Delta I_L}{2I_L} \tag{4.32}$$

The current stress across the switch S_1 is given by:

$$I_{m(2)} = \Delta I_{L(peak)} = \frac{I_o}{2}(1 + \Delta I_{L\%}) \tag{4.33}$$

Substituting equation (4.16) and (4.33) into (4.31), the current stress across the switch S_1 was:

$$I_{m(1)} = \frac{I_o}{2}\left(1 + \frac{\frac{V_{in}}{2Lf_s}(D(1-2D)}{2I_L}\right) \tag{4.34}$$

The stress across the switch S_2 is:

$$I_{m(2)} = \frac{I_o}{2}\left(1 + \frac{\frac{V_{in}}{2Lf_s}(D(1-2D))}{2I_L}\right) \tag{4.35}$$

This results from the fact that the switches conduct individually in both states in this region. In Region 2, the current stress across the switch S_1 and S_2 is the same and is:

$$I_{m(1)} = I_{m(2)} = \frac{I_o}{2}\left(1 + \frac{\frac{V_{in}}{2Lf_s}(1-D)(2D-1)}{2I_L}\right) \tag{4.36}$$

This is because in one state both switches are conducting whereas in the other state, they are both off.

4.5.3 *Switch utilization*

The converter switching utilization is defined as the ratio of the load power to the total switch stress for the converter, i.e.

$$U = \frac{P_o}{\delta} \tag{4.37}$$

Where, P_o is the load power. The switch utilization was compared for both Regions 1 and 2. In the 1st region, using equation (4.23), the total switching stress was given by:

$$\delta_1 = V_{m(1)} I_{m(1)} + V_{m(2)} I_{m(2)} \tag{4.38}$$

From equations (4.24), (4.26), (4.31) and (4.33). The total switching stress is given by:

$$\delta_1 = \left(\frac{V_o(1-D)}{2} (1 + \Delta V_{o\%}) \frac{I_o}{2} (1 + \Delta I_{L\%}) \right) + \left(\frac{V_o}{2} (1 + \Delta V_{o\%}) \frac{I_o}{2} (1 + \Delta I_{L\%}) \right) \tag{4.39}$$

Equation (4.39) simplifies to:

$$\delta_1 = \left(\frac{P_o(1-D)}{4} (1 + \Delta V_{o\%})(1 + \Delta I_{L\%}) \right) + \left(\frac{P_o}{4} (1 + \Delta V_{o\%})(1 + \Delta I_{L\%}) \right) \tag{4.40}$$

Finally,

$$\delta_1 = \frac{P_o}{4} (1 + \Delta V_{o\%})(1 + \Delta I_{L\%})(2 - D) \tag{4.41}$$

From equation (4.37), the switch utilization in Region 1 is,

$$U_1 = \frac{4}{(1 + \Delta V_{o\%})(1 + \Delta I_{L\%})(1 - 2D)} \tag{4.42}$$

The switch utilization in Region 2 was solved and found to be:

$$U_2 = \frac{4}{(1 + \Delta V_{o\%})(1 + \Delta I_{L\%})(2D - 1)} \tag{4.43}$$

Therefore, the switch utilization is better when the converter is operating in Region 1 than in Region 2. In this region the duty cycle can be 50% or lower. Which is also the optimum point for impedance spectroscopy since the ripple is at its lowest.

4.6 Efficiency analysis

The converter's efficiency was analysed in both Regions 1 and 2 to determine which of the two, has a higher efficiency. The losses in the switches, capacitors, inductors and diodes were derived to calculate the efficiency.

4.6.1 Switching losses

When the switch turns on, there are losses due to the voltage decreasing and the current increasing. These losses can be calculated as:

$$P_{Ln} = \frac{1}{4} V_{in} I_o f (t_{vf} + t_{cr}) \tag{4.44}$$

Where, t_{vf} and t_{cr} are the voltage rise time and the current fall time, respectively. When the switch turns off the losses are:

$$P_{Lf} = \frac{P_o f_{sw}}{4D} (t_{vr} + t_{cf}) \tag{4.45}$$

Where, t_{vr} and t_{cf} are the voltage rise time and the current fall time, respectively. In Region 1, both states have a switch voltage V_{in} that is half the output voltage. In Region 2, the switch voltage is equal to the output voltage. Hence, the losses in Region 2 will be twice those in Region 1.

i. Switch Conduction losses

While the switch is operating, the losses are:

$$P_{cn} = \left(1 - \frac{V_{in}}{V_o}\right)\left(\frac{V_{in}}{V_o}\right)^2 I_o^2 r_{ds} \tag{4.46}$$

Where, r_{ds} is the drain to source resistance; V_{on} is the switch's on-state voltage. The conduction losses in Region 2 will also be twice those in Region 1 because of the direct relationship between the voltage and power loss.

ii. Diode losses

The converter has two diodes and the losses across the diode are:

$$P_D = 2(I_L V_{th} I_{D(ave)}^2 r_D)D \tag{4.47}$$

Where, $I_{D(ave)}$ is the average diode current between the states. The diode losses will be the same in both regions.

iii. ***Capacitor losses***

Each of the two load capacitors:

$$P_L = I_{c(rms)}^2 r_c \tag{4.48}$$

Where $I_{c(rms)}$ is the RMS current of the capacitors; r_c the capacitor's dc resistance. The capacitor losses will also be the same in both regions.

iv. ***Inductor losses***

For both the input and output inductors, the losses are given by:

$$P_L = I_L^2 r_L \tag{4.49}$$

Where, r_L is the inductor ESR resistance. The inductor losses in Region 1 will be less than those in Region 2 because, in Region 1, when switch S_1 is on, the converter draws only ac current from the battery and only draws dc current when switch S_2 is on. Whereas, in Region 2, the converter draws dc current in both states. This shows that the efficiency in Region 1 will be higher than the efficiency in Region 2, because of the lower losses in this Region making it the optimum region to operate in.

4.7 Three-level boost converter modelling

The three-level converter is a non-linear, 3rd order system. The converter can be linearized using state space averaging to obtain an approximate linear model for the converter.

4.7.1 State modelling

The model of state, input and output vectors to represent the dynamics of the converter.

$$\dot{x} = Ax + Bu \tag{4.50}$$

For the state equation, and:

$$y = Cx + Du \tag{4.51}$$

For the output equation. Where; A, B, C, D are matrices that describe the dynamic behaviour of the converter; x is state vector; u is the input vector; and y is the output vector. The state vector $\dot{x}$ has the same dimensions as the order of the converter – which is 3rd for the three-level converter. The order of a converter is determined by dynamics elements such as the inductor and capacitor. The state vector can therefore be represented as:

$$\dot{x} = \begin{bmatrix} \frac{dI_L(t)}{dt} \\ \frac{dV_{c1}(t)}{dt} \\ \frac{dV_{c2}(t)}{dt} \end{bmatrix} \tag{4.52}$$

Both regions were analysed, and their average models obtained. In Region 1, only Modes 2 and 3 apply. The state vector for each region can be represented as:

$$\dot{x} = A_1 x + B_1 u \tag{4.53}$$

For Mode 2 and:

$$\dot{x} = A_2 x + B_2 u \tag{4.54}$$

For Mode 3. The state matrices then become the sum of each Mode's state matrix. The dynamics equation representing Mode 2:

$$V_{in}(t) - I_L(t)r_L - L\frac{dI_L(t)}{dt} - V_{c2}(t) = 0 \tag{4.55}$$

For the voltage and:

$$r_{c2}C_2\frac{dV_{c2}(t)}{dt} = I_L(t) - \frac{V_{c2}(t)}{R} \tag{4.56}$$

For the current. Converting the equations into matrix form:

$$\begin{bmatrix} \frac{dI_L(t)}{dt} \\ \frac{dV_{c1}(t)}{dt} \\ \frac{dV_{c2}(t)}{dt} \end{bmatrix} = \begin{bmatrix} -\frac{r_L}{L} & 0 & -\frac{1}{L} \\ 0 & 0 & 0 \\ \frac{1}{r_{c2}C_2} & 0 & \frac{1}{r_{c2}RC_2} \end{bmatrix} \begin{bmatrix} I_L(t) \\ V_{c1}(t) \\ V_{c2}(t) \end{bmatrix} + \begin{bmatrix} \frac{1}{L} \\ 0 \\ 0 \end{bmatrix} V_{in}(t) \tag{4.57}$$

The state matrices then become:

$$A_1 = \begin{bmatrix} -\frac{r_L}{L} & 0 & -\frac{1}{L} \\ 0 & 0 & 0 \\ \frac{1}{r_{c2}C_2} & 0 & \frac{1}{r_{c2}RC_2} \end{bmatrix};\ B_1 = \begin{bmatrix} \frac{1}{L} \\ 0 \\ 0 \end{bmatrix} \tag{4.58}$$

In Mode 3:

$$V_{in}(t) - I_L(t)r_L - L\frac{dI_L(t)}{dt} - V_{c1}(t) = 0 \tag{4.59}$$

For the voltage and:

$$r_{c1}C_1\frac{dV_{c1}(t)}{dt} = I_L(t) - \frac{V_{c1}(t)}{R} \tag{4.60}$$

For the current. Converting the equations into matrix form:

$$\begin{bmatrix} \frac{dI_L(t)}{dt} \\ \frac{dV_{c1}(t)}{dt} \\ \frac{dV_{c2}(t)}{dt} \end{bmatrix} = \begin{bmatrix} -\frac{r_L}{L} & -\frac{1}{L} & 0 \\ \frac{1}{r_{c1}C_1} & \frac{1}{r_{c1}RC_1} & 0 \\ 0 & 0 & 0 \end{bmatrix} \begin{bmatrix} I_L(t) \\ V_{c1}(t) \\ V_{c2}(t) \end{bmatrix} + \begin{bmatrix} \frac{1}{L} \\ 0 \\ 0 \end{bmatrix} V_{in}(t) \tag{4.61}$$

The state matrices then become:

$$A_2 = \begin{bmatrix} -\frac{r_L}{L} & -\frac{1}{L} & 0 \\ \frac{1}{r_{c1}C_1} & \frac{1}{r_{c1}RC_1} & 0 \\ 0 & 0 & 0 \end{bmatrix};\ B_2 = \begin{bmatrix} \frac{1}{L} \\ 0 \\ 0 \end{bmatrix} \tag{4.62}$$

Using equations (4.58) and (4.62) the state matrix for this region is given by:

$$A = \begin{bmatrix} -\frac{r_L}{L} & 0 & -\frac{1}{L} \\ 0 & 0 & 0 \\ \frac{1}{r_{c2}C_2} & 0 & \frac{1}{r_{c2}RC_2} \end{bmatrix} + \begin{bmatrix} -\frac{r_L}{L} & -\frac{1}{L} & 0 \\ \frac{1}{r_{c1}C_1} & \frac{1}{r_{c1}RC_1} & 0 \\ 0 & 0 & 0 \end{bmatrix} = \begin{bmatrix} -\frac{2r_L}{L} & -\frac{1}{L} & -\frac{1}{L} \\ \frac{1}{r_{c1}C_1} & \frac{1}{r_{c1}RC_1} & 0 \\ \frac{1}{r_{c2}C_2} & 0 & \frac{1}{r_{c2}RC_2} \end{bmatrix} \tag{4.63}$$

And the input matrix becomes:

$$B = \begin{bmatrix} \frac{1}{L} \\ 0 \\ 0 \end{bmatrix} + \begin{bmatrix} \frac{1}{L} \\ 0 \\ 0 \end{bmatrix} = \begin{bmatrix} \frac{2}{L} \\ 0 \\ 0 \end{bmatrix} \tag{4.64}$$

The complete state model for the converter in Region 1 then becomes:

$$\begin{bmatrix} \frac{dI_L(t)}{dt} \\ \frac{dV_{c1}(t)}{dt} \\ \frac{dV_{c2}(t)}{dt} \end{bmatrix} = \begin{bmatrix} -\frac{2r_L}{L} & -\frac{1}{L} & -\frac{1}{L} \\ \frac{1}{r_{c1}C_1} & \frac{1}{r_{c1}RC_1} & 0 \\ \frac{1}{r_{c2}C_2} & 0 & \frac{1}{r_{c2}RC_2} \end{bmatrix} \begin{bmatrix} I_L(t) \\ V_{c1}(t) \\ V_{c2}(t) \end{bmatrix} + \begin{bmatrix} \frac{2}{L} \\ 0 \\ 0 \end{bmatrix} V_{in}(t) \tag{4.65}$$

In Region 2, Modes 1 and 4 apply. In Mode 1, when both switches are on, the dynamic equation describing the voltage in the on state:

$$V_{in}(t) - I_L(t)r_L - L\frac{dI_L(t)}{dt} = 0 \tag{4.66}$$

And for the current, the state:

$$r_{c1}C_1\frac{dV_{c1}(t)}{dt} = r_{c2}C_2\frac{dV_{c1}(t)}{dt} = -\frac{V_{c1}(t)+V_{c2}(t)}{R} \tag{4.67}$$

Converting the equation into matrix form:

$$\begin{bmatrix}\frac{dI_L(t)}{dt}\\ \frac{dV_{c1}(t)}{dt}\\ \frac{dV_{c2}(t)}{dt}\end{bmatrix} = \begin{bmatrix}-\frac{r_L}{L} & 0 & 0\\ 0 & -\frac{1}{r_{c1}RC_1} & -\frac{1}{r_{c1}RC_1}\\ 0 & -\frac{1}{r_{c2}RC_2} & -\frac{1}{r_{c2}RC_2}\end{bmatrix}\begin{bmatrix}I_L(t)\\ V_{c1}(t)\\ V_{c2}(t)\end{bmatrix} + \begin{bmatrix}\frac{1}{L}\\ 0\\ 0\end{bmatrix}V_{in}(t) \tag{4.68}$$

In Mode 4, when both switches are both off, the dynamic equation are:

$$V_{in}(t) - I_L(t)r_L - L\frac{dI_L(t)}{dt} - V_{c1}(t) - V_{c2}(t) = 0 \tag{4.69}$$

For the voltage and:

$$r_{c1}C_1\frac{dV_{c1}(t)}{dt} = r_{c2}C_2\frac{dV_{c1}(t)}{dt} = I_L(t) - \frac{V_{c1}(t)+V_{c2}(t)}{R} \tag{4.70}$$

For the current. Converting the equations into matrix form:

$$\begin{bmatrix}\frac{dI_L(t)}{dt}\\ \frac{dV_{c1}(t)}{dt}\\ \frac{dV_{c2}(t)}{dt}\end{bmatrix} = \begin{bmatrix}-\frac{r_L}{L} & -\frac{1}{L} & -\frac{1}{L}\\ \frac{1}{r_{c1}RC_1} & -\frac{1}{r_{c1}RC_1} & -\frac{1}{r_{c1}RC_1}\\ \frac{1}{r_{c2}RC_2} & -\frac{1}{r_{c2}RC_2} & -\frac{1}{r_{c2}RC_2}\end{bmatrix}\begin{bmatrix}I_L(t)\\ V_{c1}(t)\\ V_{c2}(t)\end{bmatrix} + \begin{bmatrix}\frac{1}{L}\\ 0\\ 0\end{bmatrix}V_{in}(t) \tag{4.71}$$

The region state matrix then becomes:

$$A = D\begin{bmatrix}-\frac{r_L}{L} & 0 & 0\\ 0 & -\frac{1}{r_{c1}RC_1} & -\frac{1}{r_{c1}RC_1}\\ 0 & -\frac{1}{r_{c2}RC_2} & -\frac{1}{r_{c2}RC_2}\end{bmatrix} + (1-D)\begin{bmatrix}-\frac{r_L}{L} & \frac{1}{L} & \frac{1}{L}\\ \frac{1}{r_{c1}RC_1} & -\frac{1}{r_{c1}RC_1} & -\frac{1}{r_{c1}RC_1}\\ \frac{1}{r_{c2}RC_2} & -\frac{1}{r_{c2}RC_2} & -\frac{1}{r_{c2}RC_2}\end{bmatrix} = \begin{bmatrix}-\frac{r_L}{L} & -\frac{1-D}{L} & -\frac{1-D}{L}\\ \frac{1-D}{r_{c1}C_1} & -\frac{1}{r_{c1}RC_1} & -\frac{1}{r_{c1}RC_1}\\ \frac{1-D}{r_{c2}C_2} & -\frac{1}{r_{c2}RC_2} & -\frac{1}{r_{c2}RC_2}\end{bmatrix} \tag{4.72}$$

And the region input matrix:

$$B = D\begin{bmatrix}\frac{1}{L}\\ 0\\ 0\end{bmatrix} + (1-D)\begin{bmatrix}\frac{1}{L}\\ 0\\ 0\end{bmatrix} = \begin{bmatrix}\frac{1}{L}\\ 0\\ 0\end{bmatrix} \tag{4.73}$$

The complete model for the region becomes:

$$\begin{bmatrix} \frac{dI_L(t)}{dt} \\ \frac{dV_{c1}(t)}{dt} \\ \frac{dV_{c2}(t)}{dt} \end{bmatrix} = \begin{bmatrix} -\frac{r_L}{L} & -\frac{1-D}{L} & -\frac{1-D}{L} \\ \frac{1-D}{r_{c1}C_1} & -\frac{1}{r_{c1}RC_1} & -\frac{1}{r_{c1}RC_1} \\ \frac{1-D}{r_{c2}C_2} & -\frac{1}{r_{c2}RC_2} & -\frac{1}{r_{c2}RC_2} \end{bmatrix} \begin{bmatrix} I_L(t) \\ V_{c1}(t) \\ V_{c2}(t) \end{bmatrix} + \begin{bmatrix} \frac{1}{L} \\ 0 \\ 0 \end{bmatrix} V_{in}(t) \tag{4.74}$$

4.7.2 Small signal analysis

Small signal analysis assumes that the input is small enough such that the system can be treated as linear. This enables the derivation of small signal transfer functions that describe the converter from the input to various outputs which are linear, continuous and time-invariant. The small signal equations describing the converter are:

$$\left.\begin{aligned} V_{in}(t) &= V_{in} + \widetilde{v_{in}}(t) \\ x &= X + \tilde{x} \\ V_o(t) &= V_o + \widetilde{v_o}(t) \\ I_L(t) &= I_L + \widetilde{i_L}(t) \\ u_1(t) &= D_1 + \widetilde{d_1}(t) \\ u_1(t) &= D_1 + \widetilde{d_1}(t) \end{aligned}\right\} \tag{4.75}$$

To obtain the linear model, second order terms are assumed to be small enough to be neglected. The variations in the input are also assumed to be negligible. The plant equation can be obtained from:

$$P_o = C(SI - A)^{-1}B \tag{4.76}$$

$$X = V_{in}CA^{-1} \tag{4.77}$$

Where:

$$C = \begin{bmatrix} 1 & 0 & 0 \\ 0 & 1 & 0 \\ 0 & 0 & 1 \end{bmatrix} \tag{4.78}$$

Solving for the small signal transfer functions yields:

$$\frac{\widetilde{\imath_L}(s)}{\widetilde{v_{in}}(s)} = \frac{sC_1 + \frac{1}{R}}{LC_1\left(s^2 + \frac{s}{RC_1 +} \frac{\left(1 - D_1 - \frac{D_2}{2}\right)^2}{LC_1}\right)} \tag{4.79}$$

$$\frac{\widetilde{\imath_L}(s)}{\widetilde{d_1}(s)} = \frac{V_o\left(sC_1 + \frac{1}{R}\right) + \left(1 - D_1 - \frac{D_2}{2}\right)I_L}{LC_1\left(s^2 + \frac{s}{RC_1 +} \frac{\left(1 - D_1 - \frac{D_2}{2}\right)^2}{LC_1}\right)} \tag{4.80}$$

$$\frac{\widetilde{\imath_L}(s)}{\widetilde{d_2}(s)} = \frac{\frac{V_o}{2}\left(sC_1 + \frac{1}{R}\right) + \left(1 - D_1 - \frac{D_2}{2}\right)\frac{I_L}{2}}{LC_1\left(s^2 + \frac{s}{RC_1 +} \frac{\left(1 - D_1 - \frac{D_2}{2}\right)^2}{LC_1}\right)} \tag{4.81}$$

$$\frac{\widetilde{v_{c_2}}(s) + \widetilde{v_{c_1}}(s)}{\widetilde{v_{in}}} = \frac{sC_1\left(1 - D_1 - \frac{D_2}{2}\right)}{LC_1\left(s^2 + \frac{s}{RC_1 +} \frac{\left(1 - D_1 - \frac{D_2}{2}\right)^2}{LC_1}\right)} \tag{4.82}$$

$$\frac{\widetilde{v_{c_1}}(s)}{\widetilde{v_{in}}(s)} = \frac{\left(1 - D_1 - \frac{D_2}{2}\right)}{LC_1\left(s^2 + \frac{s}{RC_1 +} \frac{\left(1 - D_1 - \frac{D_2}{2}\right)^2}{LC_1}\right)} \tag{4.83}$$

$$\frac{\widetilde{v_{c_1}}(s)}{\widetilde{d_1}(s)} = \frac{V_o\left(1 - D_1 - \frac{D_2}{2}\right) - sLI_L}{LC_1\left(s^2 + \frac{s}{RC_1 +} \frac{\left(1 - D_1 - \frac{D_2}{2}\right)^2}{LC_1}\right)} \tag{4.84}$$

$$\frac{\widetilde{v_{c_1}}(s)}{\widetilde{d_2}(s)} = \frac{\frac{V_o}{2}\left(1 - D_1 - \frac{D_2}{2}\right) - \frac{sLI_L}{2}}{LC_1\left(s^2 + \frac{s}{RC_1 +} \frac{\left(1 - D_1 - \frac{D_2}{2}\right)^2}{LC_1}\right)} \tag{4.85}$$

$$\frac{\widetilde{v_{c_1}}(s)}{\widetilde{v_{c_2}}(s)} = \frac{\left(1 - D_1 - \frac{D_2}{2}\right)^2}{LC_1\left(s^2 + \frac{s}{RC_1 +}\frac{\left(1 - D_1 - \frac{D_2}{2}\right)^2}{LC_1}\right)} \tag{4.86}$$

The small signal transfer functions described by equations (4.79) - (4.86) characterize the three-level boost converter from various inputs to its outputs – this ensures multiple control techniques that can be used to control the three level boost converter.

4.7.3 Three-level boost converter control scheme

Controlling the **3**-level converter involves regulating the output voltage and ensuring that the voltages across capacitor $\boldsymbol{C_1}$ and $\boldsymbol{C_2}$ are equally balanced; Figure 4.6 shows the configuration required for this control. The regulation loop is designed such that the inductor current produces the duty cycle control signal d_1. The balancing loop is designed such that it produces the duty cycle control signal d_2. The EIS duty cycle, $\widetilde{d_{eis}}$ signal is added on the modulating dc duty cycle. The EIS signal is only added to the modulating signal once the system reaches steady state. To ensure that the system is operating in a linear region, a threshold was set for the output voltage. The threshold was set such that the EIS induced ripple at the input voltage is not more than $10mV$ peak per Lithium-ion cell i.e. $60mV$ for 6 series connected cells; and the average terminal battery voltage is $\pm 5\%$ of $22V$. If the output voltage falls outside the threshold, the EIS measurement terminates.

Converter systems have several time delays generated by the components of the system; because of these time delays the voltage across the filter capacitors C_1 and C_2, becomes unbalanced. This unbalance:

- Lowers the output voltage value
- Increases the voltage across the capacitor C_1 to high levels
- Increases the voltage stress across the switches
- Alters the control transfer functions

As such, the voltage across the capacitors must be balanced to ensure normal system operation. A control loop to balance the capacitor is added to the classical feedback loop. Figure 4.6 shows the configuration of the control scheme that was employed.

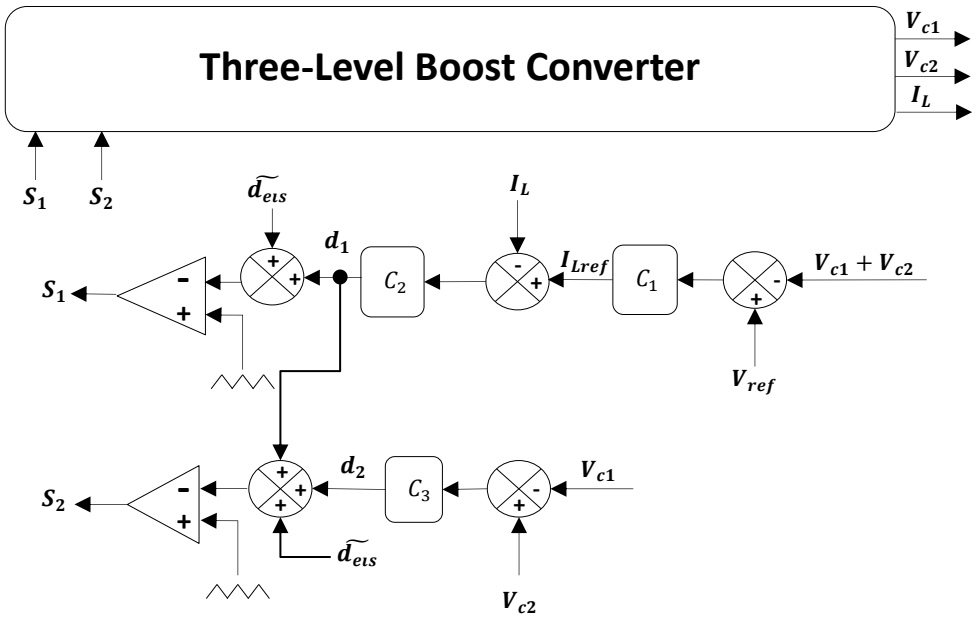

Figure 4.6: Three-level boost converter control scheme

Under normal operation the duty cycle d_2 is zero since the voltage across the capacitors are equal. When the there is a difference in the capacitor voltages, the duty cycle d_2 adjusts to ensure the voltages balance. The compensator C_1 is the transfer function from the output voltage to the inductor current as described by equation (4.82). The compensator C_2 is the transfer function from the duty cycle to the inductor current as described by equation (4.80) and the compensator C_3 is the transfer function across the two filter capacitors as described by (4.86).

5. Design of the Three-level Boost Converter for EIS Implementation

The design of the system was undertaken in this section. First the specifications for the converter were stated. The converter passive components were then designed according to the specifications. The switch was selected based on the voltage stress and then the controllers for the control scheme were designed.

5.1 System specifications

The converter DC specifications and the EIS AC specifications used in this research are discussed in sections *5.1.1* and *5.1.2* below.

5.1.1 Converter specifications

The converter was powered from a Lithium-ion battery stack and was designed such that it has low current and voltage ripples for optimum EIS results. Table 5-1 shows the specifications for the converter DC operation.

Table 5-1: Three-level boost converter specifications

Battery stack power output	$440\ W$
Battery / DC output voltage	$22 - 25\ V_{in}$
Rated current	$20A$
DC output voltage	$44\ V_{DC}$
Carrier switching frequency	$20kH_z$
DC battery internal resistance R_{Lb}	$18m\Omega$
DC Load impedance R_L	22Ω
Inductor ESR r_L	$70m\Omega$
Capacitor ESR r_C	$10m\Omega$
Output voltage ripple	$\leq 2\%\ of\ V_o(t)$
Inductor ripple ΔI_L	$20\%\ of\ I_{L,max}$
Duty cycle, D	50%

The battery stack has a maximum discharge current of $20A$ – while the nominal operation was designed such that the battery has a constant $4A$ DC discharge current, while charging a laptop battery. The laptop battery is rated at $90W, 2.17A$.

5.1.2 EIS specifications

The EIS current amplitude was chosen such that the battery would remain in its linear region of operation. However, if an arbitrary EIS current amplitude is injected, it might operate in the non-linear region thereby leading to invalid results. The impedance spectroscopy was designed according to the specifications in Table 5-2.

Table 5-2: Three-level boost converter EIS specifications

Signal type	$Sine\ wave$
EIS Current Amplitude	$10\%\ I_{Load}$
EIS Frequency range	$0.1 - 2000\ H_z$
EIS Testing Temperature	25^oC
States of Charge	$25\%, 50\%, 100\%$

The EIS is specified to be conducted at a room temperature of $25°C$ to remain constant during the operation of EIS when operating at 100%, 50% and 25% state of charge of the battery over a frequency range of $0.1H - 2kHz$. The amplitude of 10% of the battery current is specified in order to maintain the stability and the linearity of the system of operation.

5.2 Selection of passive components design

The inductor, the filter capacitors and the decoupling capacitors were designed for according to the specifications.

5.2.1 Inductor design

The inductor size was determined using equation (5.1):

$$\Delta I_L = \frac{V_o D(1-D)}{L f_{sw}} \tag{5.1}$$

The ripple inductor current, ΔI_L was specified to be 20% of the maximum inductor current ripple. The maximum inductor current ripple was chosen to be 9A. To determine the maximum inductor current ripple, equation (5.2) was considered.

$$I_L = \frac{I_{L,max} - I_{L,min}}{2} \tag{5.2}$$

Where, $(I_{L,max} - I_{L,min})$ is equivalent to the peak to peak ripple inductor current ΔI_L, as such:

$$I_{L,} = \frac{\Delta I_L \times I_{Lmax}}{2} \tag{5.3}$$

But ΔI_L is 20% of the maximum inductor current, hence:

$$I_L = \frac{0.2 \times 9}{2} \tag{5.4}$$

Solving the maximum inductor current:

$$I_{L,} = \frac{1.8}{2} \tag{5.5}$$

Substituting (5.5) into (5.1):

$$L = \frac{V_o \times (1 - D)(2D - 1)}{f_{sw} I_L} \tag{5.6}$$

Using Table 5-1 and substituting the values, the inductor value was computed to be $160\mu H$. The experimental inductor was built using a Ferrite core and the value obtained at 20kH_z was $171\mu H$. This value was close enough to the calculated value such that it would not cause a significant change in the expected results. The ESR resistance of the inductor built was $98m\Omega$. This is larger than the specification value but will not cause a large change in the gain magnitude of the converter.

5.2.2 Filter capacitor design

The filter capacitors ensure that the output voltage is constant as the converter switches between states. The capacitor was computed from:

$$C_1 = C_2 = \frac{DT_s\left(V_{in} - \frac{V_o}{2}\right)}{R\Delta V_c} \tag{5.7}$$

Substituting the values from Table 5-1, the filter capacitors were computed to be $210\mu F$ each. Each of the capacitors required a voltage rating of $22V$, based on the specifications. The capacitors used experimentally were $250\mu F$ with a voltage rating of $55V$.

5.2.3 Decoupling capacitor design

The output voltage of the battery stack is not well regulated because of the high switching converter. This unregulated output voltage leads to higher inductor current peaks and high voltage ripple at the output. To solve this issue, a decoupling capacitor was added at the input of the converter to ensure a constant input voltage. This capacitor value was computed from:

$$C_d = \frac{V_{in}I_L}{2\pi f V_{in}\Delta V_c} \tag{5.8}$$

Substituting the values from Table 5-1, the capacitor value obtained was $1.3mF$. This value was enough to minimize the ripple at the input.

5.3 Switch selection

The switch was selected such that it can operated at 20kHz and can handle voltage and current stresses as specified by equations (4.27)-(4.30) and (4.34)-(4.36). Using Table 5-1, the voltage stress during Region 1 was computed to be $40V$ and the current stress was $11A$. Since the converter will also operate in Region 2, because of the EIS duty cycle, the voltage and current stress in that region were computed to be $57V$ and $14A$, respectively. The switch selected was a SCT2120AF MOSFET, whose data sheet can be found in the Appendix. The MOSFET can handle $650V$ and $29A$ at a drain power of $165W$ – which is more than adequate for this application.

5.4 EIS signal design

Before the battery model can be simulated, the FRA was used to parameterize the battery using the EEC in Fig. 2. The developed model was then represented in the MATLAB Simulink as an equivalent circuit. The battery equivalent circuit parameters were estimated at 100% SOC over a frequency

range $0.1Hz - 2kHz$. The battery current was set at $4A$ so that it won't change the battery SoC significantly during the period of measurement. The amplitude that is 10% of the battery current, was used as the perturbation amplitude, in order to maintain the stability and linearity of the system. The battery current can be estimated as:

$$I_{bat} = I_{dc} + I_{eis} + I_{sw} \tag{5.9}$$

Where:

$$I_{eis} = 0.1 I_{dc} sin(2\pi f_{eis} t) \tag{5.10}$$

And, I_{dc} is the DC discharging current; I_{eis} the EIS current; I_{sw} the switching frequency current; f_{eis} the frequency of EIS perturbation signal. The parameters of the Nyquist plot obtained from both the converter simulation and the FRA which was estimated using the transfer function of the AC-EEC model. The EIS signal is injected by adding a sinusoidally varying EIS duty cycle D_{eis}, of a small peak amplitude, on top of the 50% duty cycle operating point of the converter such that,

$$D(t) = D_{dc} + D_{eis} \tag{5.11}$$

Where:

$$D_{eis} = \left(\left(1 - \left(\frac{V_{0.ref}}{R_L} \left(\frac{1}{I_{dc} + I_{eis}} \right) \right) \right) - D_{dc} \right) sin(2\pi f_{eis} t) \tag{5.12}$$

The peak amplitude of D_{eis} was chosen such that, the lithium ion battery draws I_{eis}; this peak was approximated by using the converter current transfer ratio based on equation (4.10). Assuming a constant dc load current and battery current at the operating point, the battery current reaches a low frequency peak defined by the EIS current therefore, using (4.10), the D_{eis} was determined as shown in (5.12).

5.5 Controller design

The compensators for both the main and voltage balancing loops were designed in this section. Proportional integral (PI) controllers were chosen as the design of choice. There were 3 PI controllers that were designed – 2 in the main loop and 1 for the voltage balancing loop. Table 5-3 shows the specifications for the controllers which were based on the battery capabilities and EIS requirements.

Table 5-3: Controller specifications

Specification Type	Specification
Steady State Error	Zero
Percentage Overshoot	$\leq 17\%$
Bandwidth	$\geq 2000Hz$
Phase margin	$\geq 58^{o}$
Settling time	$50ms$

The overshoot was selected as such, because the maximum voltage the battery can handle for a short period of time is $4.2V$. This overshoot specification then gave rise to the phase margin. The settling time was a specification that acts as a threshold time for the EIS measurements. The bandwidth was selected because the battery was to be tested for EIS frequencies up to $2000Hz$.

5.5.1 Voltage reference controller design

The voltage reference controller ensures a regulated output voltage for the three-level boost converter. The plant relating to this controller is as defined by equation (4.82):

$$\frac{\widetilde{v_{c_2}}(s)+\widetilde{v_{c_1}}(s)}{\widetilde{v_{in}}}=\frac{sC_1\left(1-D_1-\frac{D_2}{2}\right)}{LC_1\left(s^2+\frac{s}{RC_1+}\frac{\left(1-D_1-\frac{D_2}{2}\right)^2}{LC_1}\right)}$$

The plant is a second order system. The controller was synthesized using MATLAB Sisotool and the response shown in Figure 5.1.

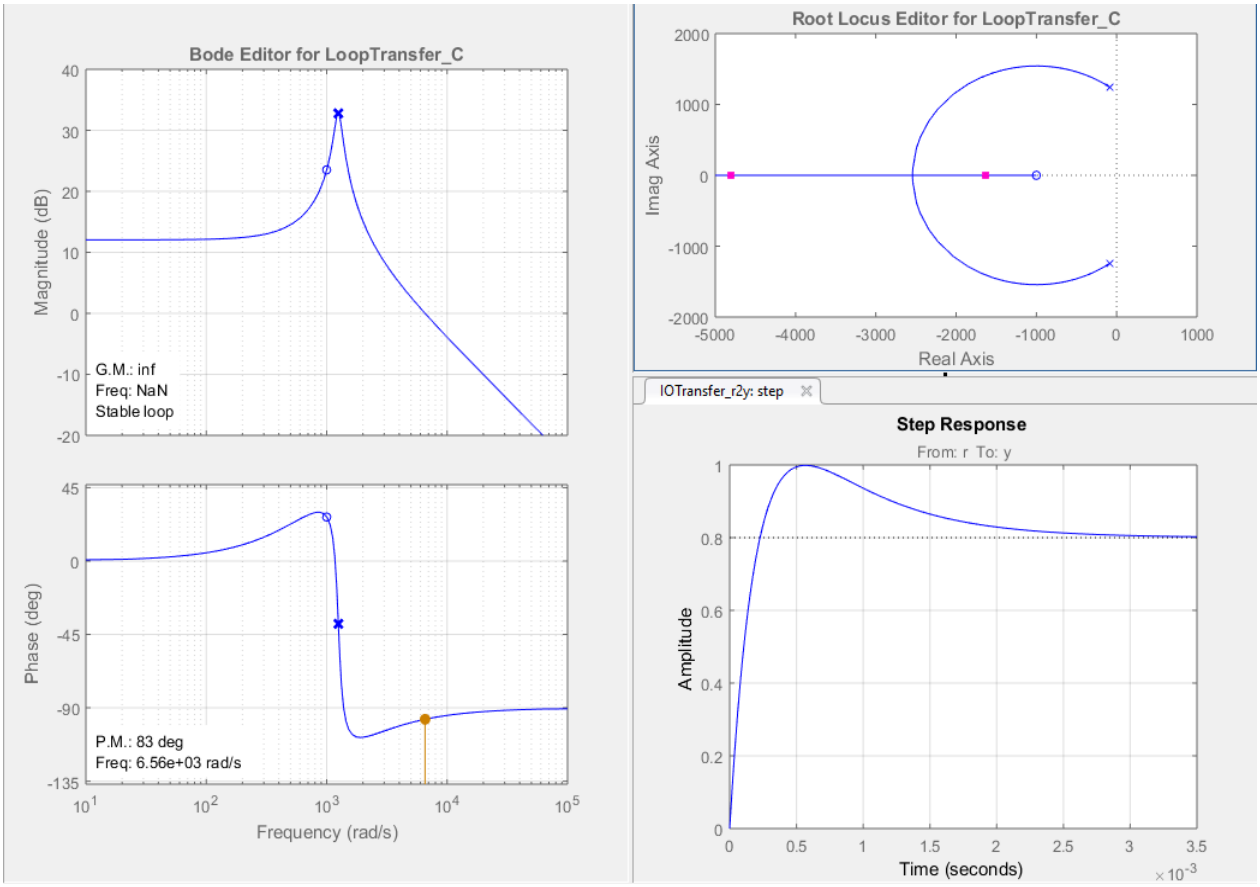

Figure 5.1: Voltage reference plant open loop response

The response of the plant shows that it is stable and minimum phase – it does not have a zero on the right hand-hand plane and hence, has no undershoot in the time response. The bode plot shows that resonance for the plant is between $1000rad.s^{-1}$ and $2000rad.s^{-1}$. The bandwidth for the plant is greater than $6000Hz$ which enables impedance testing. The root locus shows that the system has oscillatory dominant poles meaning that, if there is low gain in the controller, the system will oscillate. Large gain values would result in a critically damped system that would meet the specifications. The settling time of the response of the plant is $3.5ms$ which meets the requirements for settling time. The PI controller therefore, needs to be designed to meet the overshoot and steady state error specifications.
The PI controller has a structure as illustrated by equation (5.13)

$$C = K_p + \frac{K_i}{s} \tag{5.13}$$

Where, K_p is the proportional gain and K_i is the integral gain. Simplifying (5.13):

$$C = \frac{K_p\left(s + \frac{K_i}{K_p}\right)}{s} \tag{5.14}$$

Equation (5.14) shows that to design the PI controller, an integrator is added, then a zero is placed and finally the controller gain is designed. The integrator was added as shown in Figure 5.2. The integrator

ensure type number correction i.e. it increases the system type number from Zero to One. This means that for a step input – as provided by the converter voltage – the response will have zero steady state error.

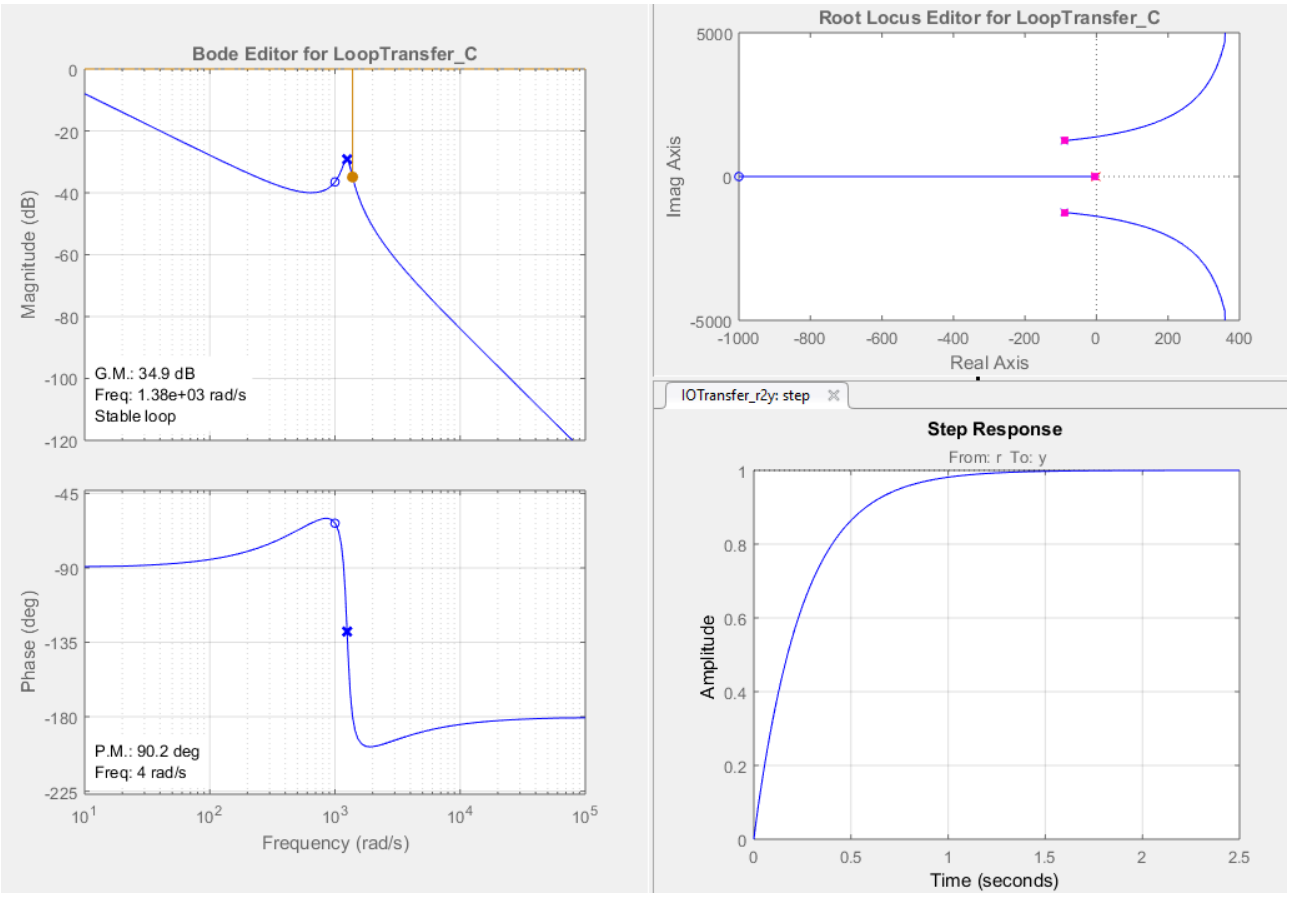

Figure 5.2: Voltage reference plant closed loop response with integrator

The closed loop response shows that the system is still stable. The bode plot however, shows that the system bandwidth has decreased from $6000Hz$ to less that $80Hz$ because of the integrator. Although the phase margin has improved, the system now shows a limited gain margin of $34.9dB$. This gain margin is still within the design specifications. With this limited gain margin, the root locus now shows that if the controller gain increases significantly, the system will not only become oscillatory. The step response now shows no overshoot or steady state error. The settling time however, has increased to $2s$ which is above the required specifications.

The zero was added such that it cancels out the effects of the slowest poles of the system, in this case, the oscillatory pair of open loop poles as shown in Figure 5.2.

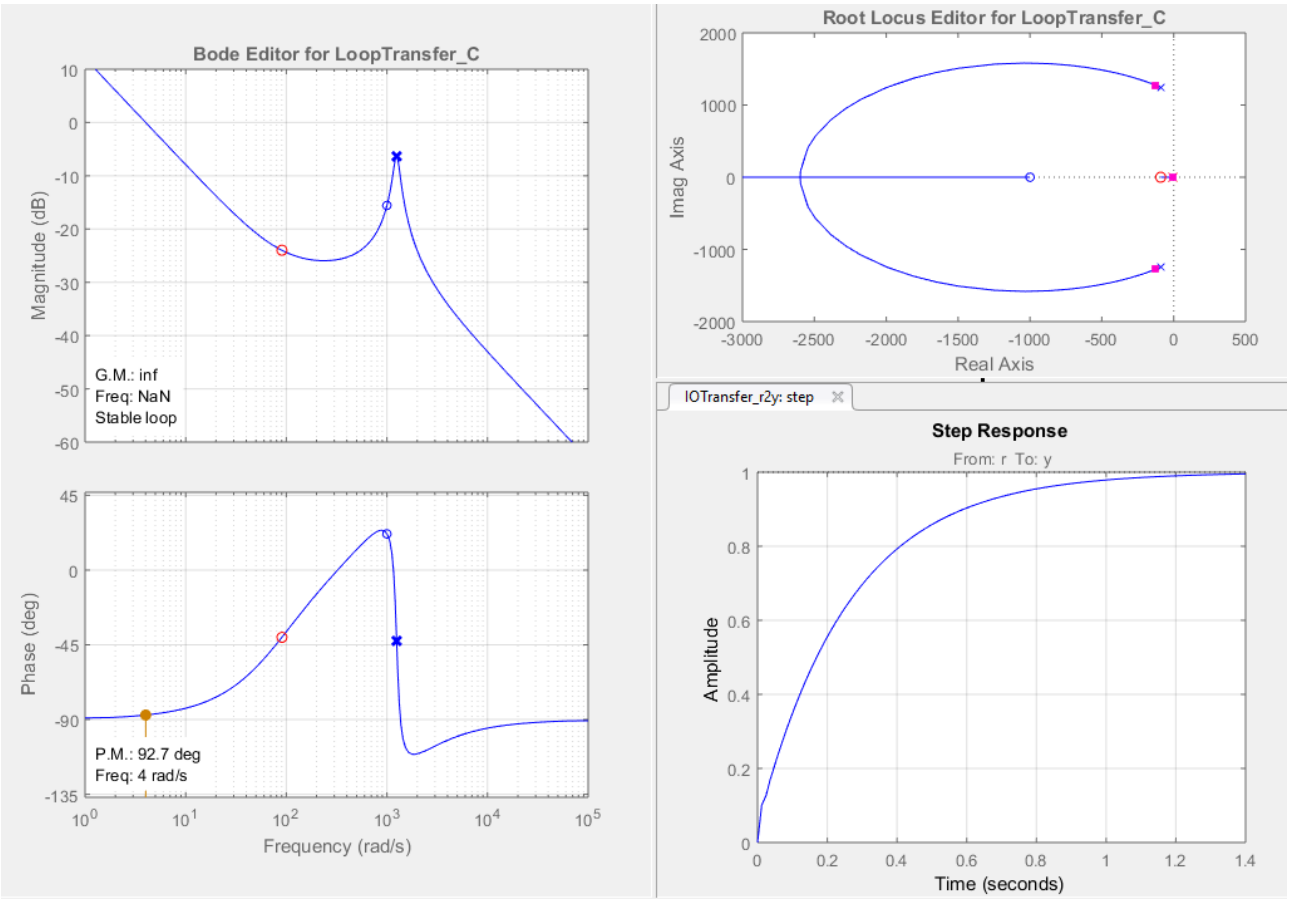

Figure 5.3: voltage reference plant closed loop response with integrator and zero

The system response is still stable. The bode plot bandwidth remains unchanged. The phase margin has improved to 92.7^{o} and the gain margin is now infinite. The root locus now shows that decreasing the gain will not result in an oscillatory or unstable system. In fact, increasing the gain will result in better damped system and will also increase the speed of the response.

The gain was tuned until an appropriate response was obtained as shown in Figure 5.4.

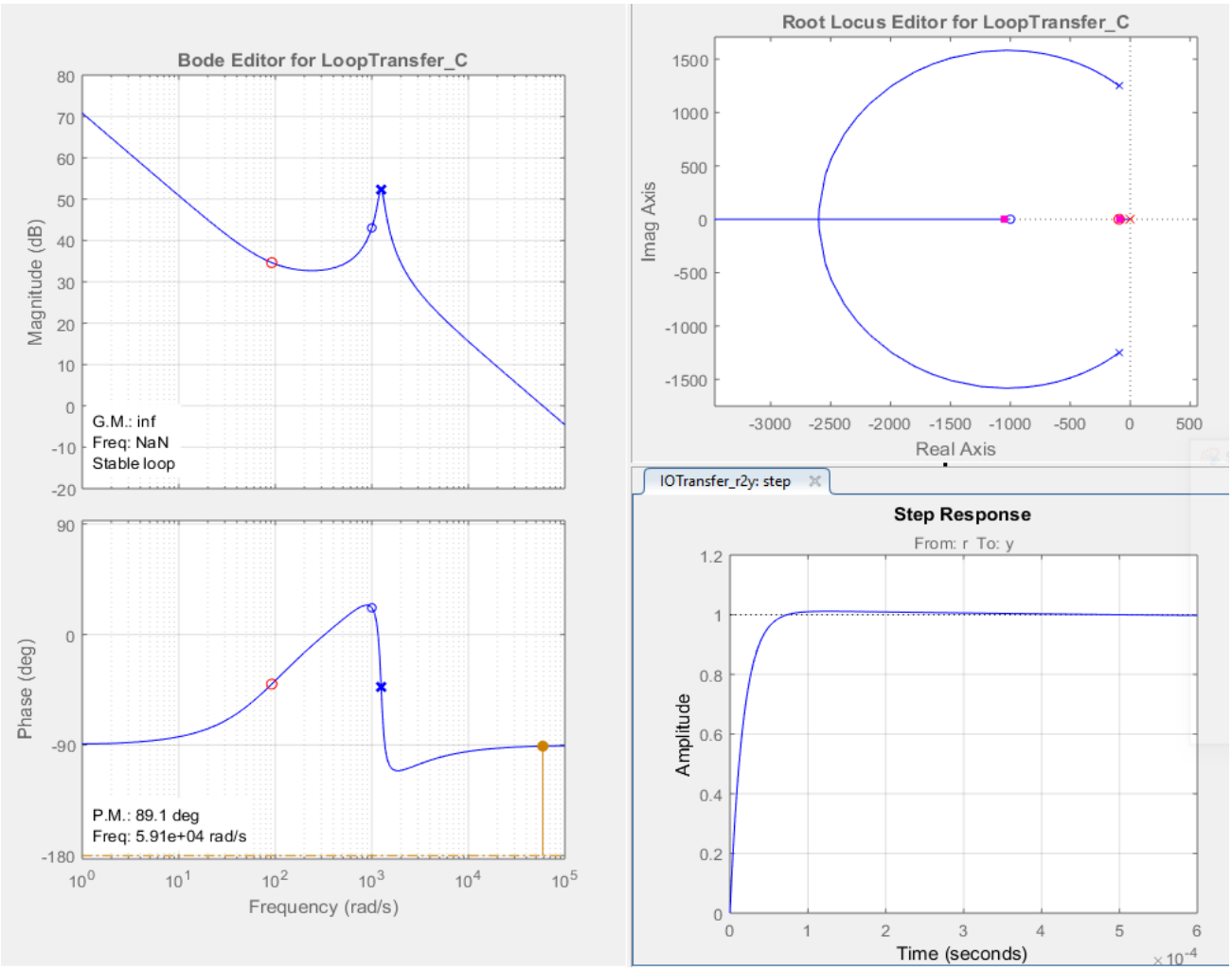

Figure 5.4: Voltage reference system closed loop response under PI compensation

The response now shows that the bandwidth of the system is greater than $10000Hz$ which meets the design specifications. The phase margin is 89.1^o which meets the specifications. The gain margin is infinite. The step response a response settling time of $600\mu s$ which is fast enough for EIS measurements. The overshoot observed is $< 1\%$ of the final value, which also meets the specifications. The PI controller chosen was therefore,

$$C_1 = \frac{78 \times 10^3 (s + 90.91)}{s} \tag{5.15}$$

The controller was then used to simulate the three-level boost converter's closed loop as will be shown in the results section.

5.5.2 Inductor current controller design

The inductor current plant is as defined by equation (4.80):

$$\frac{\widetilde{i_L}(s)}{\widetilde{v_{in}}(s)} = \frac{sC_1 + \frac{1}{R}}{LC_1\left(s^2 + \frac{s}{RC_1 + \frac{\left(1 - D_1 - \frac{D_2}{2}\right)^2}{LC_1}}\right)}$$

The plant was simulated on MATLAB Sisotool as show Figure 5.5 by to design the controller.

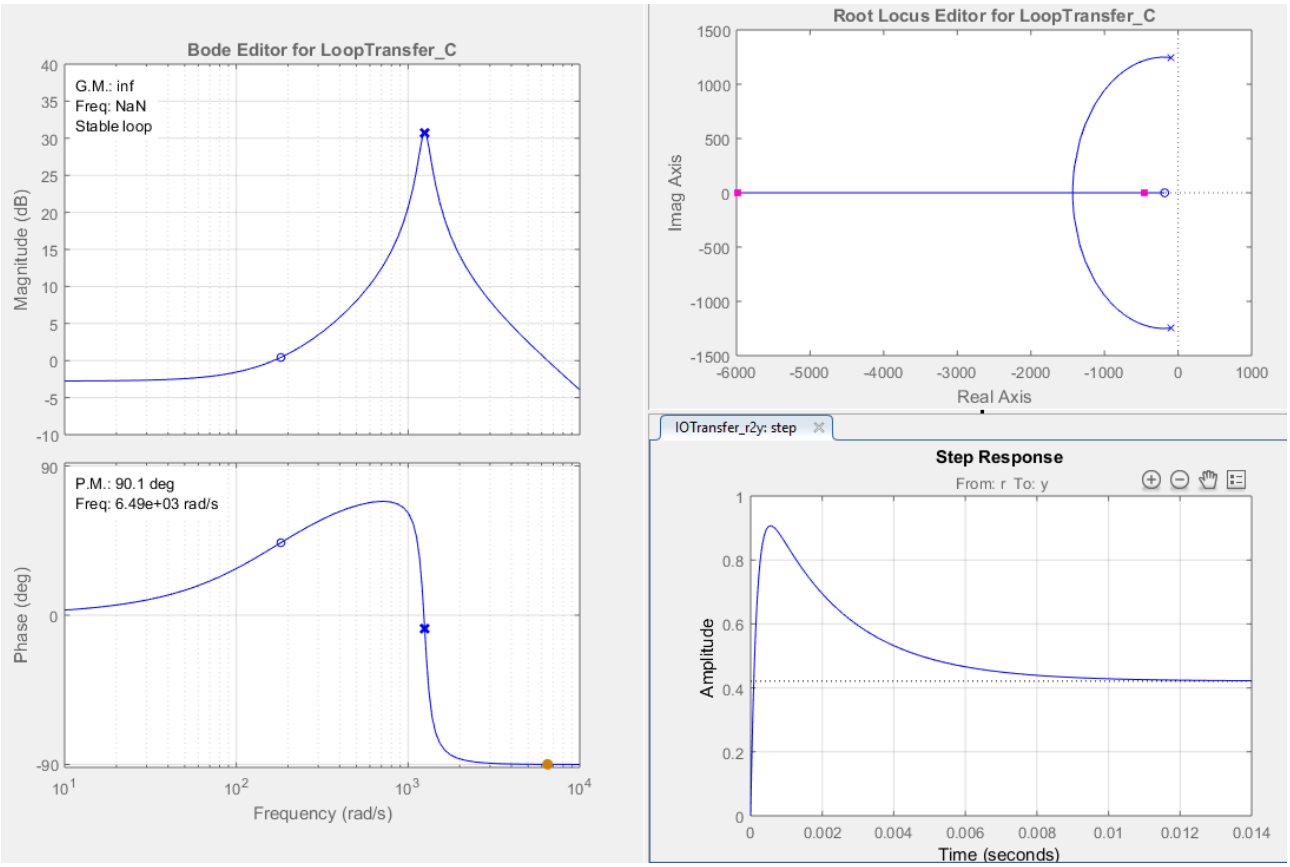

Figure 5.5: Inductor current loop open loop response

The response shows that the open loop is stable. The bode plot shows a bandwidth of more than $64000Hz$ which meets the specifications. Both the gain and phase margins also meet the specifications. Because the poles of the plant are the same as those of the voltage reference loop, the system shows the same resonance point. The root locus shows that small gain values will result in a stable but oscillatory response with larger gains improving the system damping and overshoot. The step response shows an overshoot of 114% from the final value, which does not meet the system specifications. The settling time is $14ms$ which is within the requirements, but the steady state error is 68% of the setpoint.

The PI controller was designed using the same technique as the voltage reference loop and was obtained to be:

$$C_2 = \frac{14.25 \times 10^2 (s + 214.32)}{s} \tag{5.16}$$

The response from this controller is shown in Figure 5.6.

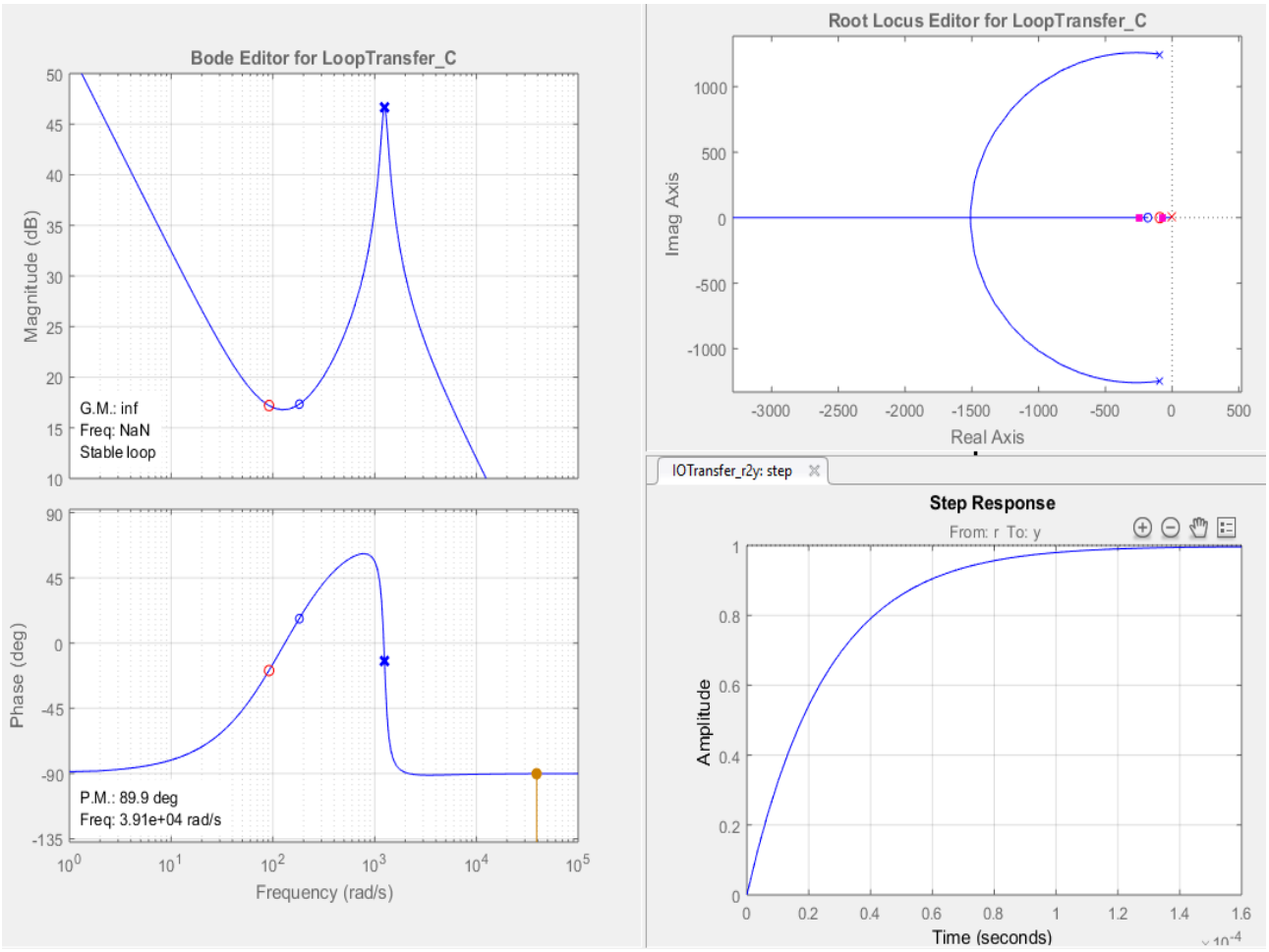

Figure 5.6: Inductor current loop closed loop response under PI compensation

The final response is shown to be stable and meets all the required specifications. The phase margin is 89.9^{o} and the gain margin is infinite. The step response shows that the system has not overshoot and steady state error. The settling time observed is $160\mu s$.

5.5.3 Voltage balancing loop controller design

The voltage balancing loop ensures a balanced voltage across the two filter capacitors. The plant for this is defined by equation (4.86) as:

$$\frac{\widetilde{v_{c_1}}(s)}{\widetilde{v_{c_2}}(s)} = \frac{\left(1 - D_1 - \frac{D_2}{2}\right)^2}{LC_1\left(s^2 + \frac{s}{RC_1 +}\frac{\left(1 - D_1 - \frac{D_2}{2}\right)^2}{LC_1}\right)}$$

The open loop response of the plant is shown by

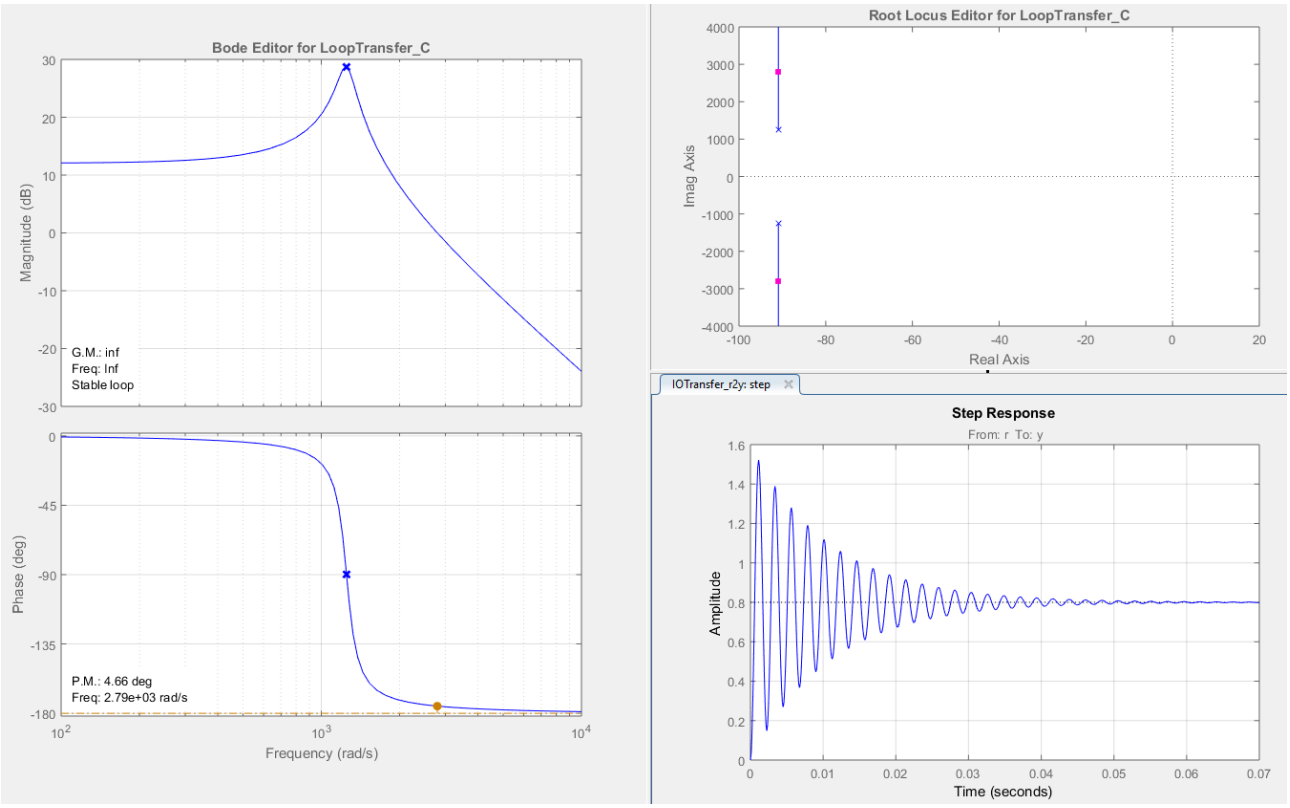

Figure 5.7: Voltage balancing loop open loop response

The root locus shows that the system has an oscillatory locus. The larger the gain values in the controller the more oscillatory the system would become. The step response shows large oscillations with an overshoot of 88% of the final value. The settling time of the system is $70ms$ which above the specifications. The steady state error observed is 20%.

The PI controller was design on MATLAB Sisotool and found to be:

$$C_3 = \frac{14.25 \times 10^2 (s + 214.32)}{s} \tag{5.17}$$

The response from the controller is shown in Figure 5.8.

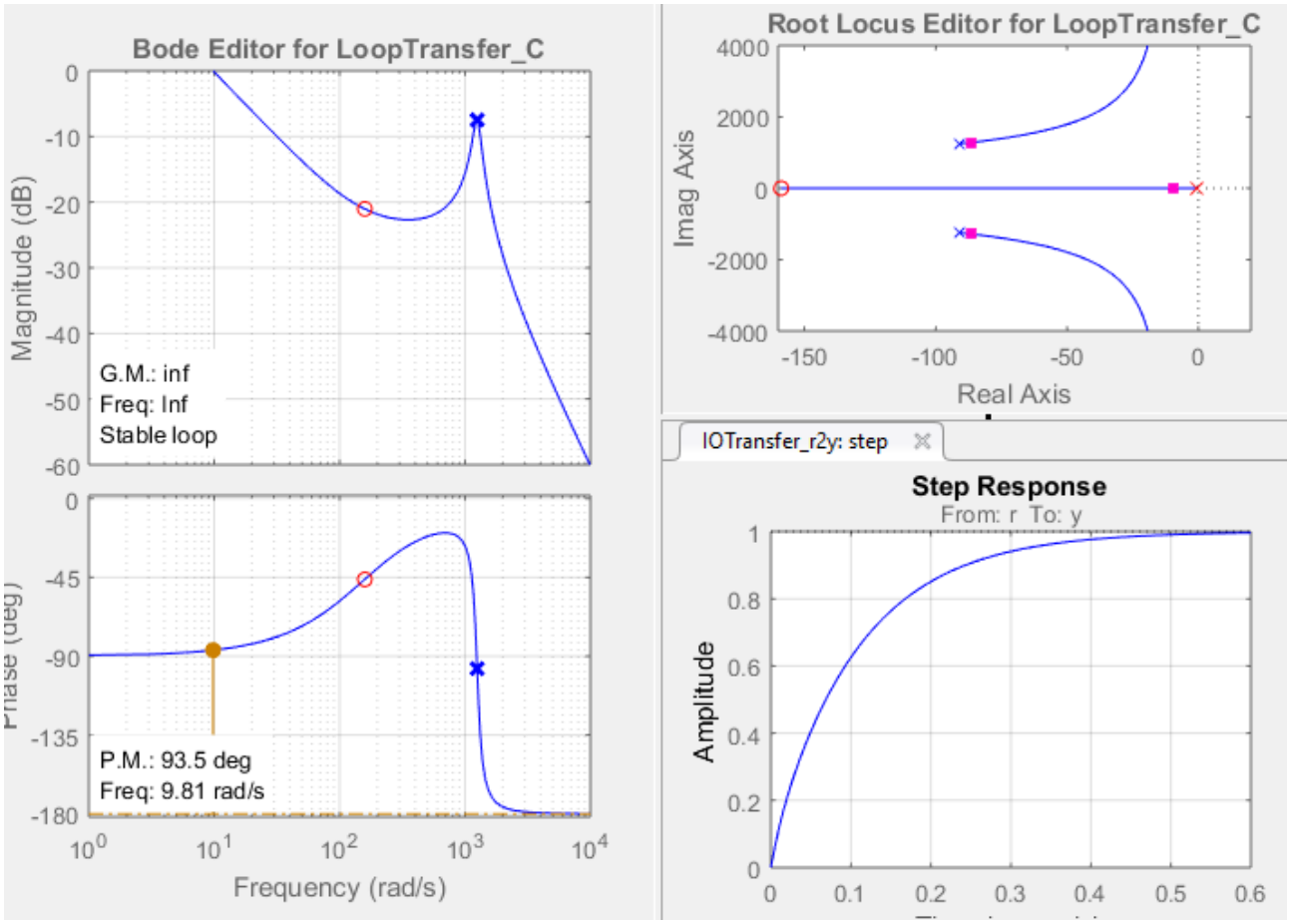

Figure 5.8: Voltage balancing loop closed loop response under PI compensation

The response shows a stable loop. The PI controller meets all the specifications of the system. The gain margin remains infinite and the phase margin in 93.5^{o}. The step response shows no overshoot or steady state error. The settling time is $6ms$ which is within the required specifications.

5.5.4 Filter Design

For EIS, the voltage and current perturbations of the battery had to be accurately measured by the NI-DAQ. The use of filters to reduce the switching component for EIS measurements was also done by [34]. An ideal filter, filters out all frequencies outside of the cut-off frequency. Practically, this is not achievable and thus there are types of filters that make trade-offs [42] The most common filter configurations are given in the table below with the advantage and disadvantage of different filter configurations.

Filter Type	**Pros**	**Cons**
Butterworth	Maximally-magnitude-response.	Transient response – moderate overshoot and ringing
Bessel	Excellent phase and transient response	Ripple in pass band, rate of roll-off is reduced

Chebyshev	Steeper roll-off	Ripple in passband

It is desired that the magnitude of the measured perturbation is as accurate as possible. Thus, a Butterworth filter was chosen due to its flat passband. The standard second-order low pass filter transfer function is shown in the equation below from [42] [43]:

$$H_{LP}(f) = -\frac{K}{(\frac{f}{FSF \times f_c})^2 + \frac{1}{Q}\frac{jf}{FSF \times f_c} + 1}$$

For a Butterworth filter, the FSF=1, for a 2nd order filter, the Q value = 0.7071. Therefore, for a unity gain Butterworth 2nd order low pass filter, fc = 5kHz. The equation reduces to

$$H_{LP}(f) = -\frac{1}{-(\frac{f}{5000})^2 + 1.414\frac{jf}{5000} + 1}$$

The low pass filter that was chosen was the unity-gain Sallen-Key active low pass filter. A second order unity gain Sallen key filter is shown in Figure 5. below. The advantage of this topology is that it can be cascaded in order to create higher order filters.

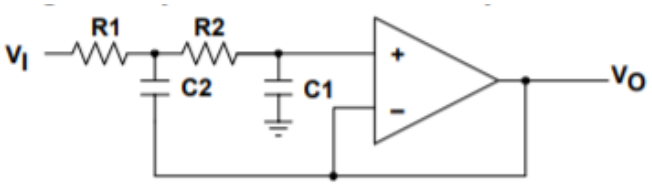

Figure 5.9: Unity-Gain Sallen-Key [43]

The following equations were used to obtain appropriate resistor and capacitor values for the Butterworth filter.

$$R_1 = mR_2\,, C \text{ and } C_2 = nC_1$$

$$Q = \frac{\sqrt{mn}}{m+1} = 0.7071\,, fc = \frac{1}{2\pi RC\sqrt{mn}} = 7000$$

$$m = 1, n = 2,$$

$$RC = \frac{1}{7000 \times 2\pi\sqrt{2}}$$

$$If\ C = 1nF, R = \frac{1}{10 \times 10^{-9} \times 7000 \times 2\pi\sqrt{2}}$$

The filter circuit was simulated in LT-SPICE. The circuit diagram is shown in Figure 5. below:

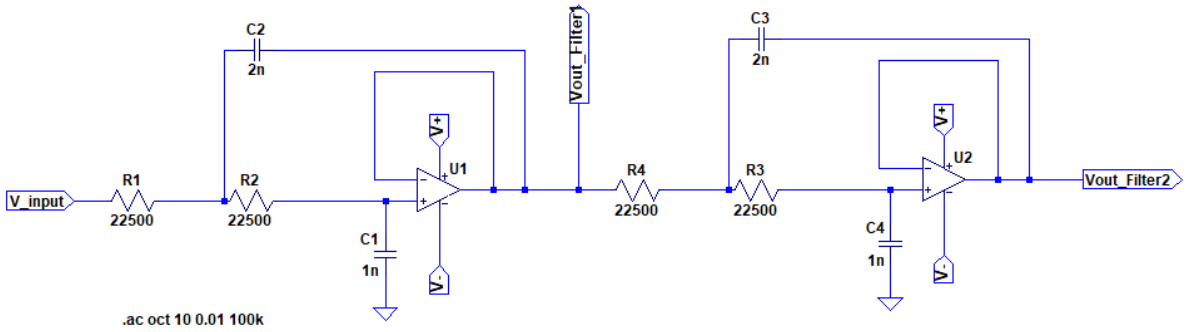

Figure 5.10: LTSPICE diagram of 4th order butterworth active low pass filter

The AC response was then measured over a wide range of frequencies to validate the filter. The voltage magnitude response and phase response are given by Figure 5. below. The blue line is the 2nd order filter's magnitude and phase response, the red line is the output of the 4th order cascaded 4th order Butterworth filter.

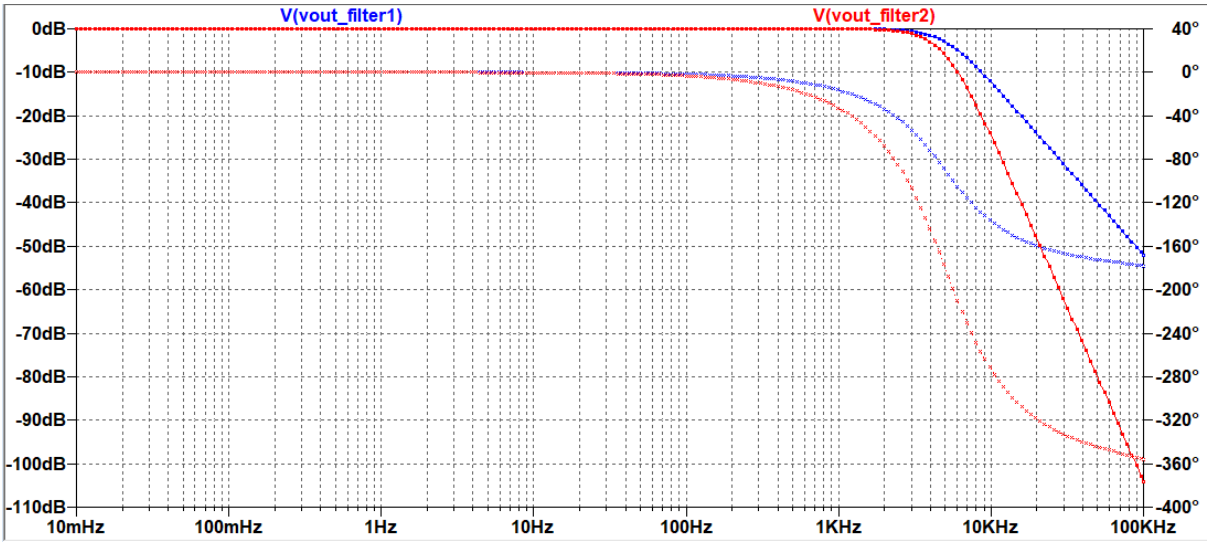

Figure 5.11: Magnitude and Phase response of low pass filters

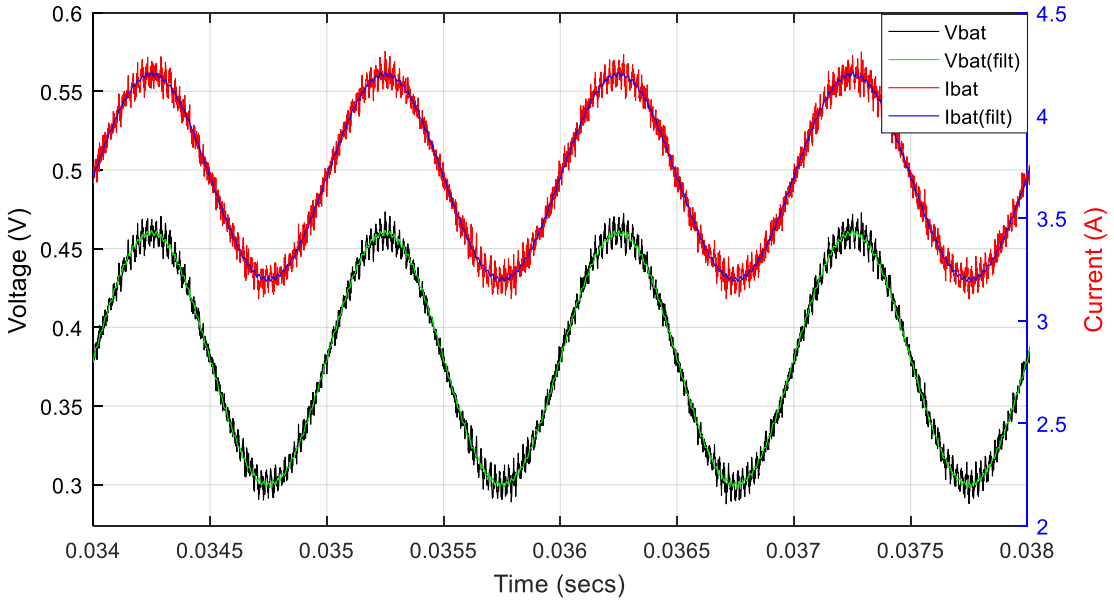

The voltage was obtained by sampling the battery voltage using an Analogue input of the NI-6366. The voltage and current measurements were then pass through an active 4th order Butterworth filter with a 5kHz cut off frequency.

6. THREE-LEVEL BOOST CONVERTER DC RESULTS

In this section the converter's DC performance was simulated and analysed before the EIS was performed. After which, its performance was then assessed experimentally, where by results are shown and discussed.

6.1 Three-level boost converter open-loop simulation

The three-level boost converter was simulated in MATLAB Simulink using the components values designed in chapter 5. The converter was simulated using a 22.1V input voltage and a load resistor of 22Ω – unless stated otherwise. The converter was simulated in both regions 1 and 2 to show its operation in these regions. Based on the design specifications, the converter reaches a minimum duty cycle of 48% and a maximum of 52% – as such, the behaviour of the converter's voltage; current and ripple, at these duty cycles was investigated. The converter was simulated with parasitic elements of the inductor, capacitor and switches included.

6.1.1 Output voltage

Figure 6.1 shows the open-loop voltage of the three-level boost converter at 48% and 52% duty cycles – which are regions 1 and 2, respectively.

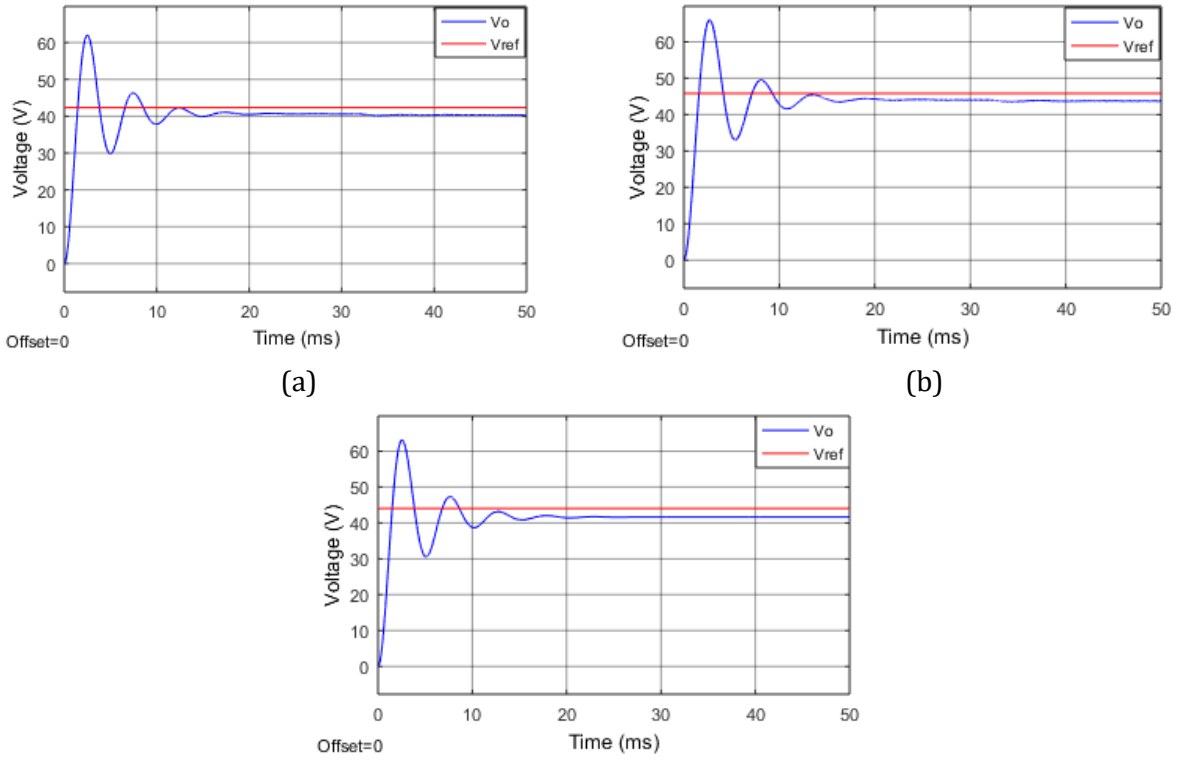

Figure 6.1: Open loop simulation of the output voltage (a) Region 1 (b) Region 2 (c) operating point

In Region1 – at 48% duty cycle – Figure 6.1 (a) shows the output voltage with a steady state a steady state error of $1.52V$; an overshoot of 50.61% and a settling time of $33ms$. Figure 6.1 (b) – at 52% duty cycle – the steady state error is larger at $1.87V$; an overshoot of 59.58% and a settling time of $34ms$. Figure 6.1 (c) shows the converter at its operating point with a steady state error of $2.1V$; an overshoot of 54.12% and the fastest settling of $22ms$. The converter showed similar steady state performance in Regions 1 and 2 within the EIS specifications. This enabled the EIS signal to be injected with minimal error.

6.1.2 Capacitor voltages

The capacitor voltages were simulated and shown in Figure 6.2, to observe their transient and steady state voltage balance behaviour in Region 1 and 2, and the operating point.

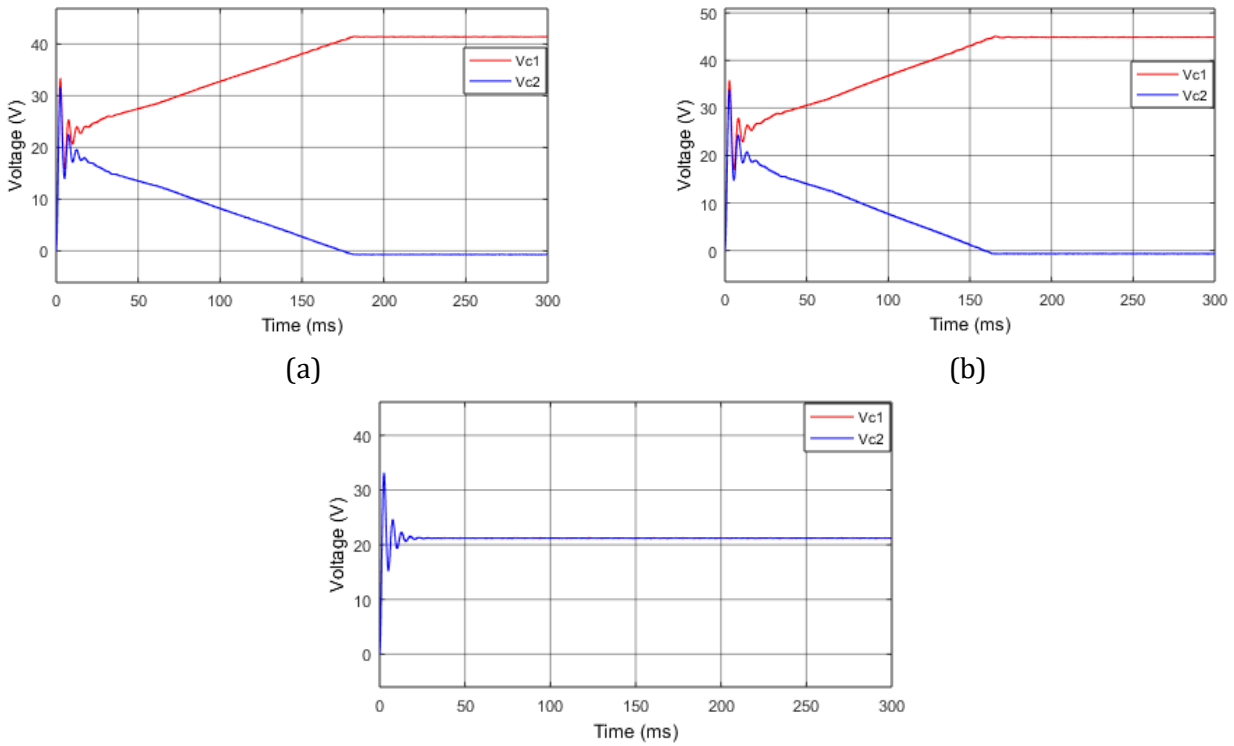

Figure 6.2: Open loop simulation of capacitors, voltages (a) Region 1 (b) Region 2 (c) operating point

Figure 6.2 (a) shows that the capacitor voltages are not balanced. At each point in time they add up to the output voltage. The voltages reach steady state in $170ms$ – which is above the required specification and slower than the output voltage steady state. The steady state value of V_{c1} is $42.37V$ and $-1.21V$ for V_{c2}. In practical implementation the capacitor voltage cannot be negative, therefore the voltage V_{c2} would have a lower saturation of $0V$ – which will result in a lower output voltage. Figure 6.2 (b) shows that the capacitors are also not balanced and reach steady state in $161ms$. This unbalance in the

capacitors causes the ripple at the output voltage to increase, which affects the design. The voltage stress across the switch S_1 doubles, which can be dangerous for the switch at power applications. Since the duty cycle will be varied within these duty cycles, a control was designed to balance the voltages across the capacitors. Figure 6.2 (c) shows the capacitor voltages at the operating point. The voltages are balanced at half the output voltage as per the design requirements.

6.1.3 Converter ripple

The converter's output voltage ripple, capacitor voltage ripple and inductor current ripples were simulated to show how the ripple of the converter changes from Region 1 to Region 2.

i. Output voltage ripple

The output voltage was designed to be less than 2% of the steady state value of the output voltage. Figure 6.3 shows the voltage ripple across the two regions and the operating point.

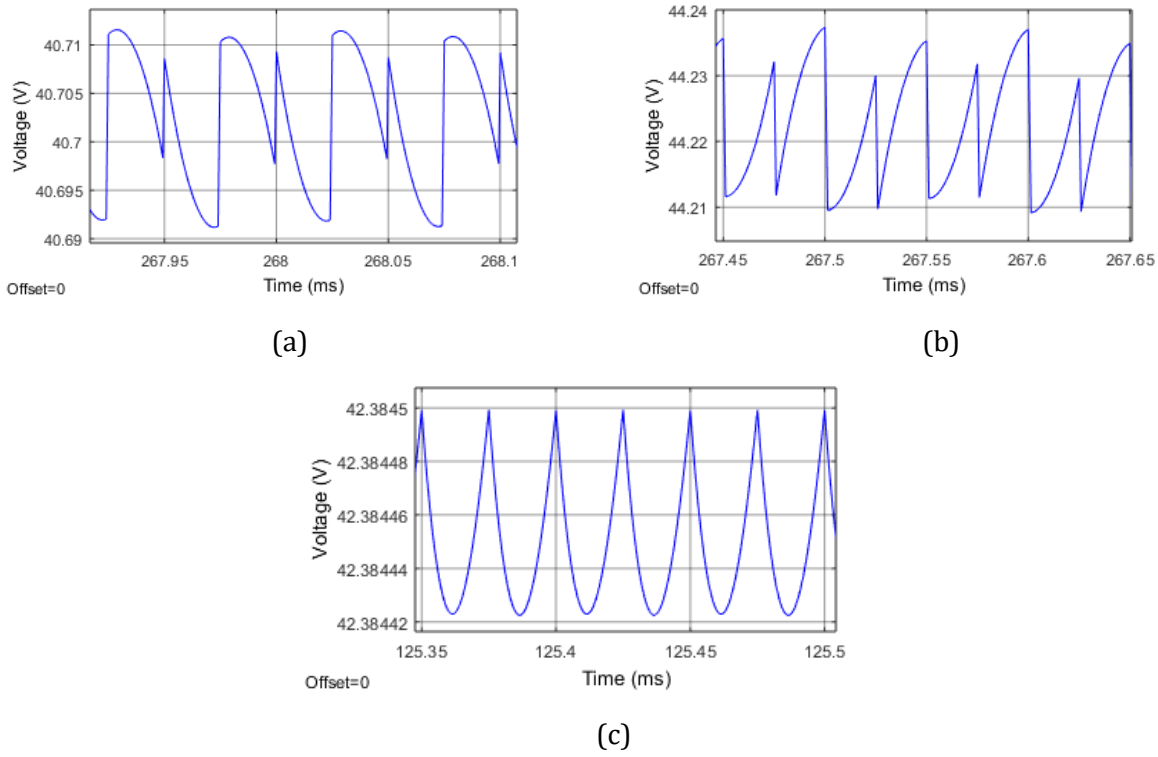

Figure 6.3: Open loop output voltage ripple (a) Region 1 (b) Region 2 (c) operating point

Figure 6.3 (a) shows that the output voltage ripple is the inverted version of Figure 6.3 (b) – this is due to the switching pattern as discussed in the analysis. The peak to peak ripple in Region 1 is 0.04% and 0.04% in Region 2 – this is because of the symmetry in the ripple. The output voltage ripple at the operating point is $8 \times 10^{-5}\%$ – which is close to zero, as analysed.

ii. Output capacitor voltage ripple

The output capacitors' voltage ripples were simulated to show the phase shift between the Regions 1 and 2.

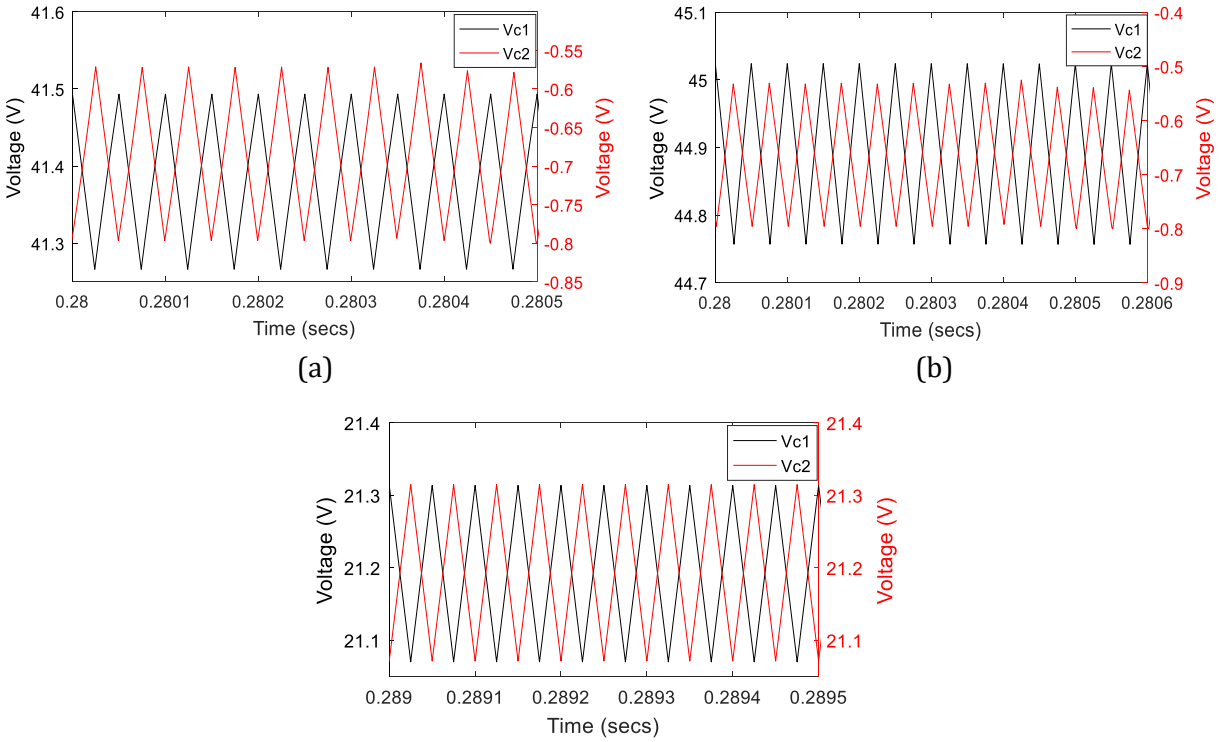

(a) (b)

(c)

Figure 6.4: Output capacitor voltage ripple (a) Region 1 (b) Region 2 (c) operating point

Figure 6.4 shows that the capacitor voltage ripples are shown to be 180^{o} out of phase, this reduces both the ripple at the output voltage. The peak to peak voltage ripples in both Region 1 and 2 are shown to be different in size, but the capacitor ripples at the operating point are equal in magnitude.

iii. ***Inductor current ripple***

The simulated inductor ripple magnitude in comparison is shown for EIS sinusoidal current in both regions and the operating point.

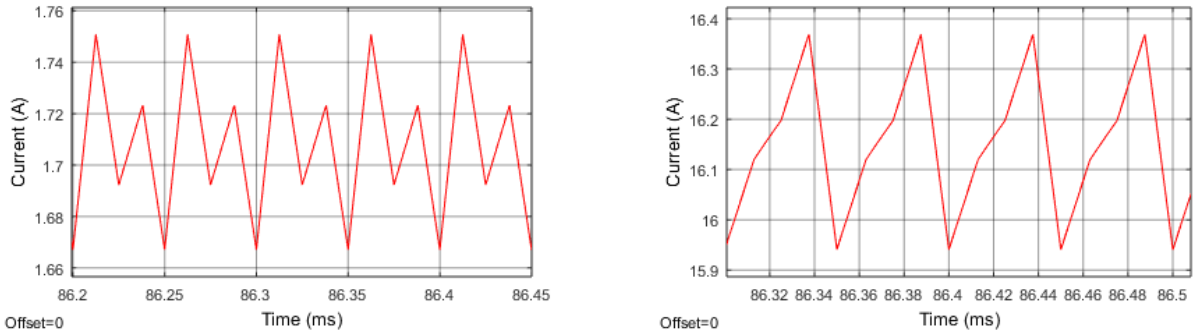

(a) (b)

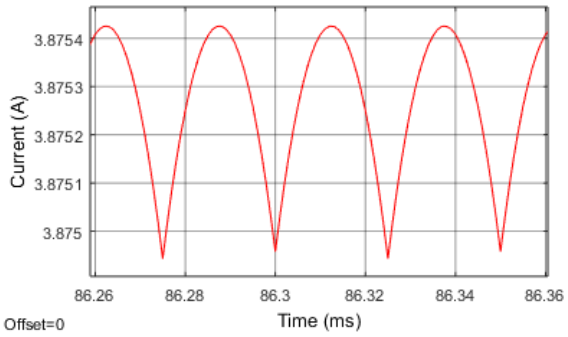

(c)

Figure 6.5: Open loop simulation of the input inductor current (a) Region 1 (b) Region 2 (c) operating point

Figure 6.5 (a) shows a ripple inductor current with a peak to peak ripple of 4.6% of the average value. This ripple is $80mA$ which is much smaller than the $1.6A$ peak to peak AC EIS current. The ripple shows 4 states where the inductor charges through switch S_1 and then both switches remain OFF and then the inductor discharges. The inductor then charges again through switch S_2 and the current rises until the switch turns OFF and then the inductor discharges. When both the switches are OFF, the potential at the input is higher than the output, hence the inductor discharges. Figure 6.5 (b) shows the ripple in Region 2 with a peak to peak current of $40mA$ which is also small enough for EIS implementation. Figure 6.5 (c) shows the current ripple at the operating point; the current has a peak to peak ripple of $500\mu A$ – which is close to zero as expected from the analysis of the converter.

6.2 The three-level boost converter closed-loop simulation result.

The open loop simulations showed that the converter has some significant performance differences between Regions 1 and 2 – this is not ideal since during EIS implementation, the converter will be operating at the boundary of both these regions. The converter was then operated under closed loop control as design for in chapter 5. The control was implanted digitally in MATLAB Simulink, using a fundamental step size of $1 \times 10^4 s$. The simulation input voltage and load resistor were the same as those in the open loop.

6.2.1 Output voltage

The output voltages in Regions 1 and 2 and the operating point are shown in Figure 6.6.

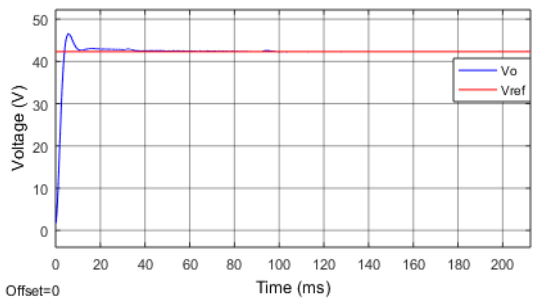

(a)

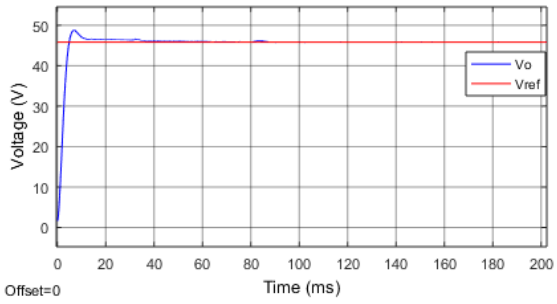

(b)

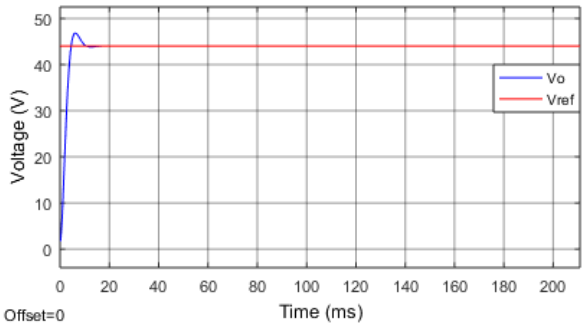

(c)

Figure 6.6: Output voltage closed loop simulations (a) Region 1 (b) Region 2 (c) operating point

Figure 6.6 (a) shows that the output voltage in Region 1 had an overshoot of 7% which meets the design specifications. The settling time for the voltage was $32ms$ which also meets the design requirements. The steady state error for the voltage had reduced to $0.01V$. The steady state ripple in the output voltage was 0.9% which is within the design specifications. Figure 6.6 (b) shows the output voltage in Region 2. The voltage also meets all the design specifications. Figure 6.6 (c) shows the output voltage at the operating point which settles within $10ms$ and an output voltage ripple of less than 5% - which is within the design requirements.

6.2.2 Capacitor voltages

The open loop simulations showed that the capacitors' voltages were unbalanced and led to higher voltage ripples and longer settling time in the output voltage. The control has a third loop dedicated to balancing the voltages across the capacitor such that the steady state performance of the converter could be improved. The capacitor voltage balancing control was introduced at time $50ms$ to ensure that the capacitor voltages were balanced; Figure 6.7 shows the closed loop results.

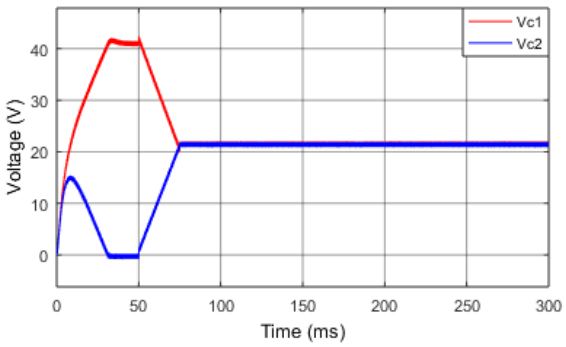

(a)

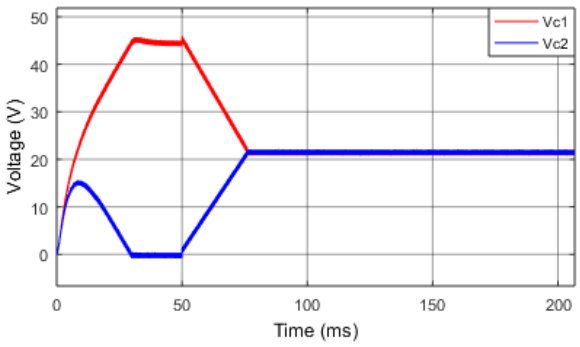

(b)

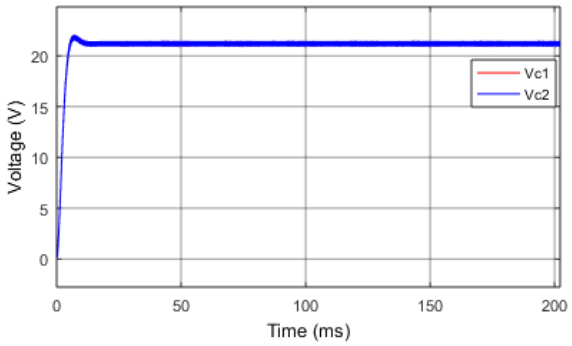

(c)

Figure 6.7: Output capacitor voltage closed loop simulation (a) Region1 (b) Region (2) operating point

Figure 6.7 (a) and (b) show that when the capacitor balancing control loop was introduced, the capacitor voltages reached a balanced voltage of half of the output voltage in approximately $25ms$. This means that when EIS is implemented, steady state would be reached at time $75ms$ and there would be minimal variation in the steady state performance of the converter.

6.3 Experimental DC results of the three-level converter

The converter was assembled in the lab for experimental testing. The results were compared to the simulated results. As shown in Figure 6.11, the converter was built on a Veroboard for simple debugging.

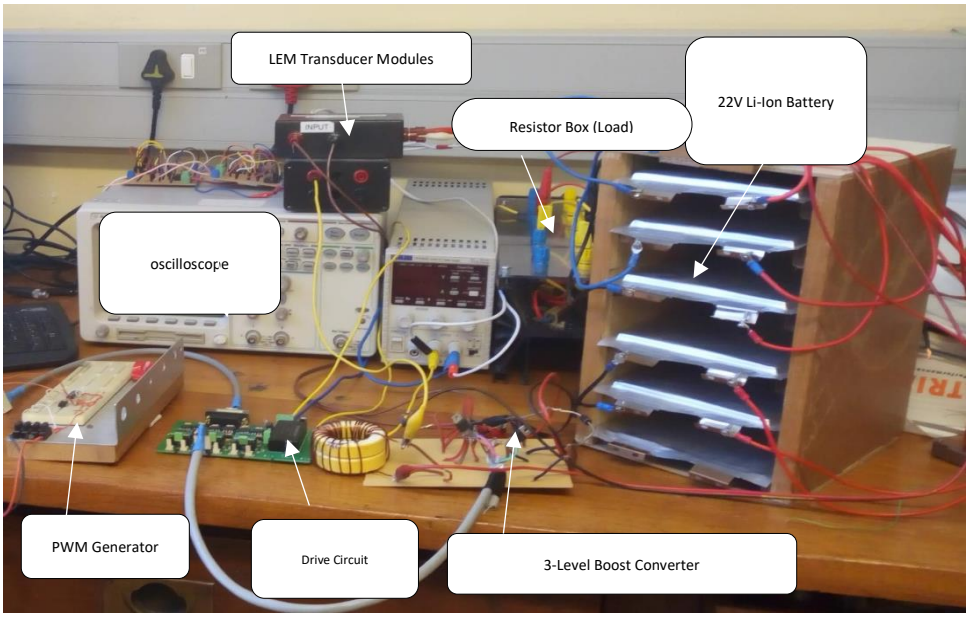

Figure 6.8: Experimental set of the three-level boost converter

The driver outputs $18V$ to fully switch the MOSFET on. An NI DAC was then integrated with MATLAB Simulink to analyse the voltage and current signals.

6.3.1 *Closed loop experimental results*

The converter was powered from 6, 3.6V LI ion batteries connected in series, which output a DC terminal voltage of 22.1V. The converter and battery supplied a 22Ω DC load. The response is shown in Figure 6.9. The closed loop was implemented on Simulink using an NI DAC as the digital to analogue interface.

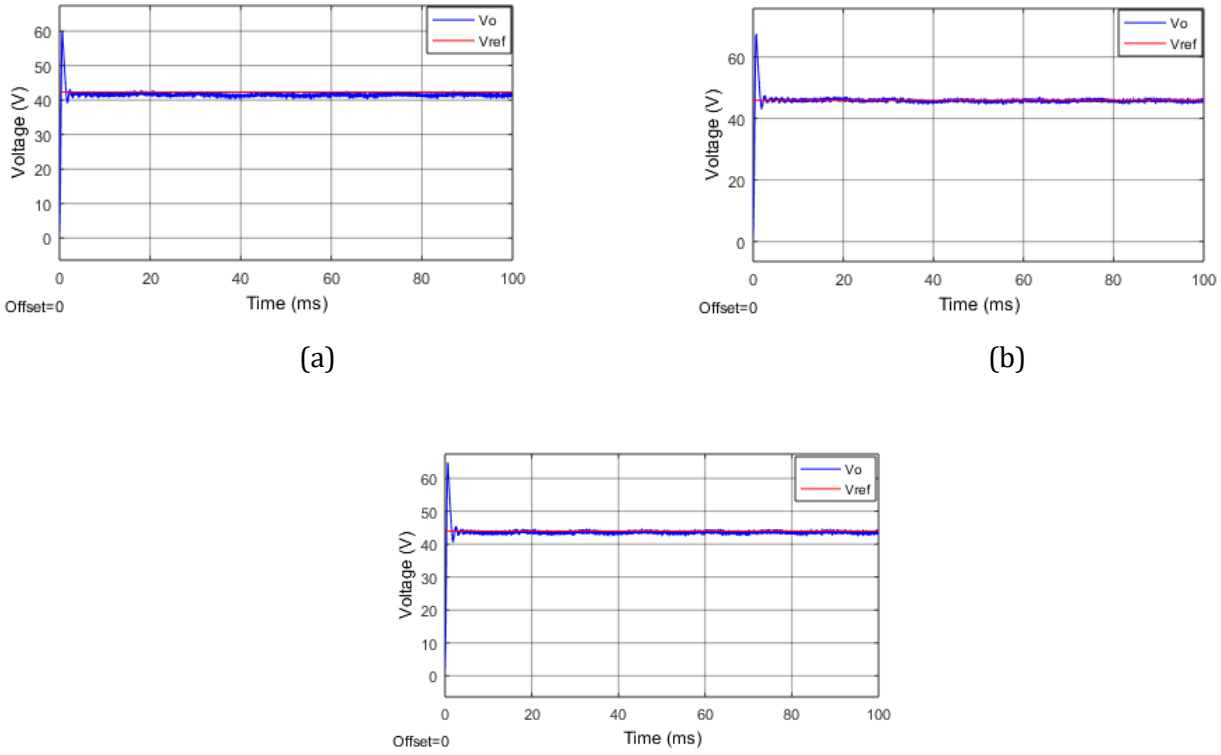

Figure 6.9: Experimental closed loop results of the output voltage (a) Region 1 (b) Region 2 (c) operating point

The output voltage reaches a steady state error of approximately 0.25V in all three regions. This steady state error is because of the voltage drops across the inductor and wiring of the converter. It is also due to the low gain achieved in open loop because of the parasitic elements of the inductor, capacitor, the two switches and the two diodes. The overshoot of the voltage is 47% which is larger than the desired value and significantly larger than the simulated results. This settling time is approximately 20ms because of the components used in the design, such as the transducers and external filters.

6.3.2 *Capacitor voltages*

The capacitor voltages were measured to show the balancing and the results shown in **Figure 6.10**.

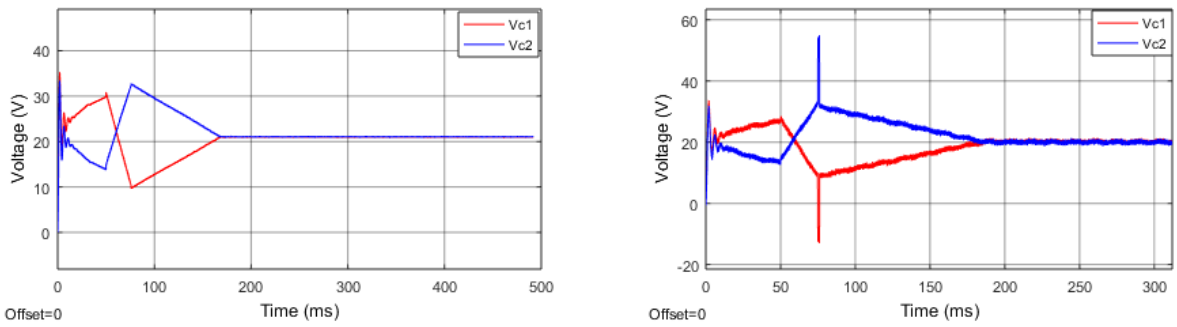

(a) (b)

Figure 6.10: Experimental closed loop capacitor voltages (a) Region 1 (b) Region 2

The capacitor voltages are shown to balance at time $175ms$. The control manages to get balance the capacitor voltages after $175ms$. Figure 6.10 (b) shows a large spike in voltage. This is because during Region2, the duty cycle is larger than 50% - hence, the control input overshoots and increases the duty cycle to values larger than 1, which causes the spike.

6.3.3 Inductor current ripple

The inductor current ripple was tested in Region 1, Region 2 and the operating point and the results shown in Figure 6..

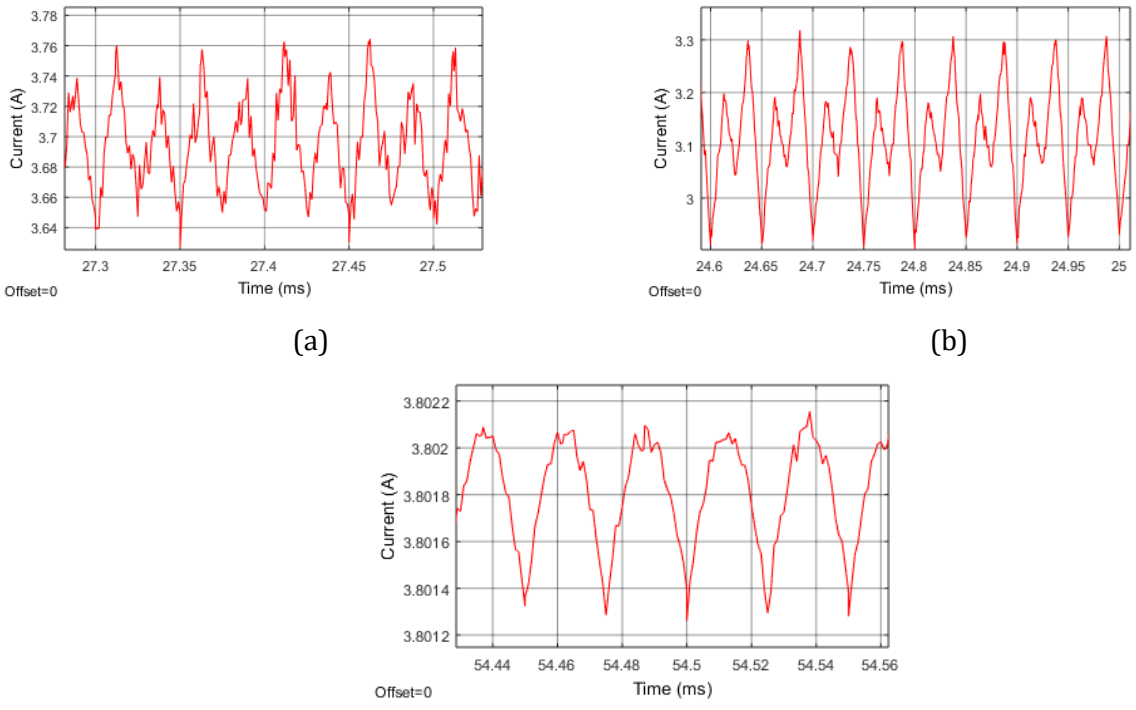

(a) (b)

(c)

Figure 6.11: Experimental inductor current ripple (a) Region1 (b) Region 2(c) operation point

Figure 6. (a) shows that the inductor ripple increased by 3.2% from the simulations. Figure 6. (b) shows a 3.9% increase and Figure 6. (c) shows a 0.9% increase from the simulations. These increases are as a result of the equipment inaccuracies of the experimental setup.

6.4 Converter performance as a function of the duty cycle

The performance of the three-level boost was assessed as the duty cycle was varied. This was done in both Region 1 and Region 2 to observed which region offers the best results. The load was adjusted to draw the rated current and the battery voltage was also kept constant.

6.4.1 Region 1 performance assessment

In the Region 1, the duty cycle varies from only 0% up to, and including, 50%. But in practice the minimum duty cycle reached was 15.41%, as shown Table 6-1, because of the switch utilization at these lower duty cycles and the limitation of the equipment that was used. The equilibrium point shifted from 50% to 53% duty cycle, as discussed because of the parasitic elements of the converter.

Table 6-1 Three-level boost converter Region 1 performance as function of the duty cycle with a constant load

$d(t)$	$V_{in}(V)$	$I_{in}(A)$	$P_{in}(W)$	$V_o(V)$	$I_o(A)$	$P_o(W)$	ΔV_o	ΔI_{in}	eff	$gain$
15,41	22,06	13,53	298,47	23,15	10,15	234,9725	4,02	6,75	0,78	1,04
20,14	22	14,2	312,4	24,25	10,36	251,23	3,75	6,53	0,80	1,10
25,21	22,1	16,52	365,09	27,89	10,06	280,5734	3,5	6,38	0,76	1,26
30,03	22,06	18,72	412,96	32,13	10,2	327,726	3,43	5,45	0,79	1,45
34,98	22,01	19,53	429,85	35	10,03	351,05	3,35	5,02	0,81	1,59

The results were then represented graphically to show how the converter performed experimentally.

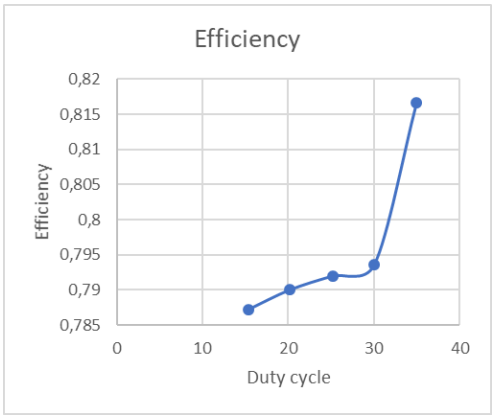

(a)

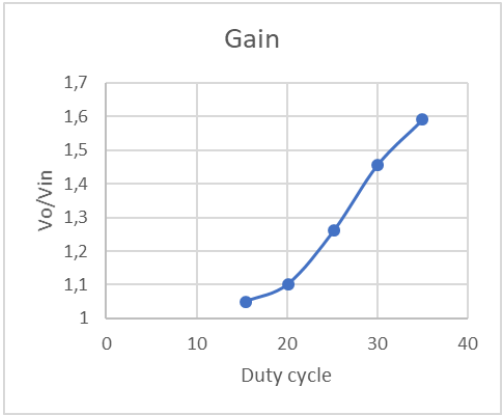

(b)

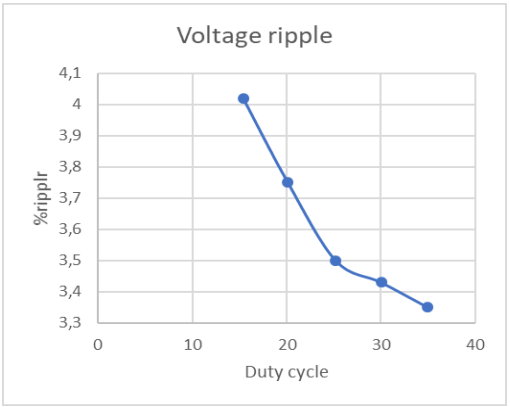

(c)

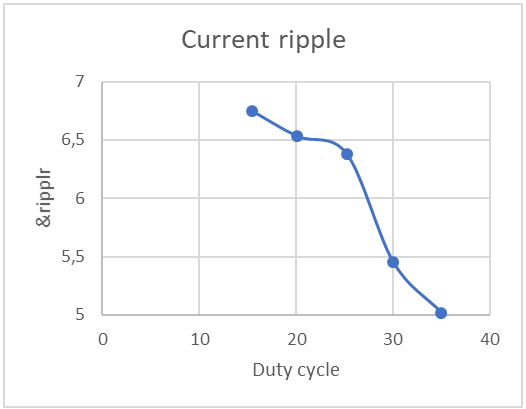

(d)

Figure 6.12: Converter Region 1 performance (a) Efficiency (b) Gain (c) Voltage ripple (d) Current ripple

Figure 6. (a) shows that the converter's efficiency rises and reaches a peak efficiency of 84% around the equilibrium point. The gain of the converter in Figure 6. (b) increases linearly and reaches a peak gain of 2 at the equilibrium. Figure 6. (c) and (d) show that the ripples decrease as the duty cycle approaches 50% which is when the capacitors are output phase by the maximum phase of 180 as analysed.

6.4.2 Region 2 performance assessment

In Region 2, the duty cycle ranges from 50%, but not including, to 100%, but because of practical limitations due to the parasitic elements and poor switch utilization at higher duty cycles, the duty cycle was varied from 54% to 83.12%, as shown in Table 6-2

Table 6-2 Three-level boost converter Region 2 performance as function of the duty cycle with a constant load

$d(t)$	$V_{in}(V)$	$I_{in}(A)$	$P_{in}(W)$	$V_o(V)$	$I_o(A)$	$P_o(W)$	ΔV_o	ΔI_{in}	eff	$gain$
53,69	22,06	15,36	338,84	44,02	5,075	223,40	4,02	6,75	0,66	2,78
55,65	22	17,35	381,70	46,23	5,02	232,07	4,35	6,89	0,61	2,41
60,23	22,1	18,05	398,91	49,23	5,01	246,64	4,86	7,12	0,62	2,23
64,58	22,06	18,99	418,92	53,12	5	265,60	5,32	7,86	0,63	2,40
68,45	22,01	19,86	437,12	61,23	5,06	309,82	6,32	8,36	0,53	2,00

The tabulated results were represented graphically as shown by Figure 6..

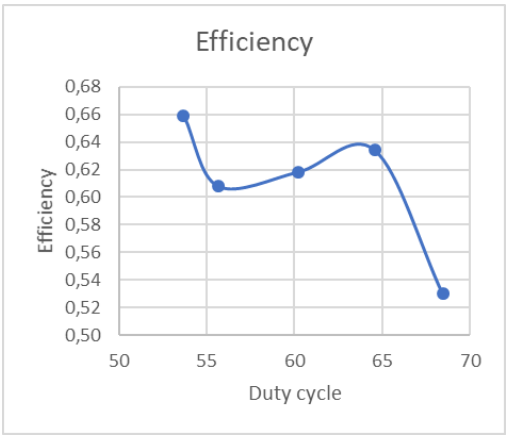

(a)

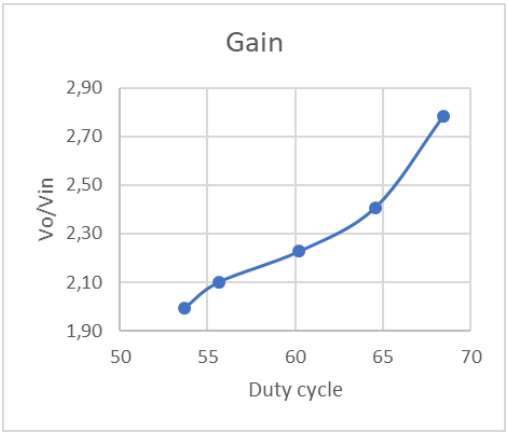

(b)

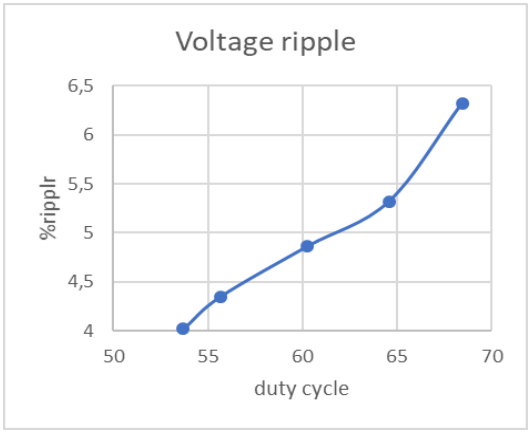

(c)

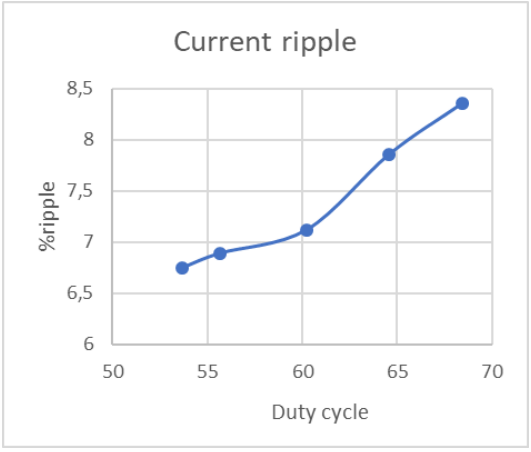

(d)

Figure 6.13: Converter Region 2 performance (a) Efficiency (b) Gain (c) Voltage ripple (d) Current ripple

Figure 6. (a) shows that the converter's efficiency reaches a peak of 66% at 54% duty cycle. The efficiency then falls off at larger duty cycles because of the parasitic elements. The gain of the converter in Figure 6. (b) decreases from a maximum of 2.78 – this low gain is also because of the parasitic elements. Figure 6. (c) and (d) show that the ripples in the voltage and inductor decrease as the duty cycle approaches 50% which is when the capacitors are output phase by the maximum phase of 180˚ as analysed.

6.5 Converter performance as a function of load power

The load power of the converter was varied using a constant load source and keeping both the duty cycle and battery voltage constant. This was also done in both Region 1 and Region 2.

6.5.1 Region 1 performance

The duty cycle was kept constant at 53% duty cycle and the load current was varied from $0.5A$ to $4A$ as shown in Table 6-3.

Table 6-3 Three-level boost converter Region 1 performance as a function of the load power with a constant duty cycle

$d(t)$	$V_{in}(V)$	$I_{in}(A)$	$P_{in}(W)$	$V_o(V)$	$I_o(A)$	$P_o(W)$	ΔV_o	ΔI_{in}	eff	$gain$
53	22,1	2,815	62,2115	44,56	0,51	22,7256	1,25	2,65	0,365295805	2,016
53	22	3,51	77,22	44,25	0,78	34,515	1,35	2,69	0,446969697	2,011
53	22,01	3,78	83,1978	43,98	1,16	51,0168	1,53	2,75	0,613198907	1,998
53	22,03	4,99	109,9297	43,25	1,82	78,715	1,83	3,52	0,716048529	1,963
53	22	5,615	123,53	42,01	2,29	96,2029	2,02	4,68	0,778781672	1,909
53	22,02	6,18	136,0836	40,25	2,56	103,04	2,56	5,68	0,757181615	1,827
53	22	7,115	156,53	39,98	2,84	113,5432	2,96	5,98	0,725376605	1,817
53	22	8,4	184,8	39,85	2,935	116,95975	3,69	6,35	0,63289908	1,811
53	22,01	9,75	214,5975	39,78	3,115	123,9147	3,87	6,4	0,577428442	1,807

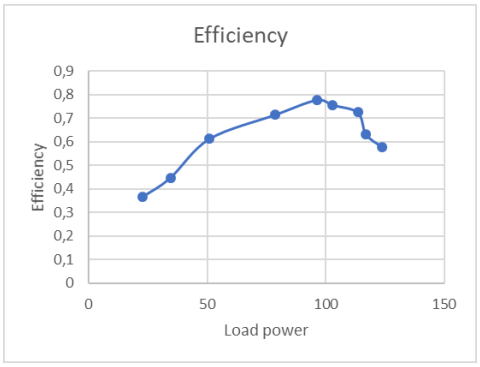

(a)

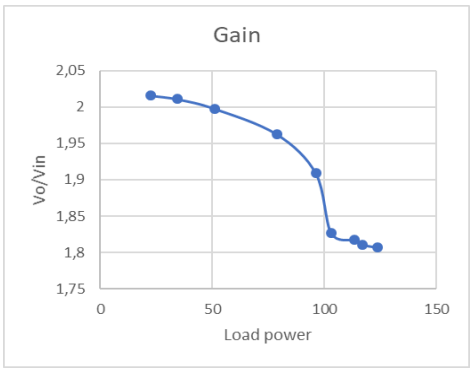

(b)

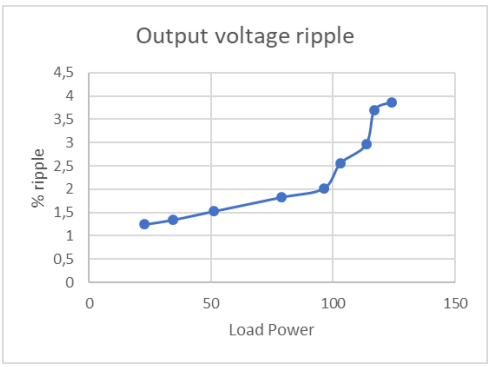

(c)

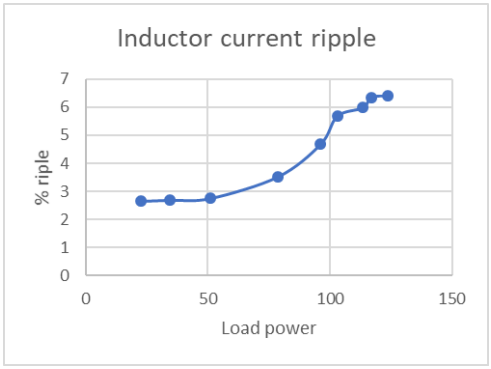

(d)

Figure 6.11: Three-level boost converter Region 1 performance as a function of the load power with a constant duty cycle

Figure 6.11 (a) shows that the converter's efficiency reaches a peak of 78% at an output power of 98W. The efficiency falls off as heavier loads. The gain of the converter in Figure 6.11 (b) decreases as the load increases – this low gain is also because of how the parasitic elements affect the gain. Figure 6.11 (c) and (d) show that the ripples in the voltage and inductor increase as the load increases. This is because the system is under strain.

6.5.2 Region 2 performance

The duty cycle was kept constant at 63% duty cycle and the load current were varied from 1A to 6A as shown in Table 6-4.

Table 6-4 Three-level boost converter Region 2 performance as a function of the load power with a constant duty cycle

$d(t)$	$V_{in}(V)$	$I_{in}(A)$	$P_{in}(W)$	$V_o(V)$	$I_o(A)$	$P_o(W)$	ΔV_o	ΔI_{in}	eff	$gain$
63	22,06	4,45	98,08	53,02	0,78	41,60	5,32	7,89	0,42	2,6
63	22	5,88	129,46	53,23	1,20	63,88	5,65	7,99	0,49	2,6
63	22,1	6,68	147,73	53,36	1,78	95,23	5,99	8,35	0,64	2,6
63	22,06	10,53	232,31	53,85	2,80	150,78	6,45	8,69	0,65	2,51
63	22,01	14,12	310,85	54,69	3,52	192,68	7,02	8,73	0,62	2,5
63	22,04	14,12	311,27	55,98	3,94	220,48	7,76	8,36	0,71	2,42
63	22,1	14,89	329,12	56,36	4,37	246,25	7,98	8,69	0,75	2,4
63	22,06	17,97	396,40	56,65	4,52	255,80	8,26	9,23	0,65	2,4
63	22	19,51	429,17	56,23	4,79	269,47	8,29	9,36	0,63	2,3

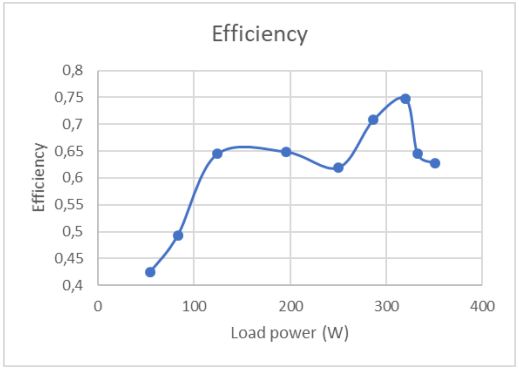

(a)

(b)

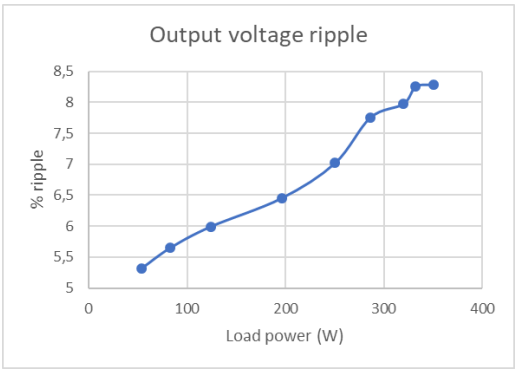

(c)

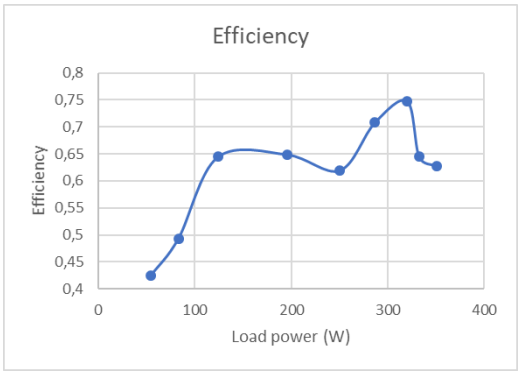

(d)

Figure 6.5: Three-level boost converter Region 2 performance as a function of the load power with a constant duty cycle

Figure 6. (a) shows that the converter's efficiency reaches a peak of 75% at an output power of $320W$. The efficiency falls off as heavier loads. The gain of the converter in Figure 6. (b) decreases as the load increases – this low gain is also because of how the parasitic elements affect the gain. Figure 6. (c) and (d) show that the ripples in the voltage and inductor increase as the load increases.

7. EIS RESULTS AND DISCUSSIONS

In this section the EIS was first implemented using the FRA device, from which the parameters for the EEC were extracted. After which the three-level boost converter was experimentally implemented and analysed before the EIS was performed.

7.1 FRA EIS implementation on Lithium-ion stack

The cells that was chosen to test EIS was EIG Lithium-Ion NCM cells. The 6x 20Ah cells were connected in series each having a nominal voltage of $3.65V$. The EIS measurement was perform in a galvanostatic mode. The frequency measurement ranges from $0.1Hz - 2kHz$ and the SoC was $100\%, 50\%$ and 25%. Before the battery model can be simulated, the parameterization value was derived from the FRA which was then used for the EEC battery model in Figure 3.1. The frequency selection ranges from $0.1Hz - 2kHz$. The battery current was set to $4A$ so that it won't charge the battery SoC significantly during the period of measurement. Figure 7.1 experimental FRA setup.

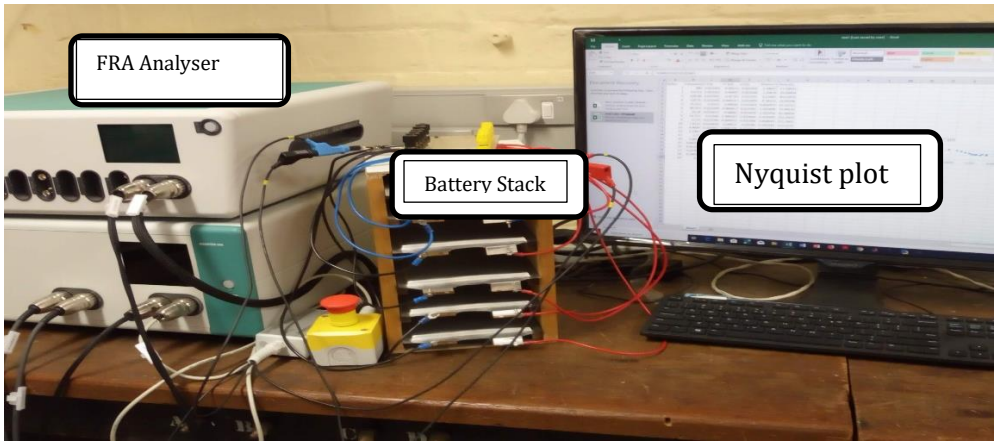

Figure 7.1: The Experimental FRA Setup with Lithium ion battery stack.

7.2 Converter EIS setup

A non-isolated three level DC-DC boost converter was designed to implement EIS on the LI-ion battery. The block diagram for the experimental set up is shown in Figure 7.2. The converter topology is used to discharge the battery while the impedance measurement is taken place. The EIS signal is applied to the switch of the converter to vary the duty cycle at steady state condition while the capacitor voltage is being balanced to ensure steady state of operation. The control signal was created on the MATLAB Simulink, the DAC was interfaced with the MATLAB through a DTB (Data Toolbox). The signal was injected in MATLAB to generate the modulating duty cycle. The overall hardware setup is shown in Figure 7.3.

The experimental test conducted on the converter, were done to match the simulations carried out in the previous section. The control was digitized using the backward difference equation, with a time constant of $2 \times 10^{-4} sec$. During the open loop experimental tests, the output voltage at 50% duty cycle was $41.2V$ and required a duty cycle of 52.1% to reach a steady state value of $44V$ as designed for – this was due to the losses along the connections and the voltage drops across the two diodes.

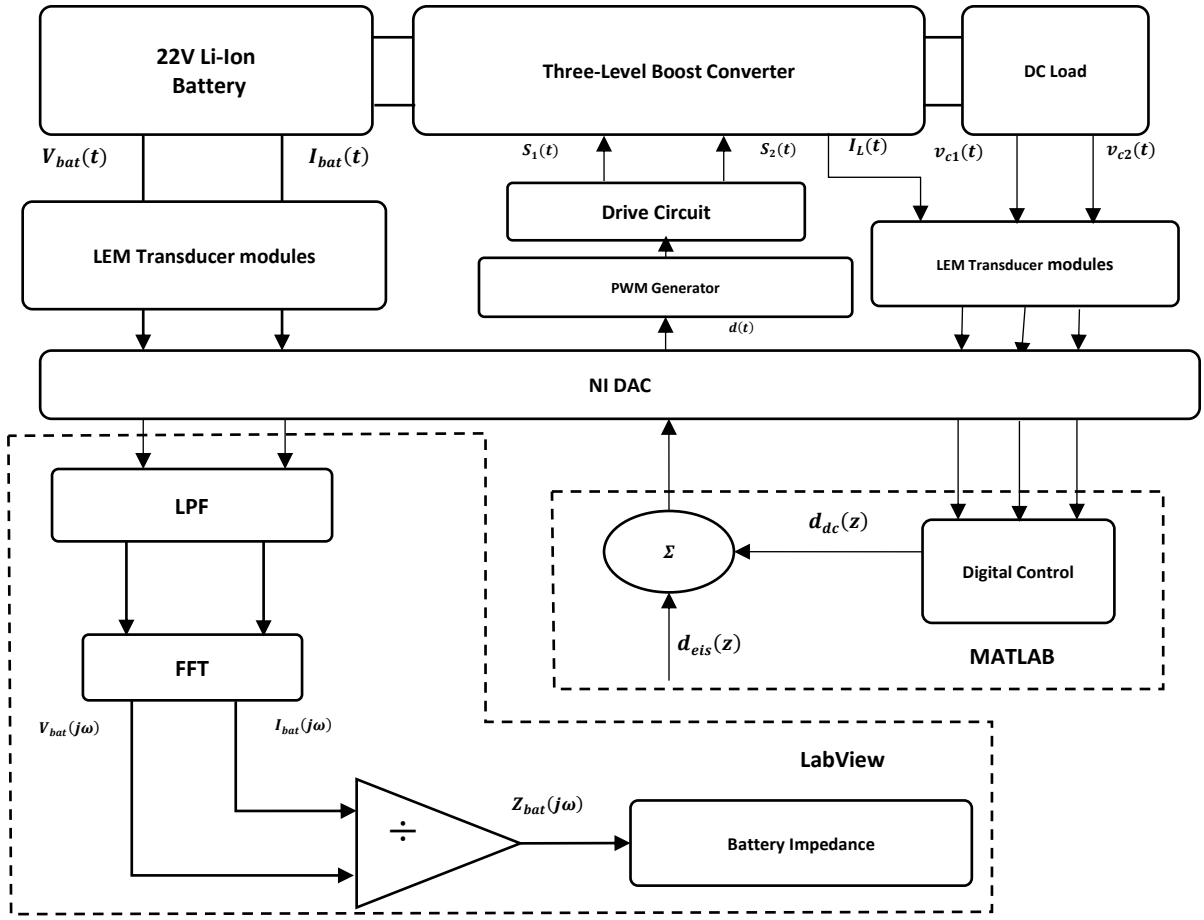

Figure 7.2: Experimental Converter EIS step-up block diagram

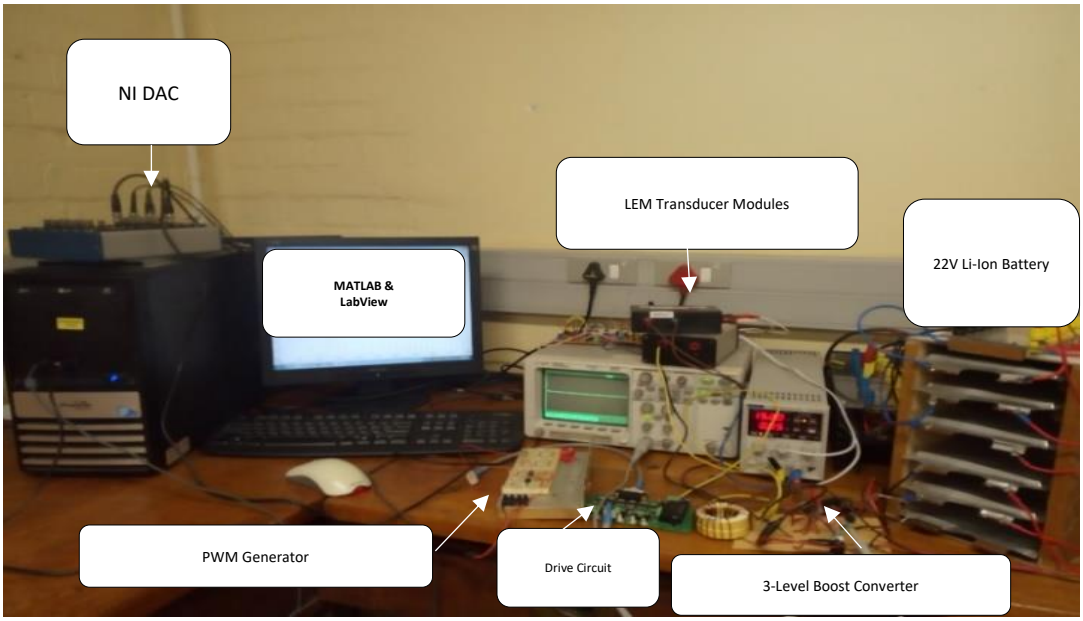

Figure 7.3: Experimental setup of the converter EIS.

7.3 FRA EIS results

The EIS test performed on the Lithium-ion cell was first implemented on a standard FRA, which is the industry standard for conducting EIS. The EIS on the Lithium-ion cell is tested at different Soc of the battery and at different discharge current of the battery. The FRA results of SoC and effect of discharge current are explained in the next section.

7.3.1 FRA Results - effects of SoC

The EIS testes were compared of a Lithium -ion cell at 20°C at a DC bias of 2A. The Figure 7.4(a) shows the FRA result at different states of charge of 25%, 50% and 100%. The basis of using a FRA to conduct the impedance test on the Lithium-ion battery is that the results will serve as a benchmark for the and simulation and experimental results.

Another way to visualize the impedance information of the lithium-ion battery is using the Bode plot. The bode plot of the different SoC of the battery at a DC bias of 2A is shown in the Figure 7.4(b) below.

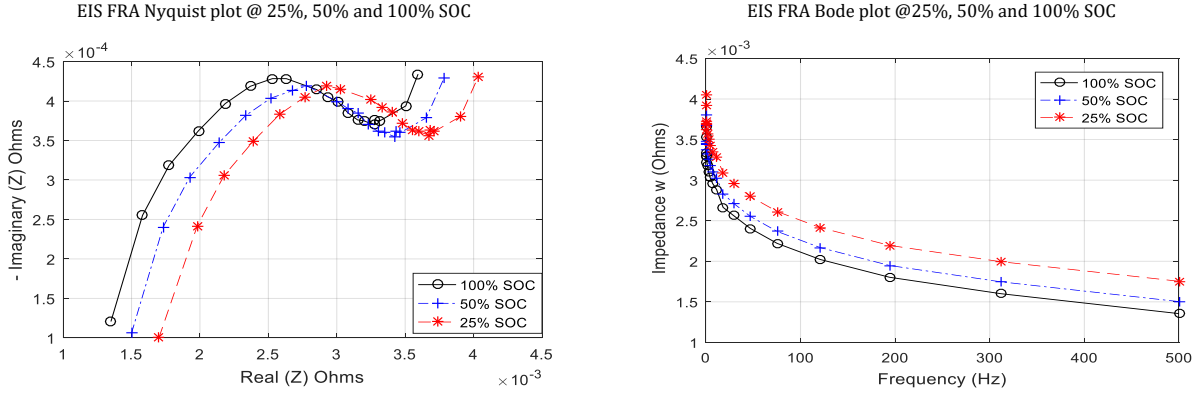

(a) (b)

Figure 7.4: (a)Nyquist plots (b) Bode plot 0.5A using FRA 25%, 50% and 100%

7.3.2 FRA Results - effect of discharge current on Li-ion batteries

The next experiment was used to investigate the impact of varying the discharge on the impedance of the Lithium-ion cells. The discharge currents selected are $2A$ *and* $3A$. Figure 7.5 shows the Nyquist plot of the effect of discharge current using FRA, the diagram shows the difference in impedance of the battery for both current.

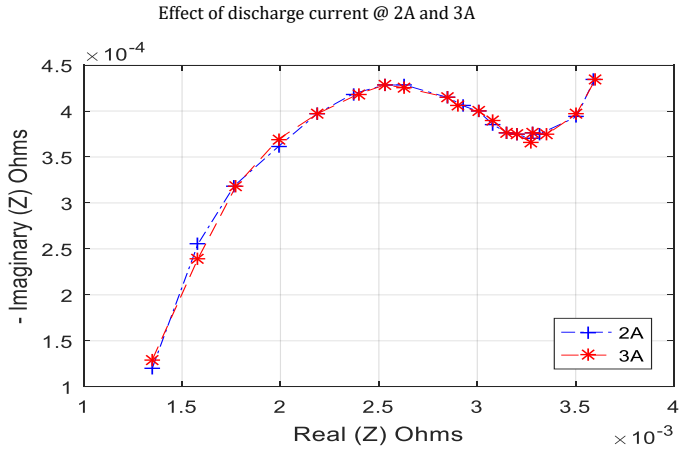

Figure 7.5: Nyquist plots results using FRA to implement EIS at a discharge current of 2A and 3A.

7.4 Converter simulation with EIS

The converter was first simulated with the Lithium-ion battery model. We have different ways of the battery modelling, but the accepted one for the battery cell is the electrical equivalent circuit (EEC) model which consists of RC network and frequency dependent impedance. The EEC model was used to represents the battery model in the SIMULINK environment.

The Nyquist data sheet obtained from the Nyquist plot of the FRA result was used to derive the EEC parameters. The EEC parameters where obtained from the result of the previous FRA results section. It is important to compare the simulation result with the FRA before it is experimentally validated. The table 7-1 shows the EEC parameterized value used in simulating the converter with EIS.

Table 7-1: Battery Parameterizes Estimation Value

SoC	25%	50%
EEC Parameters	Values	Values
R_s	0.00012	0.00051
R_{ct}	0.006	0.0028
CPE	16.0337	14.0135
W	0.39	0.27

7.4.1 *Effect of SoC of the Li-ion battery*

The parametrization test was conducted at two different SoC. Figure 7.6(a) (b) shows the parameter's simulation result with FRA results at 25 % *and* 50% SoC.

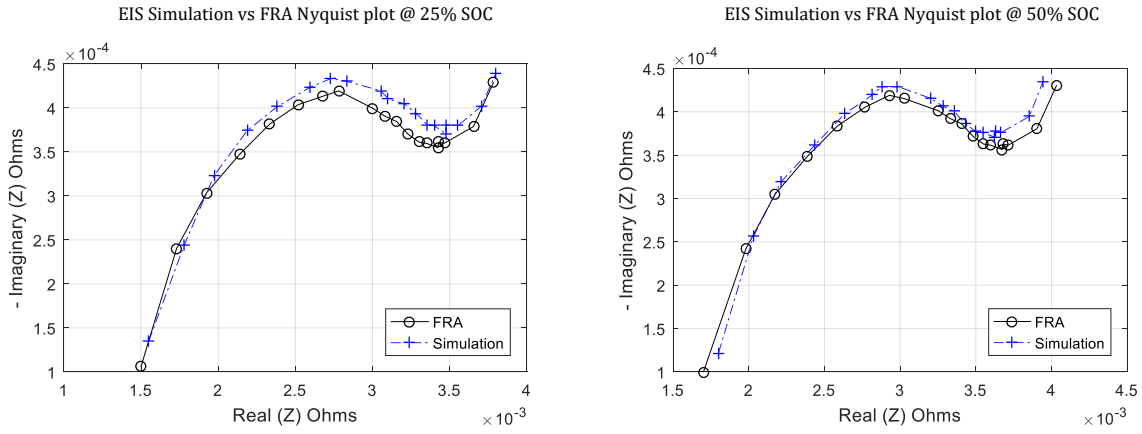

(a) (b)

Figure 7.6: Nyquist Plots simulation results (a) 25% SoC and (b) 50% SoC

Figure 7.7 shows the bode plot for simulation of the discharge current of the switching converter with the obtained parameterization the li-ion cell at 25% *and* 50 % SoC using the FRA results as the benchmark. The converter simulated with MATLAB did not properly describe the Warburg impedance at an angle of 45°. This is because the Warburg element was approximated using CPE for the simulation.

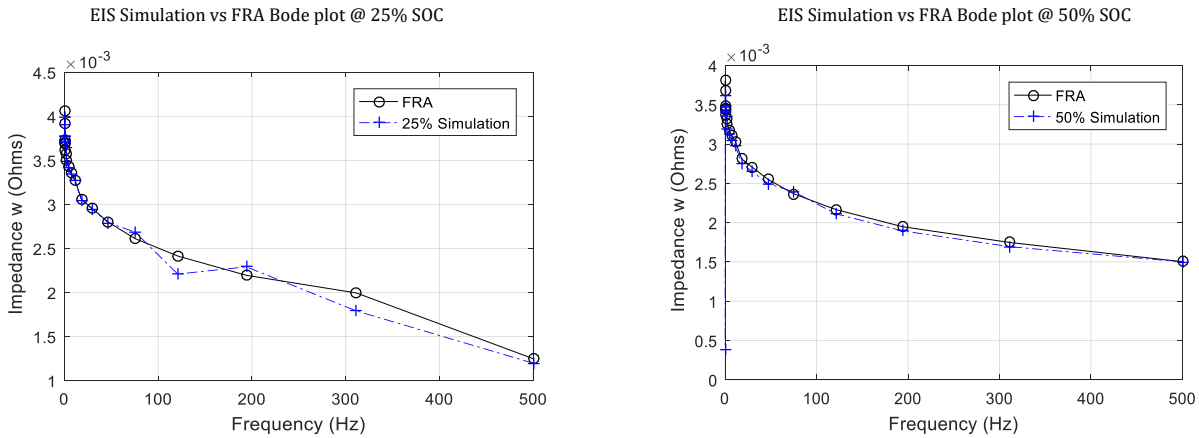

(a) (b)

Figure 7.7: Bode plot EIS Simulation results @ (a) 25% SoC (b) 50% SoC

7.4.2 *Effect of Discharge current*

The section discusses about the simulation of the parameterized discharged current of the li-ion cell. The FRA results gotten from the section 7.2 was used as a bench make to compare the results. The li-ion cell was simulated at the discharge current of $2A$ *and* $4A$ to be able to have fair comparison of the simulation and the FRA. The Figure 7.8 shows the simulated result of the discharge current of the battery at 25% *and* 50% SoC.

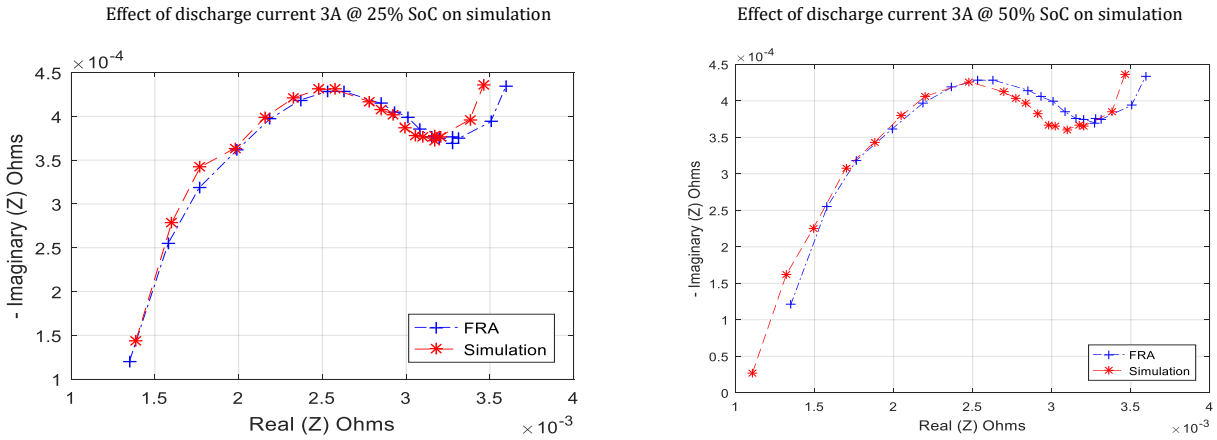

(a) (b)

Figure 7.8: Nyquist plot results on discharge current 3A @ (a) 25% and (b) 50%

The Nyquist plots results, that the Simulation results correspond with the FRA measurement results. The FRA and the simulated parameterize circuit results error is confirmed in the Table 7-2 below showing the error difference. The frequencies are divided into 3 regions. The first region is region greater than $500Hz$, this region is considered as the high frequencies' region, the middle frequencies region is frequency that falls between the region of $1Hz - 500Hz$, while low frequency region falls between frequencies less than $1Hz$. Table 7-2 shows that the error % of the EIS simulation results is less than 3% and EIS simulation results is similar with that of the FRA results.

Table 7-2: FRA vs Simulated EIS % error

SoC	25%		50%	
Test	FRA	Simulation	FRA	Simulation
f < 1	1.50	1.62	1.70	1.76
1 < f < 500	0.60	1.00	0.78	0.72
f > 1	2.42	2.32	2.69	2.45
All f	1.30	1.25	0.80	0.83

7.5 Experimental EIS using switching converter

EIS was Implemented using the switching converter for 100% SoC and 25% SoC. Figure 7.9 below shows the Nyquist and Bode magnitude plot of the Li-Ion cell at 100% SoC and 25% SoC while discharging for a 2A discharged current bias, the Nyquist and Bode plot result is comparable to the results obtained from the FRA devices.

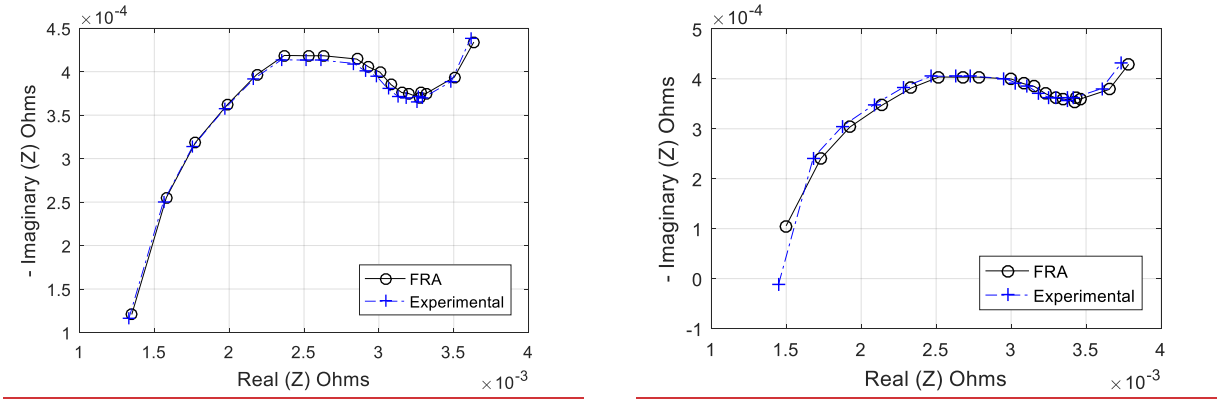

Figure 7.9: EIS Nyquist results on switching converter (a) 100% SoC (b) 25% SoC

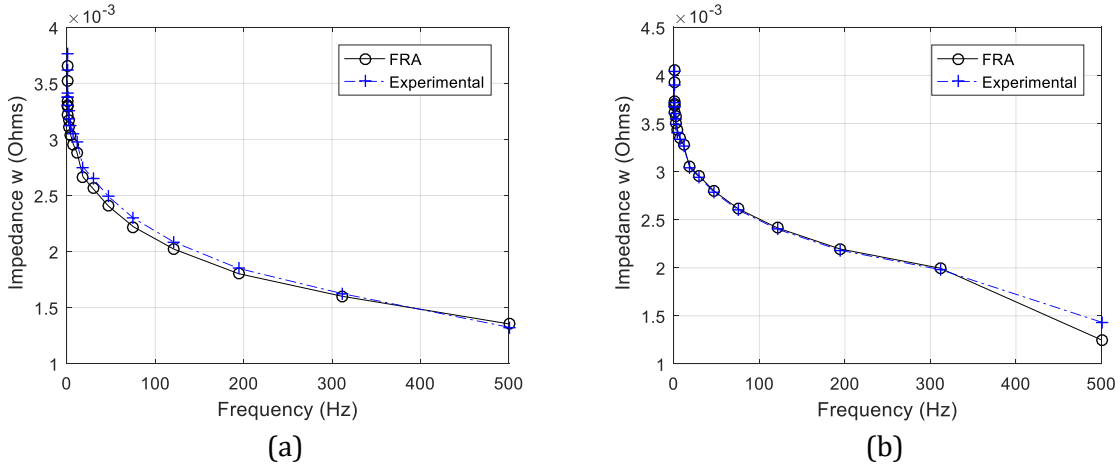

Figure 7.10: EIS Bode results on switching converter (a) 100% SoC (b) 25% SoC

The same experiment was then conducted on the Li-Ion cell at 50% SoC, however it was done for discharging current. This was done to demonstrate and compare the converters ability to perform EIS measurement during discharging. The result of the discharging current of 25% and 50% SoC is showed in the Figure 7.11. The results obtained are quite comparable to the FRA measurement of the Li-Ion cell.

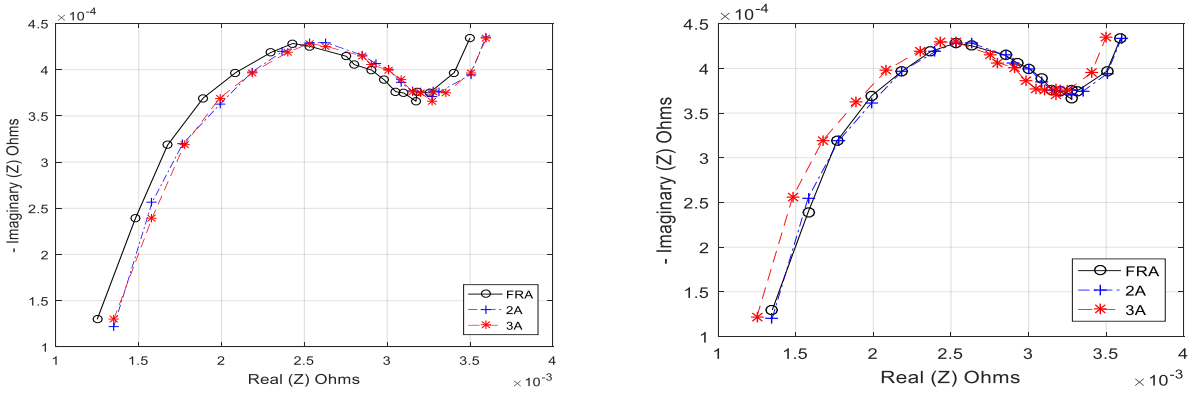

Figure 7.11: EIS Nyquist results on switching converter discharging at (a) 25% SoC (b) 50%SoC.

The Bode plot for the switching converter EIS correlates with that of the FRA result for the higher and middle frequencies but deviates slightly for the low frequencies. Table 7- 3shows that the average error is less than 6% for discharging current when the Li-Ion cell is at 25% *and* 50% SoC.

Table 7-3: 25% and 50% SoC of Switching Converter % error

SoC	25%		50%	
Discharge Current	$2A$	$3A$	$2A$	$3iA$
f < 1	3.86	4.12	3.99	4.20
1 < f < 500	2.99	3.26	3.15	3.46
f > 1	5.45	3.34	5.30	3.55
All f	3.36	3.30	4.42	4.53

7.6 Discussion and the experimental challenges overcome

From the experimental results, it can be deduced that the EIS performed on the FRA is accurate more than the EIS performed on the DC-DC boost converter. This is due to the parasitic element used in de-signing the converter which add up to the over- all impedance of the Lithium-ion battery. The DC-DC boost converter was used to inject IS signal without any additional circuitry, and it can be implemented on online system.

The experimental challenges that was overcome when performing IS with converter was that a short connectors and wires was used to avoid contributing to the impedance measure from the battery and also having a sufficient rest time for the battery when cycling the battery before measurement.

8. Conclusions and Recommendations

The major aim of this research was to explore the low-ripple three-level boost converter for EIS application. Two methods were investigated namely the offline EIS implementation and the online implementation. The offline EIS implementation was implemented using an industry standard FRA device to analyse the impedance change of the Lithium-ion battery. The online EIS implementation was implemented by duty cycle perturbation using a switching converter.

This research analysis the use of the three-level boost converter for EIS implementation. For online Implementation, the three-level boost converter is used for signal injection to measure the impedance of a Lithium-ion battery stack. The converter was operated at 50% duty cycle to ensure minimal input current ripple as required to implement EIS. It was demonstrated by varying the duty cycle of the three-level boost converter between 48% *and* 52%. The small signal analysis of the converter was used to create the voltage balance control and the current control of the converter. The current control is used to create the accurate perturbation in the inductor current, the inductor current perturbations were effective at creating a battery voltage response, so that impedance could be measured. The close loop results showed that the converter achieved a low input current ripple, although the experimental results showed an increase in the ripple from the simulations due to the shift in operating point, it was still lower than the past work using a conventional boost converter. The EIS results showed that the converter can performed EIS without large flirter because of the low input current ripple.

The experimental EIS results with the converter showed a good comparison with the simulated and the FRA results. The battery equivalent circuit parameters showed the necessary variations based on the SoC of the battery as required to monitor the battery's SoC. The low voltage stress of the three-level boost converter means that, impedance spectroscopy can be used to monitor the state of health of the batteries in high power applications with minimal down-time.

9. Bibliography

[1] E. T. a. R. S. R. H.Gan, “Implantable medical applications of lithium-ion technology,” in *Battery conference on Appilcations and Advanced Proceedings of Conference*, 2002.

[2] O. O. a. P. S. Barendse, “Characterization of Silicon based photovoltaic cells using broadband impedance spectroscopy,” in *Energy Conversion Congreess and Exposition*, USA, 2016.

[3] M. H. a. S. Islam, “Battery Impedance Measurement using Electrochemical Impedance Spectroscopy Board,” in *International Conference on Electrical & Electronics Engineering (ICEE)*, 2017.

[4] V. S. a. K. Dan, “High Resolution Converter for Battery Impedance Spectroscopy,” in *Energy Conversion congress and Exposition*, USA, 2017.

[5] D. U. S. a. W. W. C. Fleisheier, “Critical review of the Methods for monitoring Lithium Ion Batteries in Electric and Hybrid Vechicle,” in *journal of power source*, 2010.

[6] N. Mohan, “dc-dc switch mode converters,” in *Power Electronics, 2nd edition*, Canada, 1995, p. 184.

[7] P. b. Sean Moore, “Online Codition Monitoring of Lithium-ion Batteries using Impedance Spectroscopy,” in *Energy Conversion Congress Exposition*, USA, 2017.

[8] U. O. Washington, Classification of cells or Batteries, http://depts.washington.edu/matseed/batteries/MSE/classification.html., 2017.

[9] T. B. R. D. Linden, Handbook of Batteries, 1995pp25.

[10] I. a. C. E. I. Buchmann, Batteries in a portable world a handbook on rechargeable batteries for non-engineers, Cadex Electronics, 2011.

[11] k. Yiu, Battery technologies for electric vehicles and other green industrial projects, power electronics systems and application (PESA) 4th International Conference , 2011.

[12] portable rechargeable batteries (secondary batteries)., Battery association Japan: http;//www.barj.or.jp/e/knowledge/history03.html., 2013.

[13] S. C. a. J. Miller, Key challenges and recent progress in batteries, fuel cells, and hydrogen storage for clean eneegy systems, Journal of power sources, vol 159no. 1, pp.73-80, 2006, 2006.

[14] https://www.epectec.com/batteries/cell-comparison.html.

[15] R. paravasthu, Synthesis and Characterization of Lithium Cathode Materials in The System, Colorado State University: Department Of Mechanical Engineering , 2012.

[16] R. P. Touzain, "Insertion compounds of graphite with improved performances and electrochemical applications of those compounds", US, 1986.

[17] K.Mizushima, A new cathode material for batteries of high enery density., 1980..

[18] T. K.Tozawa, Lithium Ion Rechargeble battery. Progress in batteries and solar cells, 1990.

[19] K.Ozawa, Lithium-ion rechargeable batteries with LiCoO2 and carbon electrodes: the LiCoO2/C system., p. 212-221., 1994.

[20] I. Buchmann, "Types of Lithium-ion", 2015.

[21] K. Yiu, "Battery technology for electric vehicles and other green industrial project", Power Electronics Systems and Applications (PESA), 4th International Conference, 2011.

[22] T. B. C. Group, Batteries for Electric cars, 2010.

[23] J. C. a. J. Newman., Cyclable Lithium and Capacity Loss in Li-Ion Cells, Journal of The Electrochemical Society 152(4):A818, April 2005.

[24] P. F. B. B. S. H. K. N. M. Broussely, “Main aging mechanisms in Li-ion Batteries,” Journal of Power Society, 2005, p. 146.

[25] B. D. ,. S. G. a. D. R. A. Barre, “A review on Litjium-ion battery ageing, mechanism ansd estimations for automotive applications,” *Journal of power sources, vol 241,* pp. 680-689, 2013.

[26] Battery University, “BU-808b:what Causes LI_ion to Die”.*http://batteryuniversity.com/learn/article/bu_808b_what_causes_li_ion_to_die..*

[27] a. e. W. Waag, “Critical review of the methods for monitoring of Lithiun-ion Battaeries,” *Eslvier Journal of Power source,* Vols. vol 259,, pp. pp321-339, 2014.

[28] P. S. D. S. S. R. B. a. V. S. V. Ramadesigan, “Modeling and Simulation of Lithium-ion Battery from a Systems Engineering Perspective,” Journal of the Electrochemical Society, 2012.

[29] S. Hageman, “PSpice Models Nickel-metal Hydride cells,” February 1995.

[30] S. Hageman, “Simple Models let you Simulate Common Battery Types,” in *Electronic Design*, 1993, pp. pages17-129.

[31] M. Hannan, *A review of Lithium-ion battery state of charge estimation and management system in electric vechicle applications.*

[32] D.-I. Stroe, “Generalized Characterization Methodlolgy fo Perforamnce Modelling of Lithium-ion Batteries,” MDPI Batteries , 2016, pp. vol. 2, no. 37.

[33] V. Y. P. D. M. G. K. O. a. N. P. B. D.A Howey, “Online Measurement of Battery Impedance Using Motor Contoller Excitation,” in *IEEE TRransaction on Vihicular technology vol 63, no.6 pp.2557-2566.*, 2014.

[34] R. Koch and A. Jossen, “Impedance Spectroscopy for Battery Monitoring with Switched Mode Amplifiers,” in *16th International Power Electronics and Motion Control Conference and Exposition* , Antalya,Turkey, 2014.

[35] P. B. a. P. P. C.der Beer, “Fuel Cell Condition Monitoring Using Optimized Broad Impedance Spectroscopy,” *IEEE Transactions on Industrial Electronics,* 2015.

[36] O. Alao and P. Barendse, “"Online Condition Monitoring of Sealed Lead Acid & Lithium Nickel-CobaltManganese Oxide Batteries using Broadband Impedance Spectroscopy,",” in *IEEE Energy Conversion Congress and Exposition (ECCE),* , Portland, 2018.

[37] K. Godfrey, “Perturbation Signals for System Identification,” 1994.

[38] R. Koch and A.Jossen, “Impedance Spectroscopy for Battery Monitoring with Switched Mode Amplifiers,” in *16th International Power Electronics and Motion Control Conference and Exposition*, Antalya Turkey, 2014.

[39] W. a. J. Qahouq, “An Online Battery Impedance Measurement Method Using DC-DC Power Converter Control,” *IEEE Transactions on Industrial Electronics,* Vols. 16,no 11, pp. pp. 5987-59995, 2014.

[40] S. B. M. K. S. a. P. D. A. Ghosh, ““Design and Implementation of Type-II and Type-III Controller for DC-DC Switched-Mode Boost Converter by using K-Factor Approach and Optimization Techniques,,” in *IET Power Electronics, v*, 2016, pp. vol. 9, no. 5, pp.938-950.

[41] N. S. M. V. A. Chouki Balakishan, “Design and Implementation of Three-Level DC-DC Converter with Golden Section Search Based MPPT for the Photovoltaic Applications,” *Advances in Power Electronics,* 2015.

[42] ". A. L.-P. F. D. J. Karki, “Texas Instruments- AAP Precision Anlag,,” Dallas, Texas, 2002.

[43] J. Kozlowski, “Electrochemical cell prognostics using online impedance measurements and model-based data fusion techniques,” in *Aerospace Conference*, Big Sky, MT,USA, 2003.

[44] J. D. Kramer and C. Jacky, “How to write biblos,” vol. 1, no. 1, 2006.

[45] L. A. V. R. Krishna, “Control and implementation of three level boost converter for load voltage regulation,” in *IECON 2013 - 39th Annual Conference of the IEEE Industrial Electronics Society*, 2013.

[46] L. A. Vitoi, R. Krishna and D. E. Soman, “Control and implementation of three level boost converter for load voltage regulation,” in *IECON 2013 - 39th Annual Conference of the IEEE Industrial Electronics Society*, 2013.

[47] C. Y. Y. W. H. H. Lee, Journal of power sources with press, 2003.

[48] J. Karki, “Active Low-Pass Filter Design,” Texas Instruments- AAP precision Anlag, Dallas, Texas, 2002.

[49] J. Karki, “Analysis of the Sallen-Key Architecture,” July 2002. [Online]. Available: http://www.ti.com.cn/cn/lit/an/sloa024b/sloa024b.pdf. [Accessed 3 December 2017].

[50] H. R. a. A. Z. P. Desprez, “Estimation of the Soc and SoH of Li-ion Batteries by combining Impedance Measurements with the fuzzy logic inference,” in *36th Annual Conference on IEE Industrial Electronics Society*, 2010.

10. Appendices

10.1 Lithium-ion datasheet

ePLB C High Energy Product

Technology
Lithium Ion Polymer Battery
Li[NiCoMn]O2-based Cathode
Graphite-based Anode
High Energy Density
Optimized for PHEV, EV

Product General Specification

Mechanical Characteristics

Model	C020
Length	217.0 ± 1 mm (excluding terminal)
Width	129.0 ± 1 mm
Thickness	7.2 ± 0.2 mm
Weight	approx. 428 g

Electrical Characteristics

Nominal Voltage	3.65 V
Nominal Capacity	20 Ah
AC Impedance (1 KHz)	< 3 mΩ
Specific Energy	174 Wh/Kg
Energy Density	370 Wh/L
Specific Power(DOD50%, 10sec)	2300 W/Kg
Power Density(DOD50%, 10sec)	4600 W/L

Operating Conditions

Charge Conditions :	
Recommended Charge Method	CC/CV
Maximum Charge Voltage	4.15 V
Recommended Charge Current	0.5 C Current

Discharge Conditions :	
Recommended Voltage Limit for Discharge	3.0 V
Lower Voltage Limit for Discharge	2.5 V
Maximum Discharge Current (Continuous)	up to 5 C Current
Maximum Discharge Current (Peak < 10 sec)	10 C Current

Operating Temperature :	-30°C / + 55°C
Recommended Charge Temperature	0°C / + 40°C
Storage Temperature	-30°C / + 55°C

Cycle Life at 25°C : (1 C Charge / 1 C Discharge, DOD100%)
1000 Cycles to 80% Nominal Capacity

ePLB C020 Performance

Rate Capability

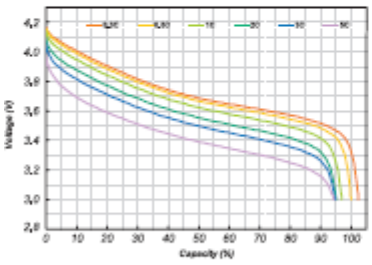

CHARGE : CC(0.5C)/CV(4.15V to 0.05C) at 25°C
DISCHARGE : CC to 3.0V at 25°C

Pulse Power Characteristics

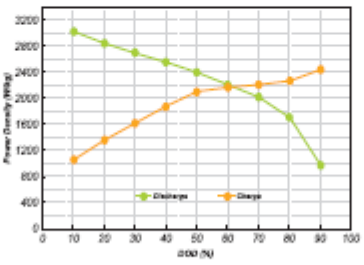

HPPC calculated from FreedomCAR Battery Test Manual

Cycle Life

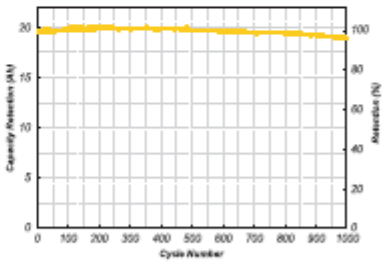

CHARGE : CC(1.0C)/CV(4.15V to 0.05C) at 25°C
DISCHARGE : CC(1.0C) to 3.0V at 25°C (DOD100%)

10.2 The circuit diagram of Three-Level boost converter

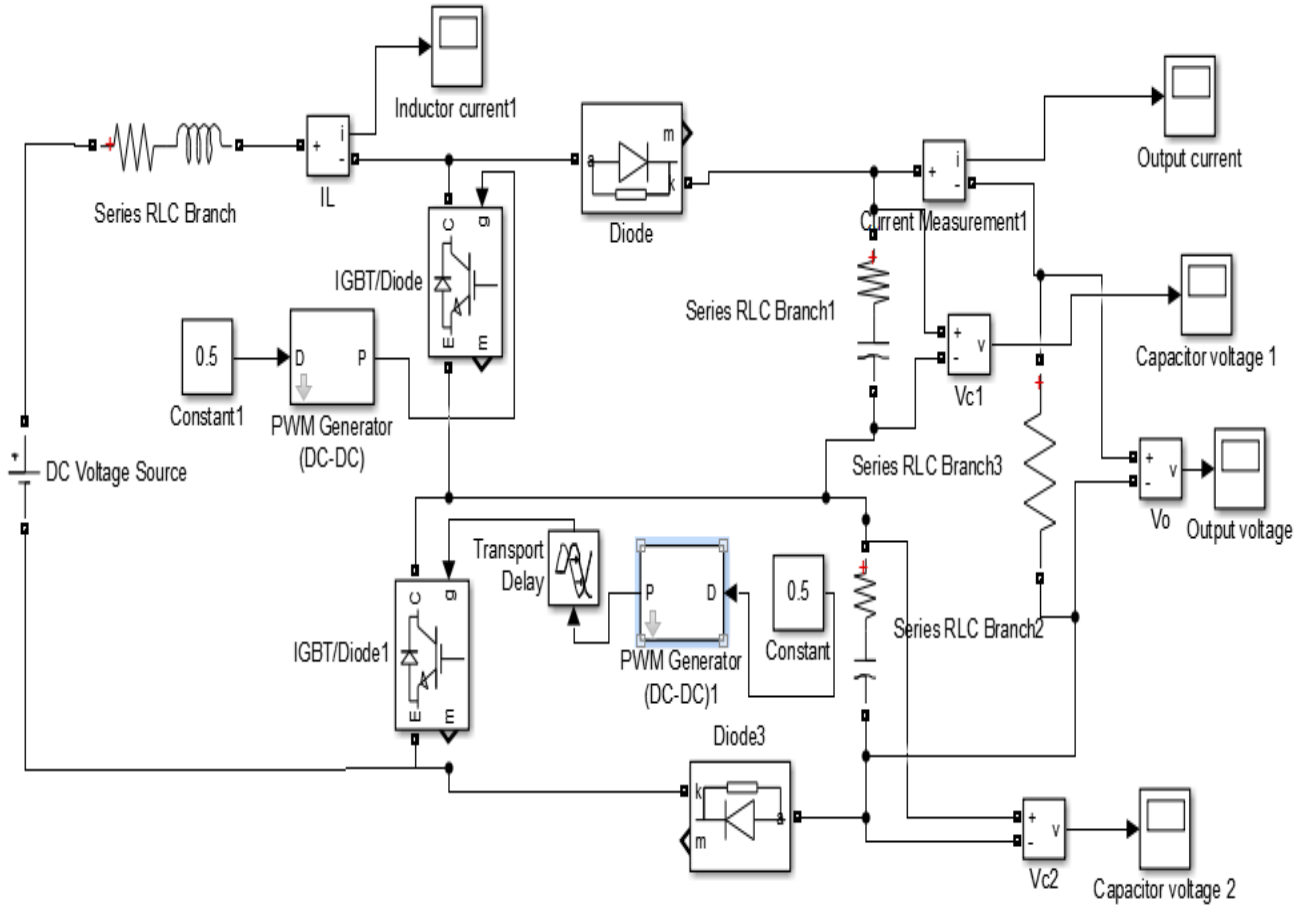

Figure 10.1: The circuit diagram of the Three-level Boost converter.

10.3 Battery Model with Three Level Boost Converter

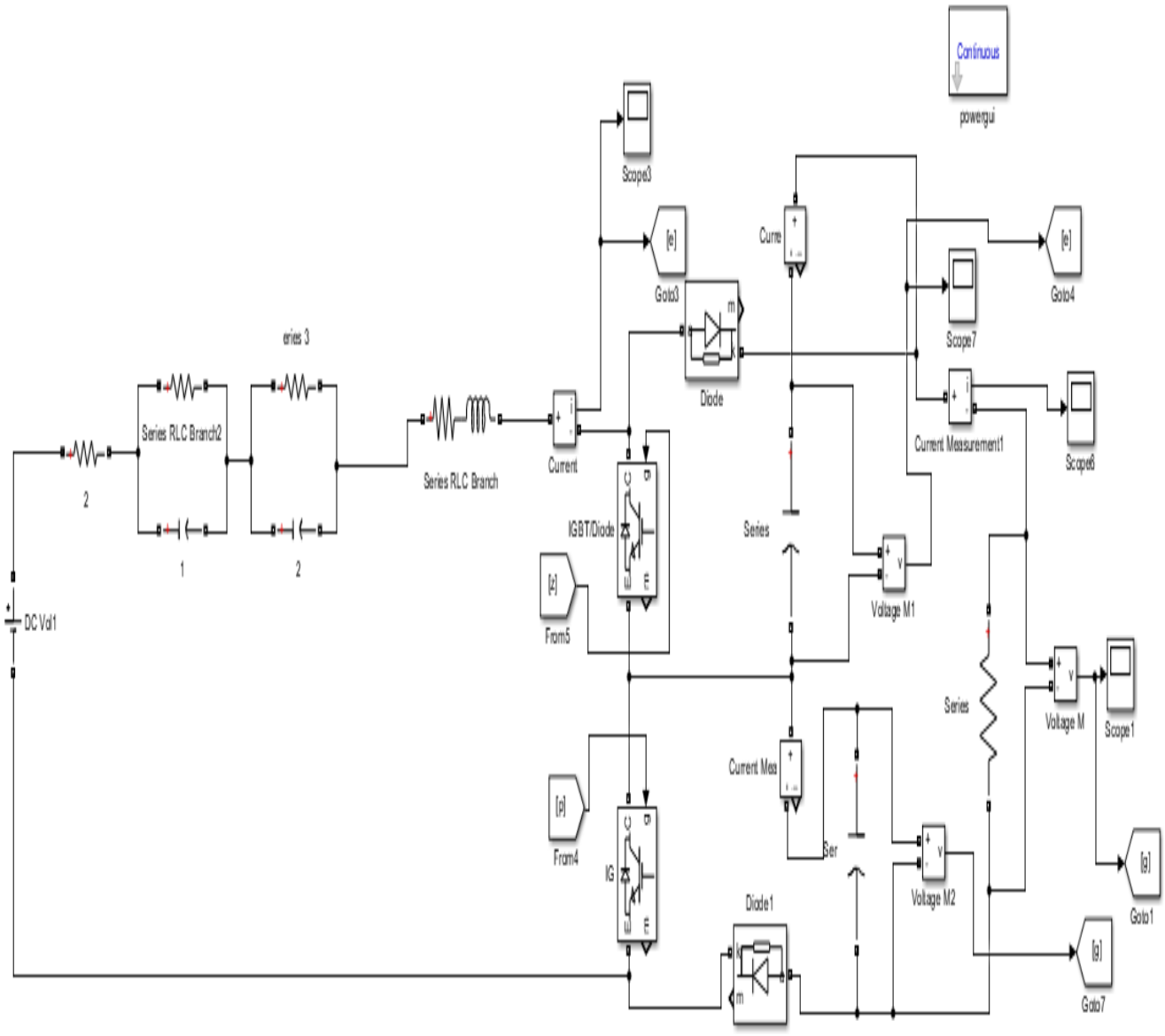

Figure 10.2: The circuit diagram of the simulated battery model with Three-level Boost converter.

10.4 Three-Level Boost Digital Control Diagram

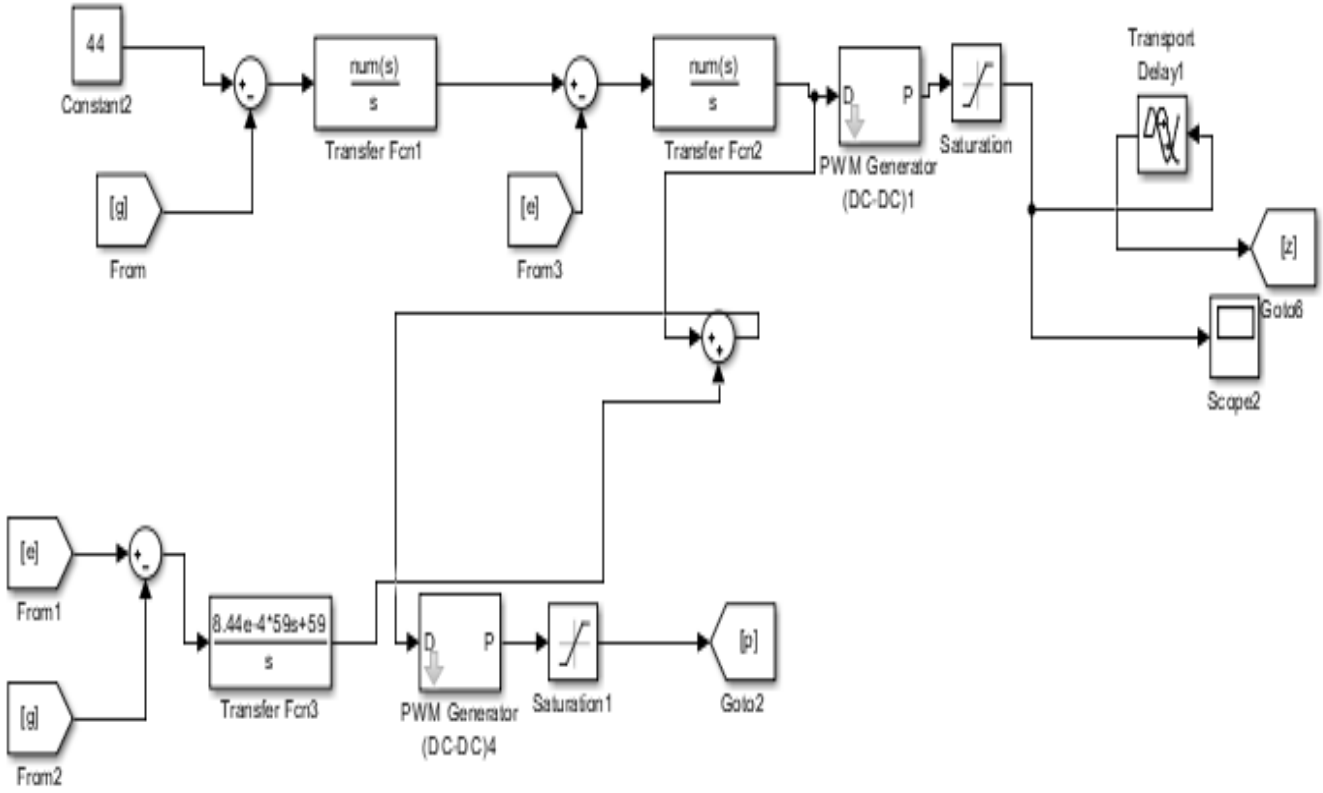

Figure 10.3: The digital control circuit diagram of the Three level Boost converter

10.5 MATLAB CODE

Figure(1)

```
AA =xlsread('Single_Cell_100SOC_Original.xls','Sheet1','A3:A21');
BB =xlsread('Single_Cell_100SOC_Original.xls','Sheet1','B3:B21');
CC =xlsread('Single_Cell_100SOC_Original.xls','Sheet1','C3:C21');
DD =xlsread('Single_Cell_100SOC_Original.xls','Sheet1','D3:D21');
EE =xlsread('Single_Cell_100SOC_Original.xls','Sheet1','E3:E21');
FF =xlsread('Single_Cell_100SOC_Original.xls','Sheet1','F3:F21');



plot(AA,BB,'k-o')
hold on
plot(CC,DD,'b-.+')
hold on
plot(EE,FF,'r--*')
grid on
%grid minor
xlabel('Real (Z) Ohms')
ylabel('- Imaginary (Z) Ohms')
legend('100% SOC','50% SOC','25% SOC','location','SouthEast')


Figure (2)

AA1 =xlsread('Single_Cell_100SOC_Original.xls','Sheet2','A3:A21');
BB1 =xlsread('Single_Cell_100SOC_Original.xls','Sheet2','B3:B21');
CC1 =xlsread('Single_Cell_100SOC_Original.xls','Sheet2','C3:C21');
DD1 =xlsread('Single_Cell_100SOC_Original.xls','Sheet2','D3:D21');
EE1 =xlsread('Single_Cell_100SOC_Original.xls','Sheet2','E3:E21');
FF1 =xlsread('Single_Cell_100SOC_Original.xls','Sheet2','F3:F21');



plot(AA1,BB1,'k-o')
hold on
plot(CC1,DD1,'b-.+')
hold on
plot(EE1,FF1,'r--*')
grid on
%grid minor
xlabel('Real (Z) Ohms')
ylabel('- Imaginary (Z) Ohms')
legend('100% SOC','50% SOC','25% SOC','location','SouthEast')

Figure (3)

AA2 =xlsread('Single_Cell_100SOC_Original.xls','Sheet3','A2:A20');
BB2 =xlsread('Single_Cell_100SOC_Original.xls','Sheet3','B2:B20');
CC2 =xlsread('Single_Cell_100SOC_Original.xls','Sheet3','C2:C20');
DD2 =xlsread('Single_Cell_100SOC_Original.xls','Sheet3','D2:D20');
EE2 =xlsread('Single_Cell_100SOC_Original.xls','Sheet3','E2:E20');
FF2 =xlsread('Single_Cell_100SOC_Original.xls','Sheet3','F2:F20');

plot(AA2,BB2,'k-o')
```

```
hold on
plot(CC2,DD2,'b-.+')
hold on
plot(EE2,FF2,'r--*')
grid on
%grid minor
xlabel('Real (Z) Ohms')
ylabel('- Imaginary (Z) Ohms')
legend('100% SOC','50% SOC','25% SOC','location','SouthEast')

 Figure(4)

AA3 =xlsread('Single_Cell_100SOC_Original.xls','Sheet2','G3:G21');
BB3 =xlsread('Single_Cell_100SOC_Original.xls','Sheet2','H3:H21');
CC3 =xlsread('Single_Cell_100SOC_Original.xls','Sheet2','I3:I21');
DD3 =xlsread('Single_Cell_100SOC_Original.xls','Sheet2','J3:J21');

plot(AA3,BB3,'k-o')
hold on
plot(AA3,CC3,'b-.+')
hold on
plot(AA3,DD3,'r--*')
grid on
%grid minor
xlabel('Frequency (Hz)')
ylabel(' Impedance w (Ohms)')
legend('100% SOC','50% SOC','25% SOC','location','NorthEast')

Figure(5)
AA4 =xlsread('Single_Cell_100SOC_Original.xls','Sheet1','G3:G21');
BB4 =xlsread('Single_Cell_100SOC_Original.xls','Sheet1','H3:H21');
CC4 =xlsread('Single_Cell_100SOC_Original.xls','Sheet1','I3:I21');
DD4 =xlsread('Single_Cell_100SOC_Original.xls','Sheet1','J3:J21');

plot(AA3,BB3,'k-o')
hold on
plot(AA3,CC3,'b-.+')
hold on
plot(AA3,DD3,'r--*')
grid on
%grid minor
xlabel('Frequency (Hz)')
ylabel(' Impedance w (Ohms)')
legend('100% SOC','50% SOC','25% SOC','location','NorthEast')

Figure(6)


AA5 =xlsread('Single_Cell_100SOC_Original.xls','Sheet3','G2:G20');
BB5 =xlsread('Single_Cell_100SOC_Original.xls','Sheet3','H2:H20');
CC5 =xlsread('Single_Cell_100SOC_Original.xls','Sheet3','I2:I20');
DD5 =xlsread('Single_Cell_100SOC_Original.xls','Sheet3','J2:J20');

plot(AA3,BB3,'k-o')
hold on
plot(AA3,CC3,'b-.+')
hold on
plot(AA3,DD3,'r--*')
```

```
grid on
%grid minor
xlabel('Frequency (Hz)')
ylabel(' Impedance w (Ohms)')
legend('100% SOC','50% SOC','25% SOC','location','North
```